A Modeling Pipeline and Parametric Study to Estimate the Biomechanical Behaviour of Bio-Engineered Fibrous Caps

Berry Kaaij

Student Number: 5261023

Delft University of Technology & Erasmus University Medical Centre

Main Supervisor: Dr. ir. A. Akyildiz

Daily Supervisor: PhD Student A. Tziotziou

Abstract

Background: Atherosclerosis is a progressive arterial disease that gives rise to plaque. Rupture thereof is a main cause of myocardial infarction and ischaemic stroke. A plaque can have a fibrotic layer between its lipid pool and the arterial lumen, which is termed a fibrous cap (FC). Rupture of this FC can expose thrombogenic plaque content to the bloodstream. From a mechanical viewpoint, the FC is hypothesized to rupture when its strength is exceeded by the structural stresses imposed thereupon. Stresses in the FC can not be measured and are generally approximated by using digital analogs such as finite element models. Such models require among other things a definition of the FC its in-vivo composition. However, this is still poorly understood as it can presently not be measured in-vivo. To investigate the relations between a FC its composition and its mechanical properties, bio-engineered FCs (BE-FC) have been developed by researchers. These BE-FCs are reported to bear resemblance to human FCs in terms of bulk mechanical properties. This study aims to aid in the comprehension of the biomechanical behaviour of these BE-FCs.
Methods: A finite element modeling pipeline has been developed for BE-FCs. Following the pipeline provides a 2D BE-FC model and a total of 16 BE-FCs were modeled. Material behaviour is defined using the Holzapfel-Gasser-Ogden model. The BE-FC models their geometry and material parameters are acquired using geometry and collagen images in combination with self-developed and data-scaleable scripts. Model simulation results provide an approximation of the BE-FC its biomechanical behaviour. This study includes an investigation of the BE-FC models their global biomechanical behaviour as well as their stress and strain peak values, peak value locations, and distributions. In addition a parametric study has been performed; 1260 idealised BE-FC models were created. These models differ in geometry and composition, allowing a more in-depth investigation of the BE-FC models their stress and strain peak values and distributions.
Results: The global biomechanical behaviour of the BE-FC models satisfyingly approximates that of their respective BE-FC. Peak stresses and strains in the BE-FC models are considerably higher than those found in the literature for ex-vivo uni-axially tensile tested FCs as well as compared to FC sections of finite element models. To the same extent the locations of the peak stresses and strains in the BE-FC models could not be co-localized to the rupture initiation locations of the BE-FCs. The stress and strain distributions are thoroughly examined using the simulation results of the idealised models. Depending on the specific stress and strain metric, each is contingent on different model characteristics and/or behaviours. In general however the most crucial of these are the collagen fibre dispersion κ, the collagen fibre mean angle Θ, the degree of model compaction, and the model its soft inclusion shape and size.
Conclusion: With this study, a novel modeling pipeline has been developed for 2D BE-FC finite element models. Results from simulations therewith give insight into the biomechanical behaviour of BE-FCs. In addition a parametric study has been performed, resulting in numerous idealised BE-FC models. The simulation results of these models aid considerably in the understanding of the BE-FCs their biomechanical behaviour. Taking everything in consideration, a contribution has been made to the comprehension of BE-FCs and along with that it therefore assists current research invested in answering how, why and when a FC ruptures.

Keywords: Atherosclerosis, Atherosclerotic Plaque, Plaque Rupture, Fibrous Cap, Stress Analysis, Strain Analysis, Finite Element Analysis

Table of contents

Nomenclature

List of Abbreviations

FC	Fibrous Cap
BE-FC	Bio-engineered Fibrous Cap
SI	Soft Inclusion
HGO	Holzapfel-Gasser-Ogden
VM	Von Mises
H	(model) height
W	(model) width
SIx	(model) Soft inclusion size in the X-direction
SIy	(model) Soft inclusion size in the Y-direction
LBc	(model) compaction of the left boundary
RBc	(model) compaction of the right boundary

List of Symbols

U	Strain energy per unit of reference volume
D	Parameter describing the compressibility of the material
C_{10}	Stress-like material constant related to isotropic material response [MPa]
k_1	Stress-like material constant related to anisotropic material response [MPa]
k_2	A dimensionless parameter related to anisotropic material response
κ	Collagen fibre dispersion
Θ	Collagen fibre mean angle [deg]
ρ	Orientation density function
N	Amount of fibre families
$\bar{C}$	Distortional part of the right Cauchy-Green strain
$\bar{I}_1$	The first invariant of $\bar{C}$
A_α	set of unit vectors with $\alpha = 1, ..., N$
$\bar{I}_{\alpha\alpha}$	The pseudo-invariant of $\bar{C}$ and A_α
J	Total volume ratio
J^{el}	Elastic volume ratio
J^{th}	Thermal volume ratio
ϵ_i^{th}	Thermal expansion strains
μ	Von Mises distribution collagen fibre mean angle [radians], equal to Θ
b	Von Mises distribution concentration parameter
$\bar{\rho}$	Von Mises orientation density function
I_0	1st kind 0th order modified Bessel function
erfi(x)	Imaginary error function
S_x	Stress in the X-axis its direction [MPa]
LE_x	Strain in the X-axis its direction
S_y	Stress in the Y-axis its direction [MPa]
LE_y	Strain in the Y-axis its direction
S_{xy}	Shear stress in the plane made by the X and Y axes [MPa]
LE_{xy}	Shear strain in the plane made by the X and Y axes
$S_{\text{in-fib}}$	Stress along the collagen fibres [MPa]
$LE_{\text{in-fib}}$	Strain along the collagen fibres
$S_{\text{across-fib}}$	Stress across the collagen fibres [MPa]
$LE_{\text{across-fib}}$	Strain across the collagen fibres

List of Figures

List of Tables

1 Introduction

Myocardial infarction and ischaemic stroke are prevalent in the developed part of the world, contributing to lifelong disability as well as mortality [1, 2]. Currently it is common knowledge that in the aetiology of myocardial infarction and ischaemic stroke, coronary and carotid atherosclerotic plaque rupture (wherewith bloodflow-blocking thrombolytic events can occur) is a leading factor [3].

Atherosclerosis
A healthy artery consists of three wall layers. From the artery its luminal surface outwards this includes: the tunica intima, the tunica media, and the tunica adventitia. Atherosclerosis is a progressive arterial disorder characterized by adaptive intimal thickening and the accumulation of fatty deposits in the tunica intima [4]. Significant arterial changes are initially limited to the tunica intima; yet disruption of the tunica adventitia and media may occur in later stages of the disease [4]. Progression of the plaque can give rise to large lipid core(s) and a fibrous layer (fibrous cap / FC) between said core(s) and the lumen [4]. Furthermore, the lipid core(s) can necrotize and the artery can develop calcifications and or haemorrhages [4]. Fig. 1 illustrates the components of a plaque. A more comprehensive plaque (progression) classification is imparted by Akyildiz [5].

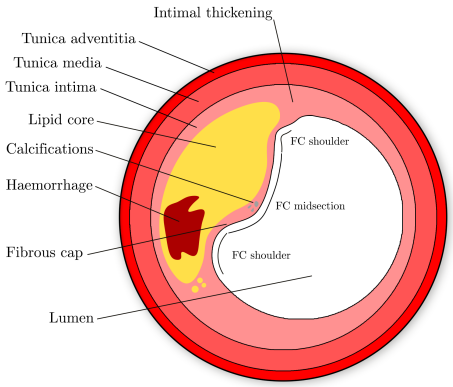

Figure 1: Illustrative representation of a plaque. All three artery wall layers can be observed: the tunica intima, media, and adventitia. The plaque has a lipid core, calcifications, a haemorrhage, and a fibrous cap. The fibrous cap is described into sections based upon location. These sections are denoted by the midsection and the shoulder sections.

Plaque Rupture
Not all plaques are considered as being vulnerable to rupture. Conversely, not all plaques that are prone to rupture, actually do so. However still, the rupture of a plaque its FC is generally associated with adverse bloodflow-blocking thrombolytic events as it separates the plaque its lumen from a lipid rich core. From a mechanical perspective FC rupture is hypothesized to ensue when its strength is exceeded by the stress it experiences [6, 7]. Indeed, stress concentrations are frequently used in the localization of plaque rupture [8–10]. The stress throughout the FC and its strength both depend upon plaque geometry, composition, and loading [4, 11]. This includes - among other things - FC curvature, FC thickness, FC

stiffness, FC inflammation, and necrotic core thickness [11, 12]. Fig. 1 illustrates a most rupture-vulnerable plaque termed a "thin-cap fibroatheroma"; it has a large soft necrotized lipid core (radial direction) accompanied by a thin, stiff and inflamed FC [4, 11, 13]. It follows naturally that understanding the relationship between the FC its loading, characteristics and its biomechanical behaviour is fundamental to accurately comprehend and assess plaque rupture.

The Fibrous Cap

The load a FC experiences is dual. A FC is subjected to structural stresses and wall shear stresses due to blood pressure and blood flow, respectively [14, 15]. Between the pair the wall shear stress is approximately four magnitudes lower [16]. Further, it is believed to contribute to plaque rupture vulnerability as it contributes to plaque formation, growth, and FC erosion [16–19]. On the other hand, structural stresses seem to play a direct major role in FC rupture [16, 20].

As is illustrated by Fig. 2 the FC can take on many shapes; including non-circular, asymmetric and highly curved shapes. The geometry has a pronounced effect on plaque rupture vulnerability because thin FC sections and high lumen curvatures are associated with high local FC stresses [5, 9, 21–24]. A majority of the FC ruptures are in fact localized to thin FC locations or the FC shoulders (a location where marked curvature often occurs, see Fig. 2) [25–28].

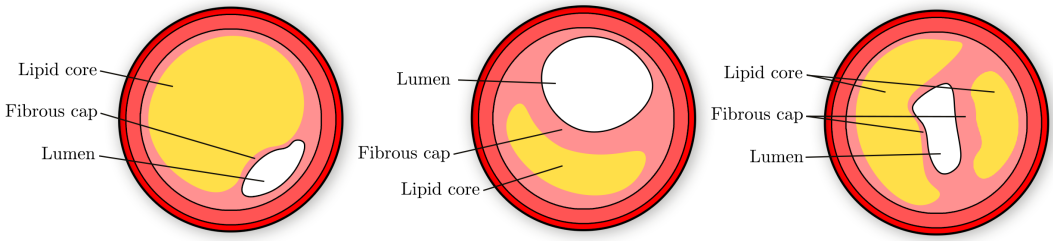

Figure 2: Three exemplary plaques with different FC geometries.

The FC composition can differ substantially both between different FCs as well as between local sections of a single FC. To start with, the FC can consist of smooth muscle cells, microcalcifications, macrophages, lymphocytic cells, elastin fibres, and type I & III fibrillar collagen fibres [6, 29–31]. The collagen fibres collectively constitute the main load-bearing constituent of the FC termed the collagenous matrix [32, 33]. The properties of this matrix depend upon the orientation, density, distribution, cross-linking, and the type of its collagen fibres [34–37].

Fibrous Cap Rupture

The exact relations between the FC its loading, characteristics and its biomechanical behaviour is however still opaque. A main cause of this is that stress is not directly measurable. The literature reports a plethora of FC rupture stress values ranging from e.g. 83 kPa to a commonly adopted value of 300 kPa, up to 683.3 kPa [15, 17, 20, 38]. A prevalent approach

to obtain the stress involves simulations with computational finite element models. This approach is often adopted as it is cost-efficient, because models consume relatively little time to construct, and per the fact that models can be readily altered. A model is a digital analog, requiring an as accurate as possible approximation of the tissue its loading conditions, geometry, and composition. The in-vivo FC geometry can be measured by using e.g. optical coherence tomography or intravascular ultrasound [39–41]. The in-vivo composition however remains elusive. Currently employed imaging modalities are insufficient. Moreover, ex-vivo composition characterization is sub-optimal. Excised ruptured FCs have a damaged morphology while excised unruptured FCs are possibly unrepresentative cases as plaques are highly heterogeneous.

Bio-Engineered Fibrous Caps
In-vitro bio-engineered collagen tissue analogs are a current topic, with literature presenting analogs with phenotypes and behaviour alike that seen in in-vivo biological systems. Correspondingly, to understand the composition and biomechanical behaviour of the plaque its FC, Wissing et al. [42] have cultured bio-engineered FCs (BE-FCs). Multiple such BE-FCs are illustrated in Fig. 3. Wissing et al. [42] reported that the BE-FCs have stiffness properties, a composition and a straining pattern alike that to real human FCs. Interestingly, these BE-FCs can be readily quantified. All things considered BE-FCs provide a novel, organized, and malleable means to investigate real human FCs in terms of composition and biomechanical behaviour - including rupture.

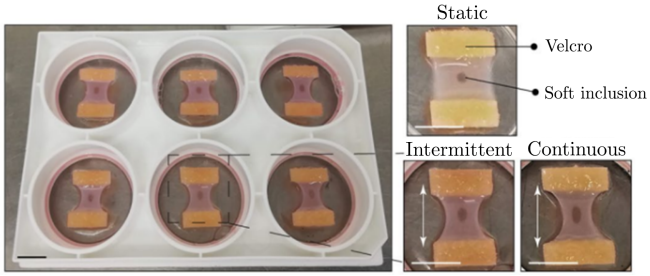

Figure 3: As adopted from [42]. Six BE-FCs are shown (pink). The BE-FCs are fixed between Velcro strips (yellow). The BE-FCs have been given a circular perforation termed a soft inclusion. Differences in the BE-FC geometry can be noted depending upon the straining protocol (highlighted as static, intermittent or continuous straining).

1.1 Research aim

A multitude of factors contribute to FC rupture. Moreover, the characteristics of FCs are difficult to measure - thereby occluding the understanding ánd prediction of FC rupture. Considering the potential contribution of BE-FCs in this regard, this study aims to further clarify their biomechanical behaviour.

To investigate the BE-FCs their biomechanical behaviour a finite element modeling pipeline is developed. The therefrom resulting models allow an assessment of the stresses and strains a BE-FC experiences. In specific, the stress and strain distributions in BE-FCs during uniaxial tensile loading until rupture are investigated. In light of FC rupture this includes the

consideration of peak stress and strain values including their locations. Over and above this a parametric study has been performed. In particular, 1260 idealised BE-FC finite element models have been constructed with differing morphologies and compositions. This allows the assessment of the relations between a BE-FC its morphology, composition, and biomechanical behaviour. The distributions as well as the peak values of their stresses and strains have been investigated.

2 Bio-engineered Fibrous Caps

Before presenting the methods used to construct BE-FC models, the actual BE-FCs will be discussed more in-detail first. This allows a better grasp of the BE-FC models their characteristics, the assumptions made, and the outcomes of model simulations.

The BE-FCs have been developed by Wissing et al. [42] and associate researchers at the Erasmus Medical Center Biomedical engineering department and at Eindhoven University of Technology. This also includes any experiments done on the BE-FCs and the gathering of data. Accordingly all acknowledgement goes to said researchers.

The initial Geometries
The BE-FCs start as myofibroblast-seeded fibrin-based gels affixed between two Velcro strips. The initial planar gel geometries are shown in Fig. 4. These gels have a punctured hole in their centre which acts as a soft inclusion analog (SI); replicating the lipid-rich necrotic core as observed in plaques. To realize more inter-gel variation some SIs were filled with fibrin for SI-gel integration.

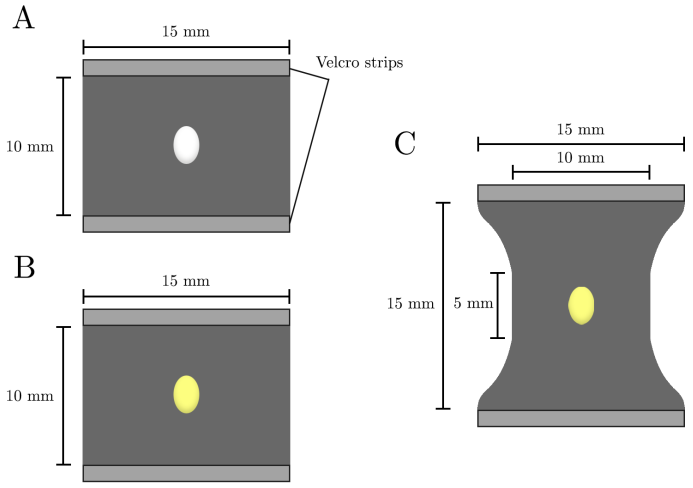

Figure 4: The initial gel geometries. Three distinct geometries are illustrated. These geometries either have an empty SI (white ellipse) or a fibrin-filled SI (yellow ellipse).

Compositional & Geometrical Changes
In order to accomplish multiple distinctly dissimilar BE-FC compositions, each gel was subjected to one of three different uniaxial straining protocols. These protocols involved either static, intermittent, or continuous straining (see Appendix A for details). The straining protocols also affect the BE-FCs their final geometry, see Fig. 5 for illustrations. In-plane the resulting BE-FCs were seen to have compacted boundaries and a narrowed SI. In addition many BE-FCs developed asymmetric shapes. Out-of-plane the BE-FCs matured into the particular shape also shown in Fig. 5.

The initial geometries of the gels have as a matter of fact been premeditated based upon these changes. Indeed, in Fig. 6 it can be seen that the compacted planar BE-FC geometry roughly approximates the shape of a real FC.

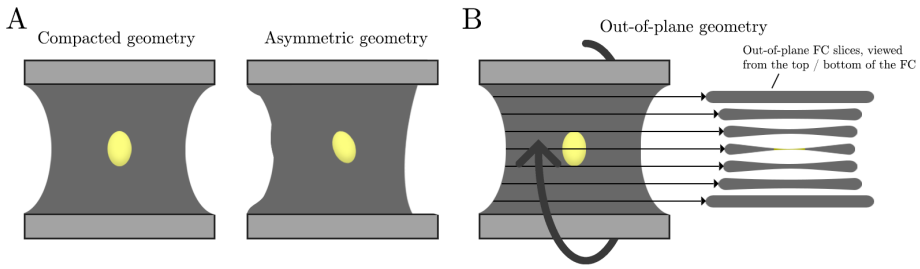

Figure 5: Illustrative BE-FC geometries after completion of the straining protocols. Subfigure A: two exemplary distorted planar geometries. Subfigure B: an exemplary out-of-plane BE-FC geometry.

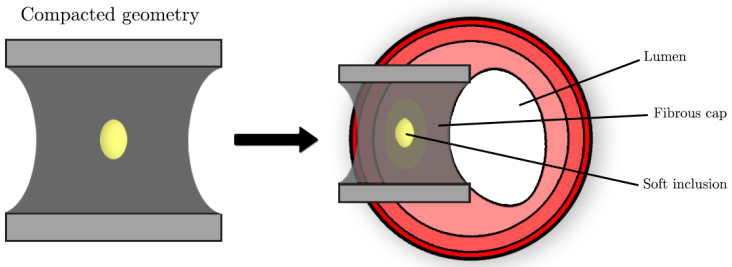

Figure 6: Interpretation of the BE-FC geometry.

Capturing the Geometry and Composition
Both the geometry as well as the composition of the BE-FCs were captured. Multiphoton microscopy imaging was performed to obtain the BE-FC its geometry whereas multiphoton second harmonic generation was used to visualize its composition. Both procedures comprise a grid-like manner imaging method, i.e. capturing 738.1 x 738.1 μm subsections of the BE-FC and subsequently merging the images as illustrated in Fig. 7.

It can be noted that the BE-FC its composition is imaged only on two whole-width grid strips (see Fig. 7). In addition composition imaging was also performed in the in-depth direction of the BE-FCs (an image was taken every 3 μm starting just under the surface of the BE-FC). The collagen content was observed to differ through the thickness of the BE-FCs, with the collagen content being considerably higher near the BE-FC its surface. Collagenous matrix characterization in the subsequent paragraphs is performed with the maximum intensity projection collagen images.

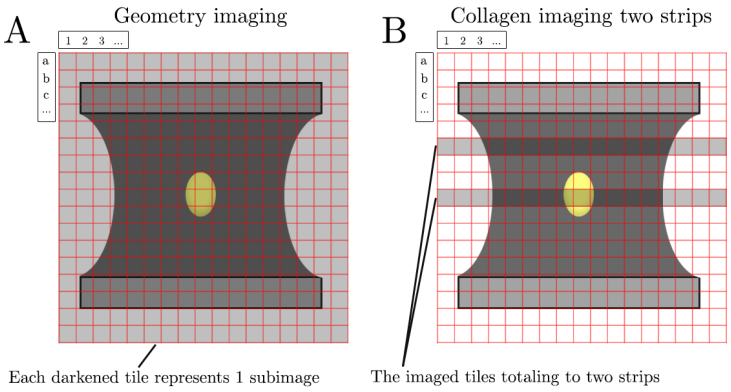

Figure 7: Geometry and collagen imaging strategy BE-FCs. Two BE-FCs affixed between Velcro strips and overlaid with a grid are shown. Darkened grid tile = location where an image is taken. After imaging the grid tile images are merged to create a total image. Subfigure A: strategy for whole BE-FC geometry imaging. Subfigure B: strategy for "two-strips" BE-FC collagen imaging.

Capturing the Biomechanical Behaviour

After having captured the geometry and composition, the biomechanical behaviour of the BE-FCs was investigated by performing a uniaxial tensile test in conjunction with digital imaging and digital image correlation. Fig. 8 illustrates this process.

Firstly, the BE-FCs were airbrushed with a tissue dye for digital image correlation and subsequently placed in a tensile tester. To ensure that the BE-FCs were in a static and non-folded condition before commencement of the tensile test a pre-stretch was performed until 0.15 mN was measured. This was followed by the application of ten pre-conditioning strain cycles at 10% strain and a strain rate of 200%/min to get the BE-FCs in a state of repeatable loading-unloading behaviour. Hereafter the tensile test was performed at a strain rate of 200%/min until failure.

During the tensile test the location(s) of rupture initation and the rupture propagation pattern(s) were captured with digital imaging. Lastly, digital image correlation provided the local strains in the BE-FCs during the tensile test. This analysis was isolated to the non-compacted and non-fixed region of the BE-FCs to account for artifacts.

The Specifics for Each Bio-engineered Fibrous Caps

A total of 16 BE-FCs are modeled. The details of the exact experimental procedure followed for each BE-FC is delineated in Appendix A. These details include the number of the BE-FC, the initial planar geometry shape including the dimensions and SI type, the particular straining protocol imposed upon it, the clamp-to-clamp distance between the clamps when the BE-FC is placed in the tensile tester, and lastly the specifics of the tensile test.

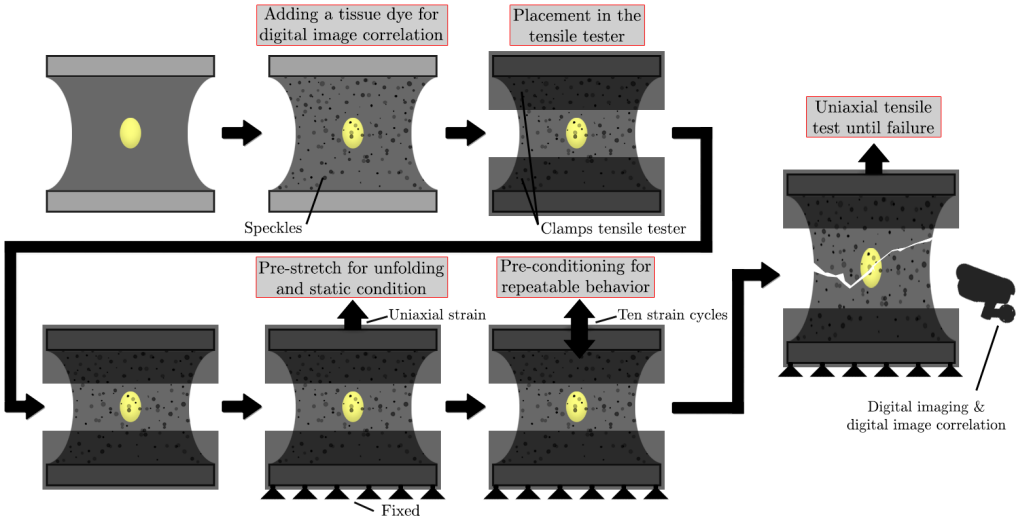

Figure 8: The uniaxial tensile test procedure for the BE-FCs.

3 Methods

3.1 Bio-Engineered Fibrous Caps - Models

16 BE-FC finite element models have been created in the modeling software Abaqus (Dassault Systèmes Simulia Corp.) [43]. Such models require a definition of the BE-FC its geometry, composition, and boundary conditions. In addition to this in finite element models the geometry is represented by connected segments called elements. Collectively the elements are termed the mesh of the model. The characteristics of these elements also need to be specified as they influence model simulation results.

Over and above these specifications, simplifications and assumptions are made for the models. To start with the BE-FC models are simplified to 2D. This simplification greatly reduces the complexity of the models. This is especially so due to the fact that the models will be given an anisotropic material model while 3D anisotropic composition modeling is a standalone endeavor on its own. On top of that it is currently unknown if simpler 2D models can capture the biomechanical behaviour of the BE-FCs. As such these models will either approve or disprove a 2D simplification; if the models cannot accurately capture the behaviour this could indicate the necessity of 3D models in future research. In addition the models are assumed plane-stress as: (1) the BE-FCs are loaded ánd supported in-plane in the tensile tester, and (2) the BE-FCs have relatively large dimensions in-plane as compared to out-of-plane (ratio $Y/X : Z \approx 1/1 : 10$). Lastly, the SI is assumed to be very compliant and therefore modeled as a "hole". In the following subsections the post-processing of the acquired data and all model components (geometry, composition, boundary conditions, and mesh specifics) will be discussed.

3.1.1 Geometry

The merged geometry image for each BE-FC (see again Fig. 7) was used to recreate the planar BE-FC geometry. Instead of manually tracing the boundaries of each BE-FC and calculating the dimensions, a Matlab script has been developed to achieve a geometry with a data-scaleable approach. The essential steps are presented in the following list and illustrated in Fig. 9.

1. The merged geometry image is cropped to only include the BE-FC geometry itself. Additionally, another cropped image is made which only includes the SI.

2. In both cropped images the brightness of the pixels in the background is higher. This brightness is used to trace the boundaries of the BE-FC and the SI. In addition - depending on the graininess of the boundaries and the amount of noise in the images - the boundary traces are smoothed by use of a Savitsky-Golay filter. Following this the boundary traces are combined through cross-correlation of the two cropped images.

3. Using the combined boundary a binary image of the BE-FC geometry is created. This image clearly shows where in the original captured image the BE-FC is - and is not. Knowing the pixel-millimeter ratio and having the geometry in binary image format, a planar orphan mesh is constructed in Matlab by use of the Matlab package MESH2D [44]. This mesh forms the basis of the BE-FC its geometry and is imported in the finite element modeling software Abaqus.

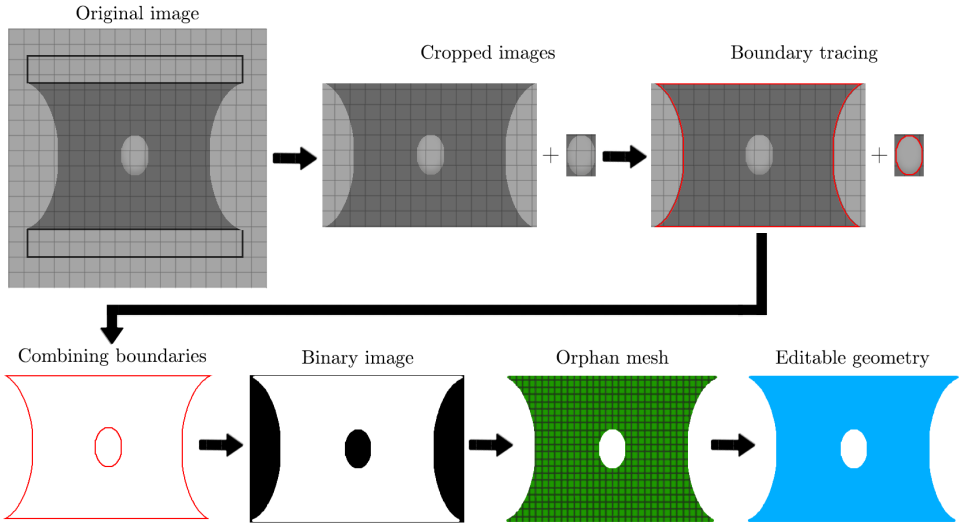

Figure 9: The steps from geometry image to model geometry. This includes: (1) image cropping to get a cropped BE-FC and SI image, (2) boundary tracing on both cropped images, (3) combining the traces, (4) creating a binary image using the traces, (5) creating an orphan mesh, and (6) converting the orphan mesh to an editable geometry.

4. In Abaqus an orphan mesh is a near-uneditable collection of nodes and elements. The mesh however can contain inaccuracies due to noise and/or artifacts in the image. Therefore it is converted to an ordinary fully editable geometry, after which any inaccuracies are manually edited accordingly.

3.1.2 Mesh

Mesh Element Properties
The plane-stress condition of the models is enforced through the mesh its element specification. To that end quadrilateral plane-stress elements with 4 nodes and a bi-linear integration scheme have been used. On top of this elements often experience large distortions in the modeling of compliant tissues which can lead to persistent convergence issues in model simulations. To alleviate this problem the elements have been given: (1) a reduced integration scheme to increase element distortion tolerance [45], and (2) hourglass control to combat spurious 'zero energy modes' which can arise due to using a reduced integration scheme.

Mesh Accuracy
The quality of the mesh and the size of the mesh its elements affect the accuracy of simulation outcomes. To enforce a more equal element size over the mesh the editable geometries have been sectioned with vertical and horizontal lines that intersect at the center-point of the BE-FC model its SI. During the tensile test a part of each model is constrained between clamps. To prevent elements in the mesh from crossing said border - which would otherwise cause high local distortions of these elements - the editable geometries have also been sectioned at the two clamp to non-clamp borders. After consideration of the BE-FC geometries (see Fig. 5) and preliminary results, a "free medial axis" meshing algorithm with

mesh transition has been chosen (see [46, 47] for the specifics).

Mesh Convergence
A mesh convergence has been performed for each BE-FC model to determine roughly the minimum amount of elements that is necessary to obtain reliable results from a simulation. To do so each model was replicated with five different meshes - each mesh differing in the amount of elements it has. Subsequently five simulations have been performed for each BE-FC model. Following this the five resulting model force-length relationships have been compared for each BE-FC model. All-in-all the mesh with the smallest amount of elements ánd with a force-length relationship indistinguishable to that of meshes with more elements has been picked for the final model.

3.1.3 Material Model

The Material Formulation
All BE-FC models have been given a Holzapfel-Gasser-Ogden (HGO) material model. This is a phenomenological hyperelastic material formulation suitable for modeling collagen fibre rich biological tissues [48]. In point of fact, it is a constitutive framework for modeling the arterial wall. The HGO material model as implemented in Abaqus is given by equations 1, 2, 3, and 4 [49].

$$U = C_{10}(\bar{I}_1 - 3) + \frac{1}{D}\left(\frac{(J^{el})^2 - 1}{2} - ln(J^{el})\right) + \frac{k_1}{2k_2}\sum_{\alpha=1}^{N}\{exp[k_2\langle\bar{E}_\alpha\rangle^2] - 1\} \tag{1}$$

where

$$\bar{E}_\alpha = \kappa(\bar{I}_1 - 3) + (1 - 3\kappa)(\bar{I}_{4(\alpha\alpha)} - 1) \tag{2}$$

$$J^{el} = \frac{J}{J^{th}}, J^{th} = (1 + \epsilon_1^{th})(1 + \epsilon_2^{th})(1 + \epsilon_3^{th}) \tag{3}$$

$$\kappa = \frac{1}{4}\int_0^\pi \rho(\Theta) sin^3\Theta d\Theta \tag{4}$$

As can be noted the formulae contain many parameters to calculate U, the strain energy per unit of reference volume. In consideration for sections to come the parameters to recognize especially are: D, C_{10}, k_1, k_2, κ, and Θ. D describes the compressibility of the material with $D > 0$. C_{10}, k_1, and k_2 are the material parameters. In specific: C_{10} is a stress-like material constant related to the material its isotropic response with $C_{10} > 0$, k_1 is a stress-like material constant related to the material its anisotropic response with $k_1 > 0$, and k_2 is a dimensionless parameter that also describes the material its anisotropic response with $k_2 > 0$. κ and Θ are the structural collagen fibre parameters. The dispersion of the collagen fibres relative to a mean fibre angle is given by κ with $0 \leq \kappa \leq 1/3$. If $\kappa = 0$ then all fibres are aligned resulting in maximum transverse anisotropy and if $\kappa = 1/3$ the material is said to be fully isotropic. Θ represents the aforementioned mean fibre angle in degrees. Θ is also used to calculate the value of the orientation density function $\rho(\Theta)$.

The HGO material model allows for the modeling of multiple transversely isotropic fibre families with different fibre-related parameter values. The amount of fibre families is specified through N with $N \leq 3$. Because of the method with which κ and Θ are determined, a single fibre family with $N = 1$ has been adopted (to be discussed). Additionally, $\bar{I}_1$ is the first invariant of $\bar{C}$ (distortional part of the right Cauchy-Green strain), $\bar{I}_{\alpha\alpha}$ is the pseudo-invariant of $\bar{C}$ and A_α (set of unit vectors with $\alpha = 1, ..., N$), and lastly J, J^{el} and J^{th} represent the total, elastic, and thermal volume ratios respectively where ϵ_i^{th} indicates the principal thermal expansion strains.

Assigning the HGO model Parameters
In Abaqus the HGO material model requires six parameters to be specified for a single fibre family: D, C_{10}, k_1, k_2, κ, and Θ. How the parameters are acquired is discussed in the following paragraphs. How these parameters are assigned will be discussed first.

The HGO material model is assigned to the elements of the BE-FC model its mesh, the material specification can thereby be varied from element to element. Be that as it may D, C_{10}, k_1, and k_2 are assumed uniform over all elements considering that: (1) D describes the compressibility of the model which is assumed uniform everywhere, and (2) C_{10}, k_1, and k_2 are stress-like or dimensionless material parameters which are likewise assumed consistent all over each BE-FC.

The structural collagen fibre parameters κ and Θ are varied from element to element because the BE-FC its collagen content is observed to vary based upon location. In addition to this - which will become more clear in the following paragraphs - κ and Θ are calculated from the maximum intensity projection collagen content images. This imaging was limited to the tiles in two strips (see Fig. 7). Hence, calculations of κ and Θ are limited to these strips all the while having to define both for the totality of the model. To locally define and assign different parameter values for κ and Θ, the following assumptions have been made and the following approaches have been adopted:

- κ - Assuming vertical similarity the κ parameter values obtained from the collagen imaged tiles in the two strips are spread out vertically, see Fig. 10 subfigures A-C (one κ value per tile in the two strips). Next, the BE-FC model its mesh elements their center-points are calculated, associated with a specific tile if it falls within its boundaries, and given the κ value of that specific tile. Fig. 10 subfigures D.1 and D.2 show that this leads to a sharp contrast in κ between neighbouring elements, which is judged as an unreasonable representation of what is really happening in a biological tissue. Accordingly κ is smoothed out over the elements using a nearest neighbour averaging approach (see Fig. 10 subfigure D.3).
- Θ - Collagen imaging results show two distinct reoccurring Θ arrangements: (1) near the BE-FC its compacted boundaries Θ follows the compacted shape of the BE-FC, and (2) near the BE-FC its center Θ follows the shape of the BE-FC its SI. Accordingly the elements have been given a mean fibre angle Θ as shown in Fig. 11. The approach to do so is elaborated on in the following bullet points and is also (for a large part) shown in Fig. 11.
  - The edges of the BE-FC its SI and its compacted boundaries are identified. Next,

the SI boundary is duplicated and scaled so that a repeating SI pattern forms over the BE-FC geometry. Each edge boundary consists of a multitude of connected points and each of these points is given a direction vector based on the point-to-point direction. This vector is converted to an angle (Θ) relative to the positive X-axis in a right-handed cartesian coordinate system.

- Next, the exact location of all boundary points and the elements their center points is determined.
- The compacted boundary points and the element centres are grouped together (as explained in the following sub-bullet) and the elements are given a collagen fibre mean angle Θ.
  - If an element its center point is within 1 mm of the compacted boundaries, that element is given the angle of a point on said boundaries. In specific, the collagen fibre mean angle Θ given is that of the boundary point with the lowest absolute distance to the element its center point.
- The SI boundary points and all left-over elements centres are grouped together (as explained in the following sub-bullet) and the elements are given a collagen fibre mean angle Θ.
  - All left-over elements are given the angle of a point on one of the SI boundaries. Again, the collagen fibre mean angle Θ of the SI boundary point that has the lowest absolute distance to the element its center point is assigned to the element.
- Finally, the transition of Θ from the compacted-boundary-element-angles group to the SI-element-angles group is improved. The border zone from group to group is taken into account to do so (the zone is specified as being from 0.5 mm to 1.5 mm from the BE-FC its compacted boundaries; i.e. two border zones for each BE-FC model). The elements in these two border zones are identified and the angle between these elements is smoothed using a nearest-neighbour averaging approach.

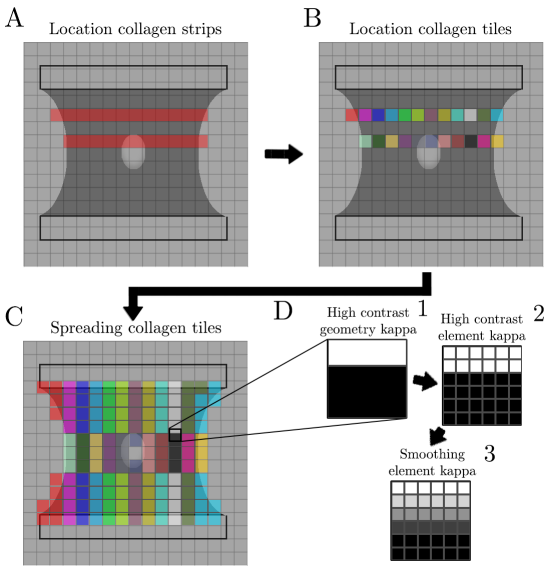

Figure 10: The approach to assign κ to the BE-FC model its elements. Subfigures A and B show the strips (red) and tiles (colored) where collagen is imaged and κ is calculated, respectively. Subfigure C shows how κ is spread out vertically. Subfigures D1 through D3 illustrate how κ is smoothed by use of a nearest neighbour averaging approach.

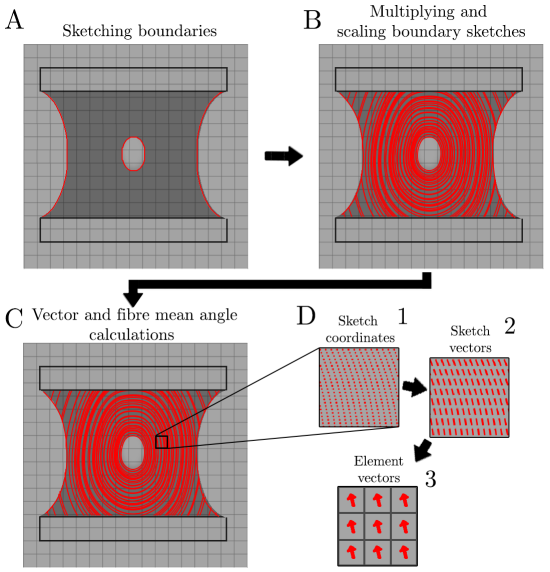

Figure 11: The approach to assign Θ to the BE-FC model its elements. Subfigure A shows the identified boundaries of the BE-FC. Subfigure B shows how the SI its boundary is multiplied and scaled. Subfigures C, D1, D2, and D3 show: (1) how these boundaries are converted from boundary points (sketch coordinates) to orientation vectors (sketch vectors), and (2) how these vectors are assigned to the BE-FC model its elements (element vectors).

Obtaining The HGO Model Parameters (1/2) - [κ & Θ]
The collagen fibre-specific parameters κ and Θ were determined by using the maximum intensity projection collagen images of the BE-FCs. To get meaningful parameters that can be compared accordingly, these images were first processed with Matlab [50] by use of FIBLAB [51]. FIBLAB is an open-source collection of Matlab scripts to determine and assess angular data. Herewith the wrapped (spanning $[0, \pi]$ (radians)) orientation of all the collagen fibres in each image was obtained. This data was used as input for another Matlab script to calculate κ and Θ. The latter script is self-developed and partly based upon the coding framework of FIBLAB. The outline of the steps taken in the two scripts is shown in Fig. 12. The following list elaborates on the details of said steps.

The main concept of the latter-mentioned script to keep in mind is: (1) the collagen fibre orientation data obtained with FIBLAB is used as an independent variable on which a statistical distribution is fitted, (2) fitting is done using an optimization algorithm that iteratively compares the shape of the collagen fibre orientation data and the statistical distribution, (3) the statistical distribution is defined by the collagen fibre mean angle μ (which with optimized parameters is identical to Θ) and a concentration parameter b (which with optimized parameters and a mathematical conversion gives κ).

- The maximum intensity projection collagen image of a tile is loaded into Matlab and FIBLAB is utilized to obtain the orientation of all the collagen fibres in the image. By use of FIBLAB this data is wrapped to a range spanning $[0, \pi]$ (radians).
- By use of a patternsearch optimization a unimodal π-periodic and transversely isotropic von Mises (VM) distribution is fitted upon the collagen fibre orientation data. This provides two directly interpretable parameters: (1) μ = the collagen fibre mean angle (rad) and (2) b = a concentration parameter. The particulars of the VM distribution as well as the fitting of this distribution on the wrapped collagen fibre orientation data with a patternsearch optimization is separately delineated in the following two sub-bullets.
  - *VM distribution*: the VM distribution is described by the orientation density function given by equation 5. Here $\bar{\rho}(\Theta)$ is the VM orientation density function, Θ denotes the collagen fibre mean angle in degrees with $0 \leq \Theta \leq 180$, b is the concentration parameter with $b > 0$, and I_0 - as given by equation 6 - describes the 1st kind 0th order modified Bessel function used to convert the VM distribution to one that is transversely isotropic and π-periodic. For the mathematical derivations leading to this particular VM distribution and a more elaborate explanation see [52].

$$\bar{\rho}(\Theta) = \frac{exp(bcos(2\Theta))}{2\pi I_0(b)} \tag{5}$$

    where

$$I_0(b) = \frac{1}{\pi}\int_0^{\pi} exp(bcos(\Theta))d\Theta \tag{6}$$

  - *Patternsearch optimization*: first of all a VM distribution is created with arbitrary values for Θ and b. The resulting VM distribution is compared with the wrapped

collagen fibre orientation data and the difference between the two is calculated using a mean squared error cost function. Next, the objective is to minimize this difference, i.e. to minimize the mean squared error. To do this the optimization scheme iteratively explores the parameter space values of Θ and b. In other words, the optimization scheme makes a multitude of VM distributions and compares every such distribution to the collagen fibre orientation data. The optimization scheme stops when a mean squared error cost function value is obtained that is satisfactorily low. It is judged out the scope of this report to discuss the modus operandi of the patternsearch optimization scheme; for this the interested reader is referred to [53].

- When a satisfactory fit is obtained, b is converted to κ by use of equations 4, 7, and 8 as described in [52]. The relation between b and κ is visualized in Fig. 13 as obtained from [52]. For these equations Θ is still the collagen fibre mean angle in degrees with $0 \leq \Theta \leq 180$. $\rho(\Theta)$ is described by the density function given by equation 7. $erfi(x)$ describes the imaginary error function given by $erfi(x) = -ierf(x)$ and equation 8.

$$\rho(\Theta) = 4\sqrt{\frac{b}{2\pi}}\frac{exp[b(cos(2\Theta)+1)]}{erfi(\sqrt{2b})} \tag{7}$$

with

$$erf(x) = \frac{2}{\sqrt{\pi}}\int_0^{\pi} exp(-t^2)dt \tag{8}$$

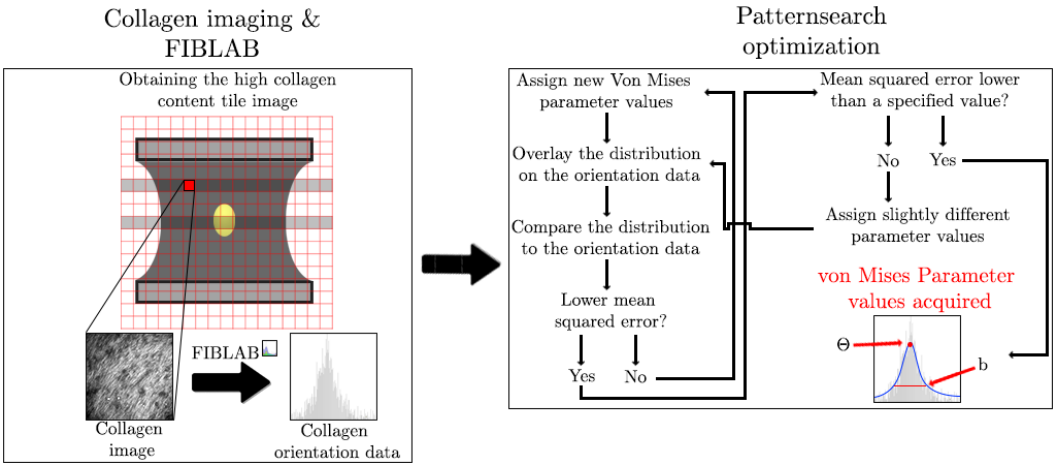

Figure 12: The collagen data post-processing steps. A grid tile its collagen image is used as input for FIBLAB, which provides the image its collagen fibre mean angle. This orientation data is used as input for a patternsearch optimization scheme where a VM distribution is fit upon it, providing the collagen fibre mean angle Θ and the concentration parameter b.

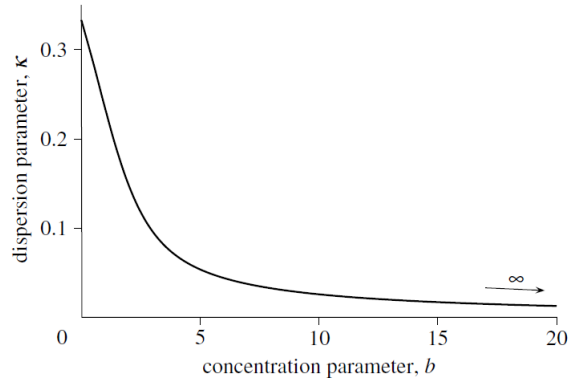

Figure 13: As obtained from [52]. The relation between the π-periodic transversely isotropic VM distribution its concentration parameter b and the collagen fibre dispersion parameter κ.

Obtaining The HGO Model Parameters (2/2) - [D, C_{10}, k_1 & k_2]
The remaining HGO material model parameters to be calculated are D, C_{10}, k_1, and k_2. D describes the incompressibility of a model. All models are assumed to have an unchangeable volume while being deformed and accordingly only isochoric deformation occurs. In other words the models are incompressible and $D = 0.001$ is assigned to the models. The values of C_{10}, k_1, and k_2 were determined with simulations of completed BE-FC models. Yet-to-be discussed model specifics are non-essential for understanding said method.

As a first step to determine C_{10}, k_1, and k_2 the experimental force-length relationship of the BE-FCs were calculated from the clamp-to-clamp distance of the BE-FCs in the tensile tester (see Appendix A), the force-time data from the tensile test, and the applied strain rate (see Appendix A). The experimental force-length relationships also include data about the rupture events. For the current calculations the part of the relationship from just shortly before the point of rupture until the end is simply omitted because damage is not modeled.

The method for finding appropriate values for C_{10}, k_1, and k_2 is somewhat akin to the one used for determining κ and Θ. Using a patternsearch optimization scheme: (1) numerous BE-FC models were created where each such model has different values for C_{10}, k_1, and k_2, (2) simulations were run for each BE-FC model, (3) after each simulation the resulting model force-length relationship was compared to the experimental force-length relationship, and (4) if the difference between the two relationships is satisfactorily low the optimization stops, yielding the parameter values. Fig. 14 as well as the following list are included to clarify the details of these steps.

- First of all the BE-FC model is created with arbitrary values for C_{10}, k_1, and k_2. Boundaries for these parameter values can be specified to decrease the parameter space dimensions to explore, thereby reducing the time necessary for the optimization.
- The BE-FC model is converted to a model input file which is then used as input for the Matlab script. Thereafter this model input file is replicated to a Matlab function file. In this function file the parameter locations are "highlighted" - allowing them to be automatically changed in a programmed script loop.

- For every iteration of the optimization the function file is "called" and new parameter values are passed through to said function file. Following this the function file creates a new BE-FC model input file, with which an Abaqus simulation is performed through Matlab.
- For every iteration of the optimization the model force-length relationship is calculated from the resulting simulation output data file. Hereafter this model force-length relationship is compared to the experimental force-length relationship through the use of a mean squared error cost function.
- The value of the cost function will be lower if the relationships are more alike. When a simulation with specific parameter values leads to a lower cost function value, the next iteration starts with parameter values more approximate to these. The optimization stops after a specified minimum mean squared error value is reached. Once more, the interested reader is referred to [53] for the exact workings of the patternsearch optimization scheme.

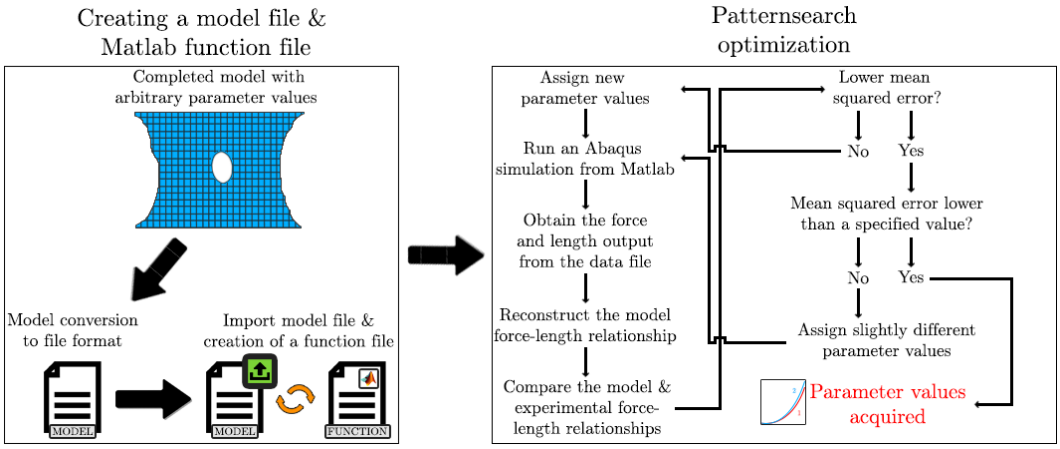

Figure 14: The optimization scheme used for determining the values of C_{10}, k_1, and k_2. A completed BE-FC model with arbitrary values for C_{10}, k_1, and k_2 is converted to a model input file, which is then replicated to a Matlab function file. This function file is called for every iteration of the optimization scheme. Every iteration produces a new model input file with new C_{10}, k_1, and k_2 values. In the end, optimized parameter values for C_{10}, k_1, and k_2 are obtained.

3.1.4 Boundary Conditions

The aim of the models their loading and boundary conditions is to replicate the circumstances of the BE-FCs as they are loaded until failure in the tensile tester. Fig. 15 illustrates the boundary conditions applied to each BE-FC model. Three boundary conditions are applied: (1) an encastre boundary condition, (2) a Y-axis symmetry boundary condition, and (3) a positive Y-direction translation boundary condition. The encastre boundary condition is assigned to each model its bottom clamp area nodes, thereby fixing each model in place. The Y-axis symmetry boundary condition is assigned to each model its top clamp area nodes, constraining each model to only be able to translate in the Y-axis direction. Lastly,

the actual positive Y-direction translation is indirectly imposed on each model its top clamp area nodes with the following steps: (1) a reference point is created above the model, (2) this reference point is coupled to the model its top clamp area nodes, and (3) the positive Y-direction translation is assigned to the reference point. In this way, any translation of the reference point gets applied to the top clamp area nodes.

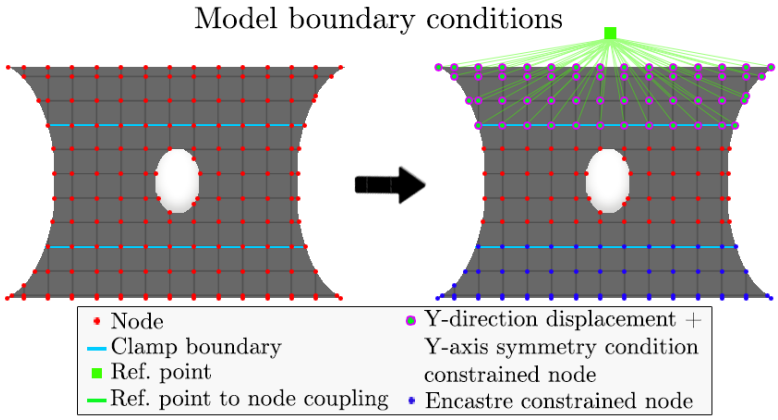

Figure 15: Illustration of the boundary conditions as assigned to the BE-FC models. Ref. point = Reference point.

3.2 Bio-Engineered Fibrous Caps - Idealised Models

To aid the development of future BE-FCs and to gain more insight into the relationship between the BE-FC models their characteristics and the stresses and strains they experience, two distinct batches of idealised BE-FC models have been created. This includes: (1) a morphology model batch and (2) a composition model batch. The first encompasses 1125 models with different geometries while keeping all other model characteristics the same, the latter covers 135 models with different compositions while - again - keeping all other model components the same. All 1260 models are - like the BE-FC models - 2D, plane-stress, and have a SI modeled as a "hole" (see section 3.1 for the reasoning). Hereafter the characteristics of the idealised models are presented in terms of their geometry, mesh, composition, and boundary conditions.

3.2.1 Geometry

Morphology model batch

The models of the morphology model batch each have a distinctive geometry created by changing the value of five geometry-related parameters. The five parameters have been illustrated in Fig. 16, subfigure A (variation in model height and width has not been visualized). As can be observed the parameters include: (1) model height (H), (2) model width (W), (3) the model its SI size in the X-direction (SIx), (4) the model its SI size in the Y-direction (SIy), and (5) the model its left-right boundary compaction (LBc, RBc). In addition Table. 1 presents the exact geometry-related parameter values implemented.

Composition model batch
The models of the composition model batch have identical geometries. This one single geometry has been visualized in Fig. 16 subfigure B. See Table. 1 for the geometry-related parameter values implemented for these models.

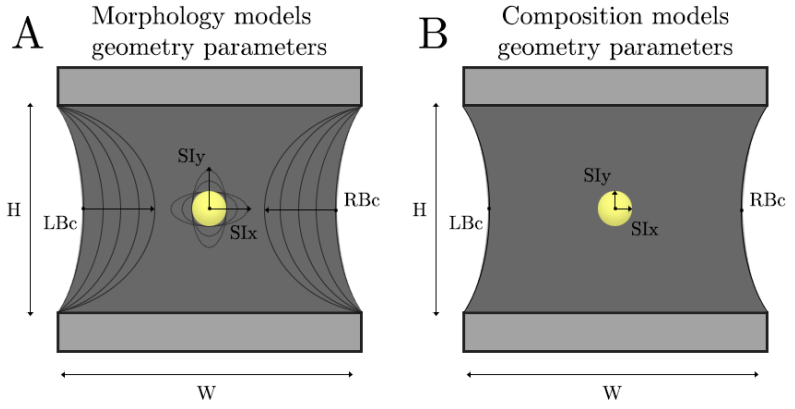

Figure 16: The geometry parameters for the idealised models. The parameters are: (1) model height (H), (2) model width (W), (3) the model its SI size in the X-direction (SIx), (4) the model its SI size in the Y-direction (SIy), and (5) the model its degree of boundary compaction (LBc, RBc). Subfigure A: the geometry parameters for the idealised morphology models. Subfigure A visualizes how these parameters are varied and what geometry results therefrom. Subfigure B: the geometry parameters for the idealised composition models. Note that the parameter values are identical between the idealised composition models.

Table 1: An overview of the geometry parameters their values for the idealised models. Boundary compaction (LBc, RBc) is defined as the shift of the compacted boundary its midpoint (at midpoint height = $H/2$) towards the SI; an increase in the value of LBc and RBc results in an increase of boundary compaction. Here $n = [0, 1, 2, 3, 4]$, $m = [0, 1, 2]$, $q = 1$ for the left compacted boundary, and $q = W - 1$ for the right compacted boundary.

	Height (H) [mm]	**Width (W) [mm]**	**SI X-size (SIx) [mm]**	**SI Y-size (SIy) [mm]**	**Boundary compaction (LBc, RBc) [mm]**
Morphology models	$10 + n \cdot 1.25$	$10 + n \cdot 1.25$	$1 + m \cdot 0.2$	$1 + m \cdot 0.2$	$q + n \cdot 0.5$
Composition models	10	15	1	1.4	q + 1

3.2.2 Mesh

The mesh characteristics of the idealised models are near-identical to that of the real BE-FC models (for the reasoning see section 3.1.2). All meshes are assigned 2D quadrilateral plane stress elements with a reduced integration scheme and hourglass control. In addition - before applying a mesh - the geometries have been sectioned at the clamp to non-clamp

borders. The clamp to clamp distance is set as being variable due to a changing of the (morphology) models their height (H); the clamp borders are set at a Y-direction distance of $\pm H/4$ from the model its midpoint. Having sectioned the model geometries the mesh is applied by using a free medial axis meshing algorithm with mesh transition enabled. To conclude no mesh refinement is performed because: (1) a fine mesh is used for all models, and (2) the models have a smooth and simple geometry.

3.2.3 Material Model

All idealised models have been assigned the HGO material model (for the reasoning and the material model specifics see section 9). This material model requires six parameters to be defined: D, C_{10}, k_1, k_2, Θ, and κ. The HGO material model is assigned to the elements of the idealised models their mesh. The parameter values of D, C_{10}, k_1, and k_2 are - as done for the BE-FC models - uniform over the elements of each idealised model its mesh. Per contra to what was done for the BE-FC models, this uniformity is now also implemented for κ. Lastly, Θ remains element-specific.

Morphology model batch
The models of the morphology model batch have identical HGO material model parameter values. See Table. 2 for the assigned parameter values. D its parameter value is identical to the value assigned to the BE-FC models, see section 9 for the reasoning. The parameter values for C_{10}, k_1, and k_2 have been adopted from BE-FC sample number 3 as this BE-FC is relatively symmetric and rectangular. The collagen fibre dispersion κ its value is chosen such that it lies within the range commonly observed for the BE-FC models. Θ is the only element-specific parameter, is again assumed ideal, and is assigned to the models using the same method as used for the BE-FC models (see section 9). The to-be-smoothed collagen fibre mean angle Θ has been visualised in Fig. 17 for one illustrative idealised model.

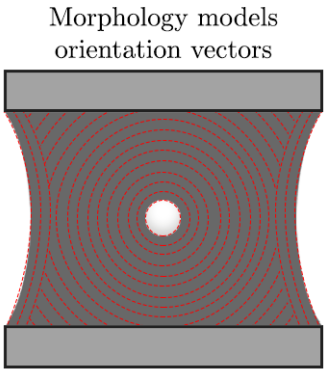

Figure 17: An illustration of the idealised morphology models their collagen fibre mean angles Θ. Near the compacted boundaries Θ follows said boundaries and everywhere else Θ follows the shape of the SI.

Composition model batch
Each idealised composition model has distinctive HGO material model parameter values. Table. 2 presents said values. For all composition models the parameters that are identical

in-between are D and Θ. These two parameters have values equivalent to what is assigned to the idealised morphology models. The parameter values of C_{10}, k_1, k_2, and κ are varied. These four parameters were increased or decreased in value starting from the values assigned to the morphology models, Table. 2 presents the specifics.

Table 2: An overview of the HGO material model parameter values for both the idealised morphology models as well as the idealised composition models. Here n = [0,1,2] and m = [0,1,2,3,4].

#	D	C_{10}	k_1	k_2	κ
Morphology models	0.001	0.2023	2.75	1.85	0.23
Composition models	0.001	$(0.2023 - 0.2023/10) + n \cdot (0.2023/10)$	$(2.75 - 2.75/10) + n \cdot (2.75/10)$	$(1.85 - 1.85/10) + n \cdot (1.85/10)$	$0.23 + m \cdot (0.23/10)$

3.2.4 Boundary Conditions

All idealised models have the same boundary conditions. In addition, these conditions are identical to the ones imposed upon the real BE-FC models. For the specifics of the conditions, a referral is therefore made to section 3.1.4 and Fig. 15. The only contrast is the amount of displacement applied to the idealised models. To approach the BE-FC tensile tester circumstances the displacement applied to the idealised models is set at half their clamp-to-clamp distance ($H/4$).

4 Results

A substantial degree of similarity between the BE-FC models was observed. Subsequently only the specifics of BE-FC sample number 3 are presented here as a representative example (the BE-FC of which data is used for the idealised models), see Fig. 18. The specifics of all BE-FC models can be examined in Appendix B.

Fig. 18 shows that the model geometry accurately fits the BE-FC its imaged planar shape. Further, the fibre dispersion κ assigned to the geometry its elements has an apparent vertical spread and a smooth element-to-element gradient. The other material model collagen parameter - the fibre mean angle Θ - follows the shape of the SI everywhere except near the compacted boundaries of the geometry, where it follows said boundaries. Furthermore, a moderate Θ gradient can be observed between these two groups with distinct fibre mean angles. Fig. 18 subfigure E shows that the global model behaviour approximates the experimentally obtained one. Nonetheless, three points of inequality between the two can be deduced (which are also persistent for multiple other BE-FC models, see appendix B). In sequence with an increasing strain the model relationship relative to the experimentally obtained one: (1) overestimates, (2), slightly underestimates, and then at the end (3) slightly overestimates the force.

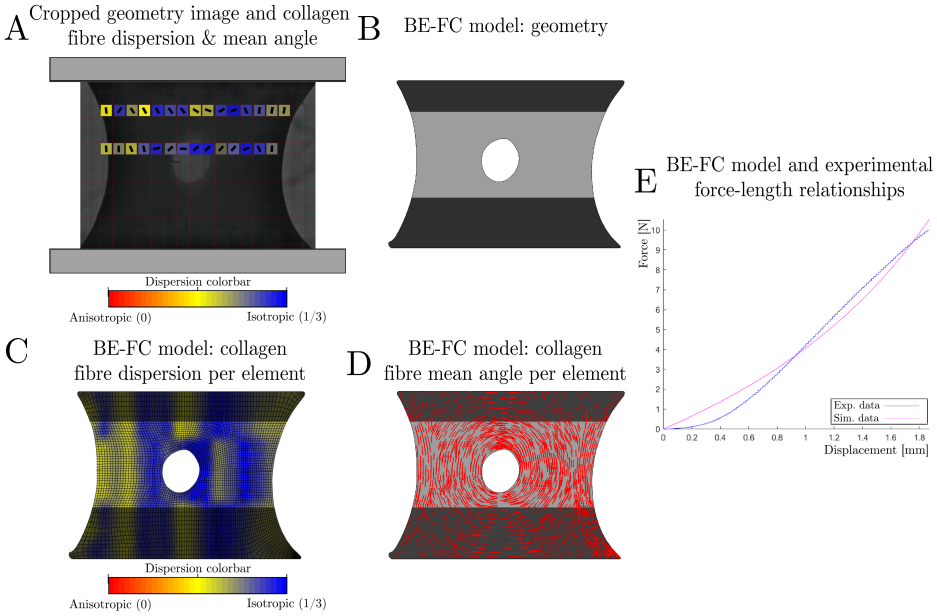

Figure 18: The characteristics of BE-FC model number 3. Subfigure A: the BE-FC its cropped geometry image including the calculated collagen fibre dispersion κ and mean angle Θ for the tiles where collagen is imaged. Tile color = degree of fibre dispersion. Vector within a tile = fibre mean angle. Subfigure B: the model geometry. Dark grey areas: geometry region which is fixed between the tensile tester its clamps. Light grey areas: the non-fixed geometry region. Subfigure C: the model its collagen fibre dispersion κ. Subfigure D: the model its collagen fibre mean angles Θ. Subfigure E: both the model and the experimental force-length relationship ("Sim. data" and "Exp. data", respectively).

4.1 Bio-engineered Fibrous Cap Models

To allow for the investigation of stresses and strains globally as well as within or across the collagen fibres, the model simulation results are presented in two different sets of coordinate systems. This includes: (1) a single global right-handed cartesian coordinate system (X-axis rightwards and Y-axis upwards), and (2) many local right-handed cartesian coordinate systems conforming to the fibres of the elements ("local output", one system per element, X-axis along the element its fibre and the Y-axis across it).

A total of six normal and four local stresses and strains have been investigated: (1) the shear stresses and strains (S_{xy} & LE_{xy}), (2) the stresses and strains in the X-direction (S_x & LE_x), (3) the stresses and strains in the Y-direction (S_y & LE_y), (4) the local stresses and strains along the collagen fibres ($S_{\text{in-fib}}$ & $LE_{\text{in-fib}}$), and lastly (5) the local stresses and strains across the collagen fibres ($S_{\text{across-fib}}$ & $LE_{\text{across-fib}}$).

4.1.1 Stress & Strain - Peak Values

The rupture of a BE-FC is assumed to correlate with the highest stresses it experiences. Along with that these stresses are closely related to the strains a BE-FC sustains during elongation. Accordingly, the peak values of both the stresses and strains in all BE-FC models are presented in Fig. 19. Tables presenting the exact values can be examined in Appendix C. Note that only positive values are presented for LE_x, LE_{xy}, and S_{xy} in Fig. 19, yet these stresses and strains can also be negative in the models. The results are presented in this manner because: (1) the sign of S_{xy} and LE_{xy} only signifies a directional change, and (2) presenting the absolute peak values of LE_x allows a better comparison between peak values of the strains.

Considering Fig. 19 it can be noted that there are two stresses with especially high peak values for all BE-FC models; S_y and $S_{\text{in-fib}}$. In specific, S_y has a median of 3.151 [2.407, 3.896] MPa ([interquartile range]) and $S_{\text{in-fib}}$ has a median of 3.2555 [2.352, 4.159] MPa. Within one model the two stresses approach each other. Per contra, they can differ considerably in-between models. S_x, S_{xy}, and $S_{\text{across-fib}}$ have considerably lower peak values; S_x has a median of 0.596 [0.315, 0.876] MPa, S_{xy} has a median of 1.01 [0.585, 1.428] MPa, and $S_{\text{across-fib}}$ has a median of 0.771 [0.255, 1.29] MPa. Also, these peak stresses are generally comparable within one BE-FC model but can differ considerably in-between the BE-FC models.

The strains with the highest peak values are LE_y, LE_{xy}, $LE_{\text{in-fib}}$, and $LE_{\text{across-fib}}$. LE_y has a median of 0.402 [0.321, 0.483], LE_{xy} has a median of 0.419 [0.357, 0.480], $LE_{\text{in-fib}}$ has a median of 0.396 [0.309, 0.484], and $LE_{\text{across-fib}}$ has a median of 0.292 [0.197, 0.386]. The largest of these is LE_{xy} for a majority of the models. Still and all, LE_y, $LE_{\text{in-fib}}$, and $LE_{\text{across-fib}}$ generally approach LE_{xy}. Lastly, LE_x is generally by far the smallest of strains in the models and has a median of 0.189 [0.145, 0.233].

4.1.2 Stress & Strain - Peak Values Locations

Apart from the peak values of the strains and stresses in the BE-FC models, the locations thereof are also meaningful when investigating a BE-FC its biomechanical behaviour and/or

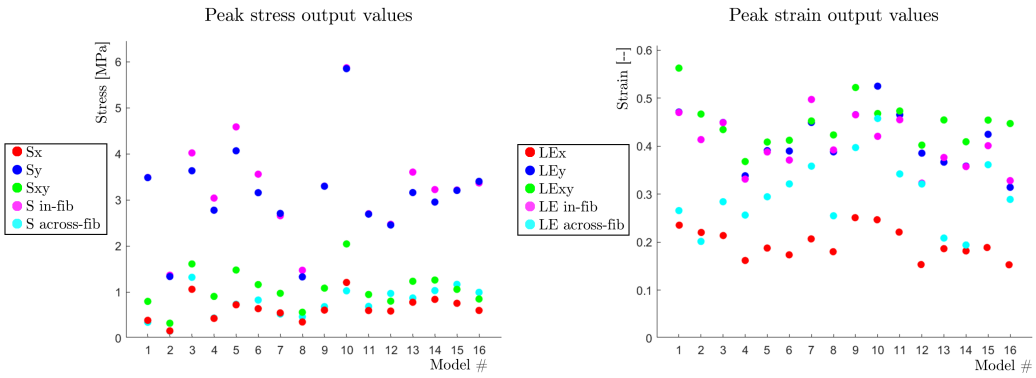

Figure 19: The peak values of the stresses and strains in the BE-FC models.

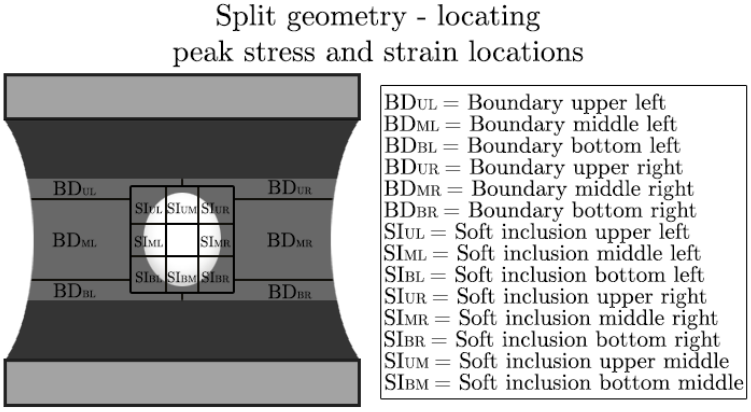

Figure 20: An illustrative split BE-FC geometry with naming for each region to locate the stress and strain peak values on the BE-FC models.

rupture. To methodically pinpoint these locations the models were split into the 14 regions shown in Fig. 20. Subsequently using these regions, the peak stress and strain value locations were determined. After having done so these locations were compared with the experimentally obtained BE-FC rupture initiation locations.

Ultimately no clear relationship was found between: (1) any of the BE-FC models their peak stress and strain locations, and (2) the experimentally obtained BE-FC rupture initiation locations. Using the naming of the regions in Fig. 20, the actual BE-FC rupture initiation locations as well as the models their peak stress and strain value locations are given in Appendix D.

4.1.3 Stress & Strain - Distributions

Stress and strain peak values as well as the locations thereof do not clarify the stresses and strains over the whole of the models. Nonetheless, such knowledge aids in clarifying the BE-FCs their biomechanical behaviour and gives insight into the effect of modeling choices.

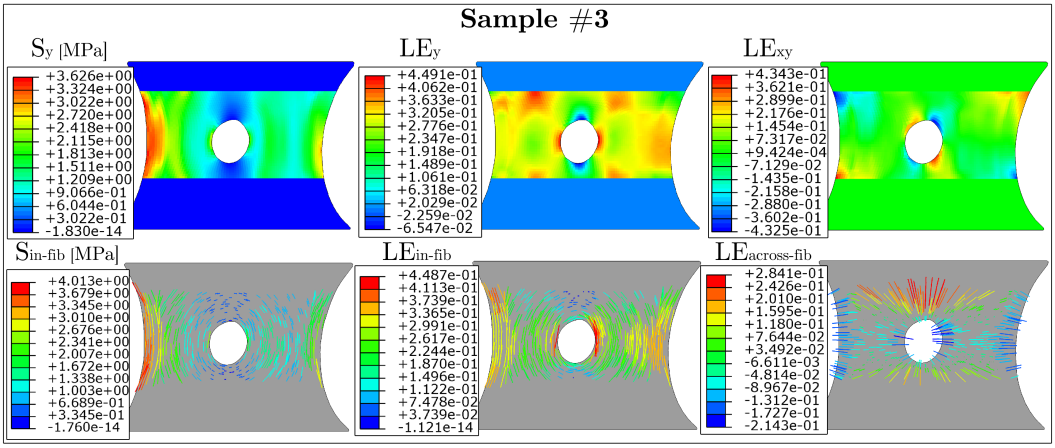

Figure 21: The stress and strain distributions of BE-FC model sample number 3. Six distributions can be seen, including that of: S_y, $S_{\text{in-fib}}$, LE_y, LE_{xy}, $LE_{\text{in-fib}}$, and $LE_{\text{across-fib}}$.

Accordingly, the distributions of the six stresses and strains in the models with the highest peak values were investigated (i.e., the distributions of S_y, $S_{\text{in-fib}}$, LE_y, LE_{xy}, $LE_{\text{in-fib}}$, and $LE_{\text{across-fib}}$). It was observed that the distributions are alike between the BE-FC models. Therefore - and in accordance with the approach taken for presenting the models their characteristics - the stress and strain distributions of BE-FC sample number 3 are presented in Fig. 21. The distributions of all models are presented in Appendix E.

Stress distributions

Fig. 21 shows that S_y and $S_{\text{in-fib}}$ have alike distributions. Further, both stresses are high near the compacted boundaries of the model - in particular near its left compacted boundary. Per contra, the stresses are especially low above and under the SI, and have moderate values everywhere else in the BE-FC model.

Strain distributions

LE_y is relatively high in three regions of the BE-FC model: near its compacted boundaries and particularly so near its right boundary, directly to the left and right of its SI, and diagonally around its SI near its clamps. Per contra LE_y is low above and under the model its SI, near its corners, and in the area halfway between its SI and its compacted boundaries. The $LE_{\text{in-fib}}$ distribution is similar to that of LE_y; $LE_{\text{in-fib}}$ is high directly left and right to the SI as well as near the model its compacted boundaries. Over and above that $LE_{\text{in-fib}}$ is low near the clamps and particularly so above and under the SI. The $LE_{\text{across-fib}}$ distribution is a counterpart of the $LE_{\text{in-fib}}$ distribution. $LE_{\text{across-fib}}$ is high above and under the SI with in comparison particularly high values above it. Moreover, $LE_{\text{across-fib}}$ decreases from these two locations towards the compacted boundaries. Further, $LE_{\text{across-fib}}$ is low everywhere else in the BE-FC model. As a final observation LE_{xy} is high diagonally around the model its SI and at its corners.

Table 3: An overview showing which model parameters have an appreciable effect on which stress and strain its peak value. ↑ = a gain in the model parameter increases the stress/strain its peak value. ↓ = a gain in the model parameter decreases the stress/strain its peak value. "-" a gain in the model parameter does not affect the stress/strain its peak value.

	S_y	$S_{\textbf{in-fib}}$	LE_{xy}	LE_y	$LE_{\textbf{in-fib}}$	$LE_{\textbf{across-fib}}$
Model height	↑	↑	↑	↑	↑	↑
Model width	↓	↓	↑	↑	-	↑
Model compaction	↑	↑	↓	-	↑	↓
Model SI X-size	-	-	-	↓	-	↓
Model SI Y-size	-	-	-	↑	-	↑
C_{10}	↑	↑	-	-	-	-
k_1	↑	↑	-	-	-	↑
k_2	↑	↑	-	-	-	-
κ	↓	↓	↑	↑	↑	↓

4.2 Idealised Models

The simulation results of the idealised models allow for a better understanding of the BE-FC models their biomechanical behaviour. Following the methodology of the previous subsections, the same stresses and strains are investigated as presented before. Further, both the peak values and the distributions of these stresses and strains will be presented.

4.2.1 Stress & Strain - Peak Values

To get an approximate grasp on the peak values of the stresses and strains in the idealised models, Fig. 22 presents boxplots thereof without discriminating between the idealised morphology models (Fig. 22 subfigure A) and the idealised composition models (Fig. 22 subfigure B). In accordance with the results presented for the BE-FC models, the stresses and strains with the highest peak values are S_y, $S_{\text{in-fib}}$, LE_y, LE_{xy}, $LE_{\text{in-fib}}$, and $LE_{\text{across-fib}}$. The further presented results will be limited to these six stresses and strains.

Figures 23 and 24 present the same data as presented in Fig. 22, but take into account the model subcategories that arise from model parameter changes (e.g. models with a height of H = 10 mm are grouped, models with a height of H = 15 mm are grouped, and the results of these models are presented per group). The figures present several noteworthy observations as to which model parameter increases or decreases which stress and/or strain its peak value. These observations are delineated in Table. 3.

Presenting the results in this manner still has a disadvantage; model subcategories still consist of idealised models with many different model parameters. For instance, the models within the first model height subcategory (H1) all have a height of 10 mm but differ in-between in other model parameters such as model compaction and model width. Consequently the relation between a model parameter change and a stress/strain its peak value could still be obscured. However, within a single isolated group of models, the in figures 23 and 24 observed relations are preserved (see Appendix F).

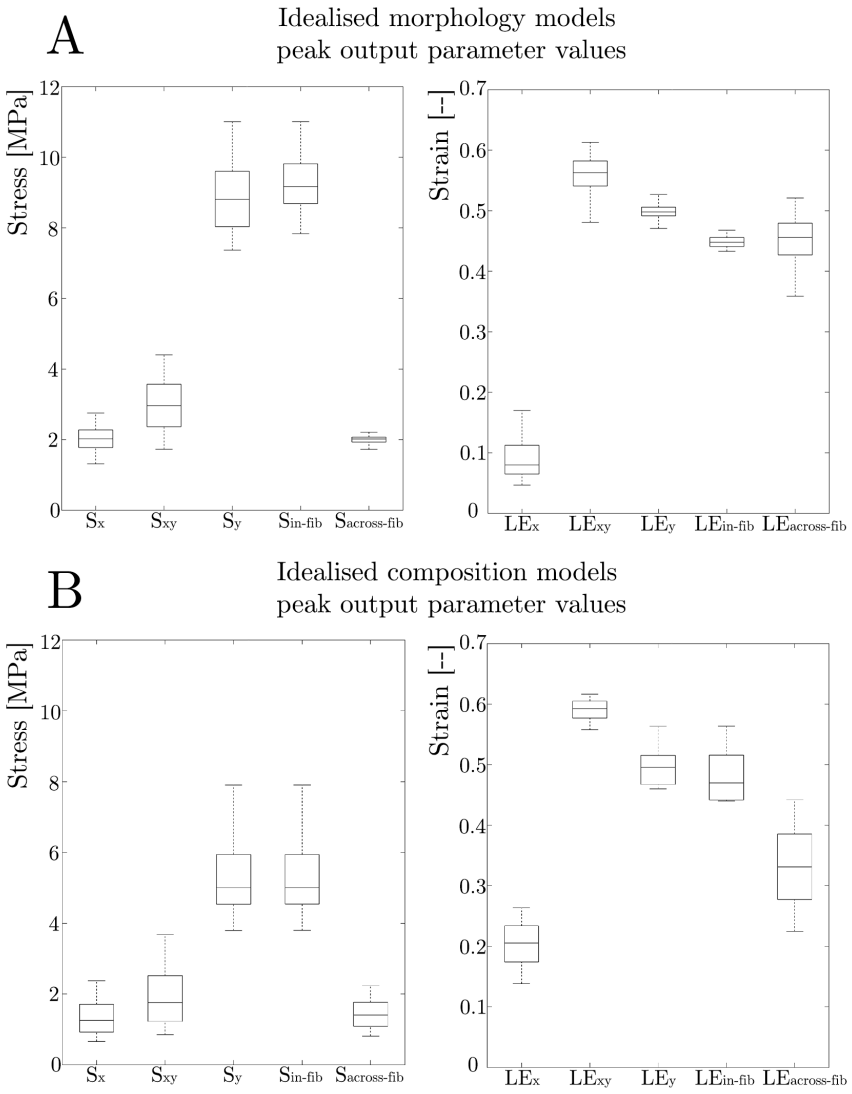

Figure 22: Boxplots of the peak values of the stresses and strains in the idealised models without differentiating between the morphology models (subfigure A) or the compositions models (subfigure B).

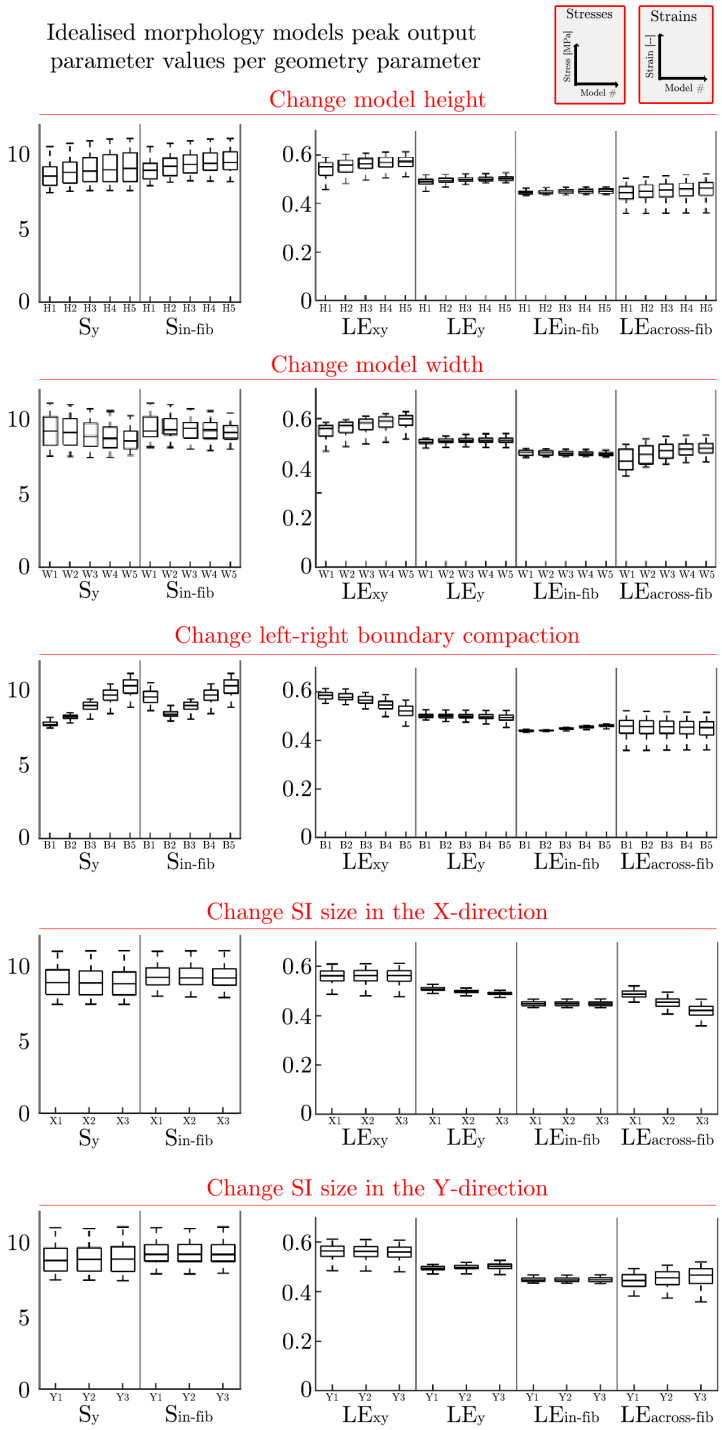

Figure 23: Boxplots of the stresses and strains their peak values in the idealised morphology models per model subcategory (e.g. changing model height). The X-axes of the plots correspond linearly (from lowest to highest values assigned) with the parameter values as presented in Tables 1 and 2.

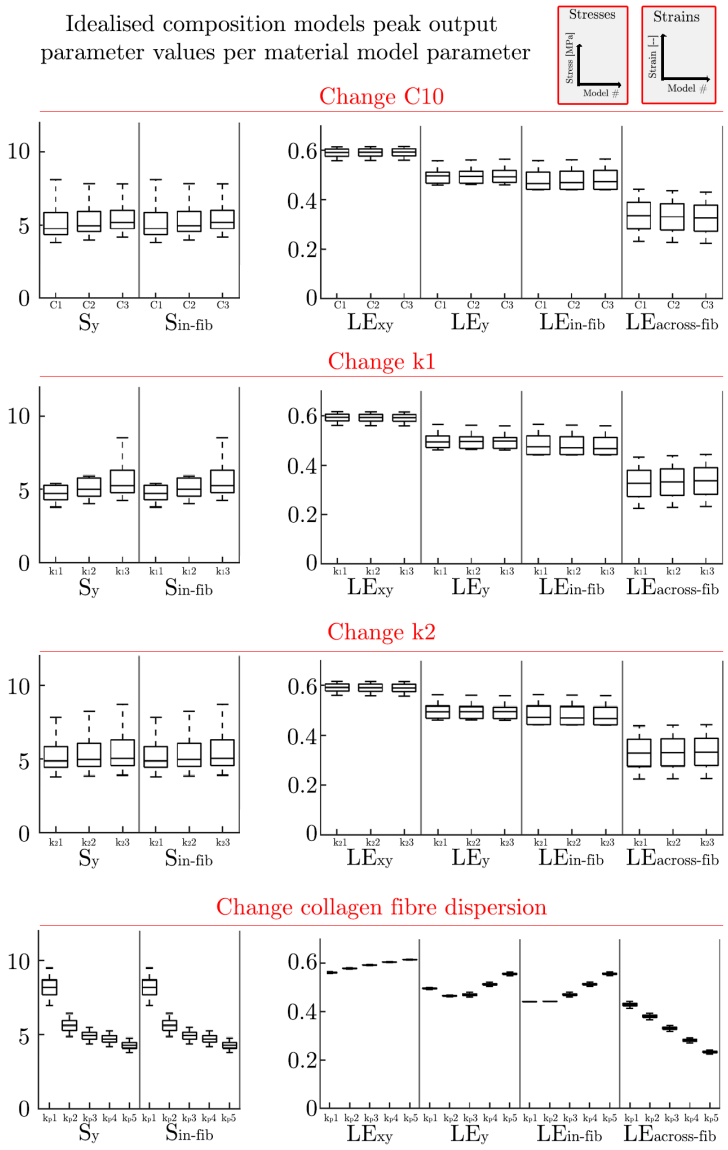

Figure 24: Boxplots of the stresses and strains their peak values in the idealised composition models per model subcategory (e.g. changing a model its collagen fibre dispersion κ). The X-axes of the plots correspond linearly (from lowest to highest values assigned) with the parameter values as presented in Tables 1 and 2.

Table 4: An overview showing which model parameters have an appreciable effect on which stress and strain its distribution.

	S_y	$S_{\textbf{in-fib}}$	LE_{xy}	LE_y	$LE_{\textbf{in-fib}}$	$LE_{\textbf{across-fib}}$
Model height			x	x	x	x
Model width				x	x	
Model compaction	x	x	x		x	
Model SI X-size	x	x	x	x	x	x
Model SI Y-size	x	x	x	x	x	x
C_{10}						
k_1	x	x				
k_2	x	x				
κ	x	x	x	x	x	x

4.2.2 Stress & Strain - Distributions

The presented relations between the model parameters and the peak values of the stresses and strains do not necessarily correspond closely to the relations between the model parameters and the distributions of the stresses and strains. Accordingly, said relations have been investigated. This has been done in a qualitative manner, i.e. by visual inspection. If a model parameter appreciably affects a stress and/or strain its distribution, the relation between the two has been marked. The results hereof are presented in Table. 4 and distributions will be presented for the marked stress/strain-model parameter combinations. In addition - to present unambiguous results - the distributions belong to models which differ in a single model parameter in-between. For instance, the effect of model height on the LE_y distribution is shown by presenting distributions of models with variable model height but fixed and matching model width, compaction, and SI size. The fixed geometry and material model parameters correspond to the ones assigned to the idealised composition models and the idealised morphology models, respectively.

S_y & $S_{\textbf{in-fib}}$ distribution
The S_y and $S_{\text{in-fib}}$ distributions are shown in figures 25 and 26, respectively. The distributions of these two stresses are alike. In particular and apart from models with a high fibre dispersion κ, high stresses are limited to the middle of the compacted boundaries. Further, the stresses are particularly low above and under the SI. The effect of a model parameter on the distributions of S_y and $S_{\text{in-fib}}$ is also similar. A gain in compaction, k_1, and/or k_2 increases the stresses at the compacted boundaries. Moreover, a gain in compaction also clusters these stresses to the middle of said boundaries. A gain in the SI its size in the Y-direction increases the stresses directly to the left and right of the SI. A gain in the SI its size in the X-direction decreases the stresses above and under the SI. Lastly, the stress distributions most significantly change with a gain in the fibre dispersion κ. A gain therein considerably decreases the stresses in the models. Moreover, in very isotropic models - models with a very high fibre dispersion κ - the stresses are highest to the left and right of the SI.

LE_{xy} distribution
Fig. 27 presents the LE_{xy} distributions. All models experience a high LE_{xy} diagonally above and under their SI as well as at their corners. A gain in compaction and/or height

increases LE_{xy} at the corners of the models. A gain in the SI its size in the X-direction slightly increases LE_{xy} in the model areas diagonally around the SI. A gain in the SI its size in the Y-direction slightly increases LE_{xy} directly and diagonally above and under the SI. Lastly, a gain in the fibre dispersion κ increases LE_{xy} diagonally above and under the SI as well as at the corners of the models. However, the areas with high LE_{xy} in the model its corners decrease in size.

LE_y distribution
The LE_y distributions are shown in Fig. 28. Excluding very isotropic models, LE_y is high near the clamps diagonally above and under the SI as well as around the middle of the compacted boundaries. Moreover, in these models LE_y is especially low above and under the SI. The geometry parameters each affect the LE_y distribution differently. A gain in model height increases LE_y near the clamps. A gain in model width increases LE_y in the two areas between the SI and the compacted boundaries. A gain in the SI its size in the X-direction decreases LE_y above and under the SI and a gain in the SI its size in the Y-direction increases LE_y in the areas left and right to the SI. The LE_y distribution most significantly changes with a gain in the fibre dispersion κ. For very isotropic models LE_y is especially high directly left and right to the SI. Moreover, LE_y is also considerable in the two areas demarcated by the clamps, the middle of the compacted boundaries, and the left/right border of the SI. Lastly, LE_y is particularly low above and under the SI.

$LE_{\text{in-fib}}$ distribution
Fig. 29 presents the $LE_{\text{in-fib}}$ distributions. The typical distribution shows a high $LE_{\text{in-fib}}$ near the compacted boundaries that extends towards the SI. In addition, $LE_{\text{in-fib}}$ is low above and under the SI. A change in model geometry has a conservative effect on this distribution. A gain in model height decreases $LE_{\text{in-fib}}$ at the clamps while a gain in model width increases it there. A gain in model compaction increases $LE_{\text{in-fib}}$ at the compacted boundaries, especially around the middle thereof. A gain in the SI its size in the X-direction decreases $LE_{\text{in-fib}}$ above and under the SI while a gain in the SI its size in the Y-direction increases $LE_{\text{in-fib}}$ to the left and right of the SI. The fibre dispersion κ affects the $LE_{\text{in-fib}}$ distribution the most. A gain in the fibre dispersion κ considerably increases $LE_{\text{in-fib}}$ to the left and right of the SI. Apart from this observation and considering the higher peak value of $LE_{\text{in-fib}}$ for these five model distributions, the distribution does not change otherwise.

$LE_{\text{across-fib}}$ distribution
The $LE_{\text{across-fib}}$ distributions are shown in Fig. 30. The typical $LE_{\text{across-fib}}$ distribution shows high values above and under the SI with a decrease thereof towards the compacted boundaries. In addition $LE_{\text{across-fib}}$ is low everywhere else. The model parameters affect $LE_{\text{across-fib}}$ above and under the SI. A gain in model height and a gain in the SI its size in the Y-direction increases $LE_{\text{across-fib}}$ there. Per contra, a gain in the SI its size in the X-direction and a gain in the fibre dispersion κ decreases it in these two locations.

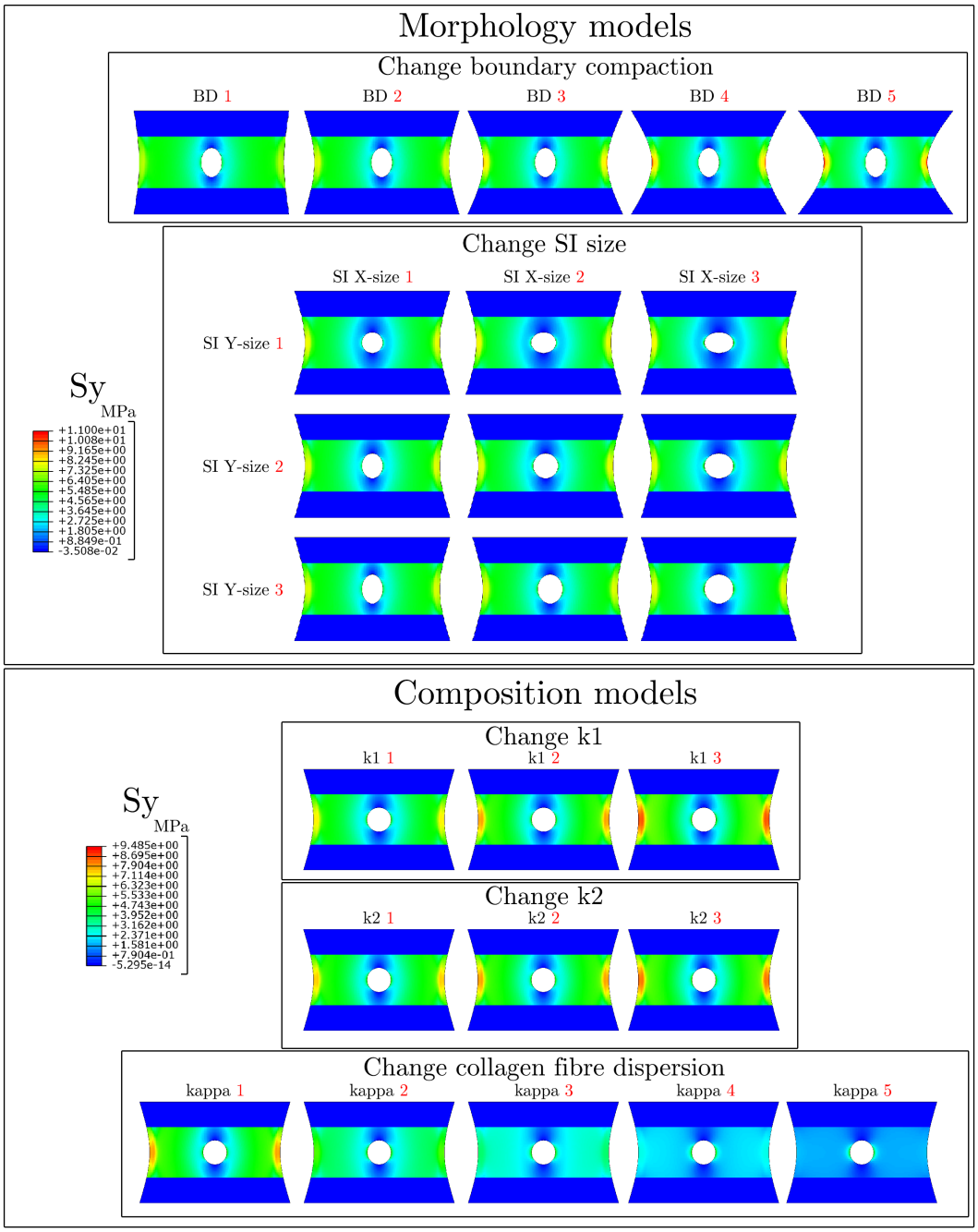

Figure 25: S_y distributions for a selection of idealised morphology and composition models. The model parameter differing between the distributions is displayed above and/or next to its particular distribution (e.g. "k_2 1"). The model parameter values correspond linearly (from lowest to highest values assigned) with the parameter values as presented in Tables 1 and 2.

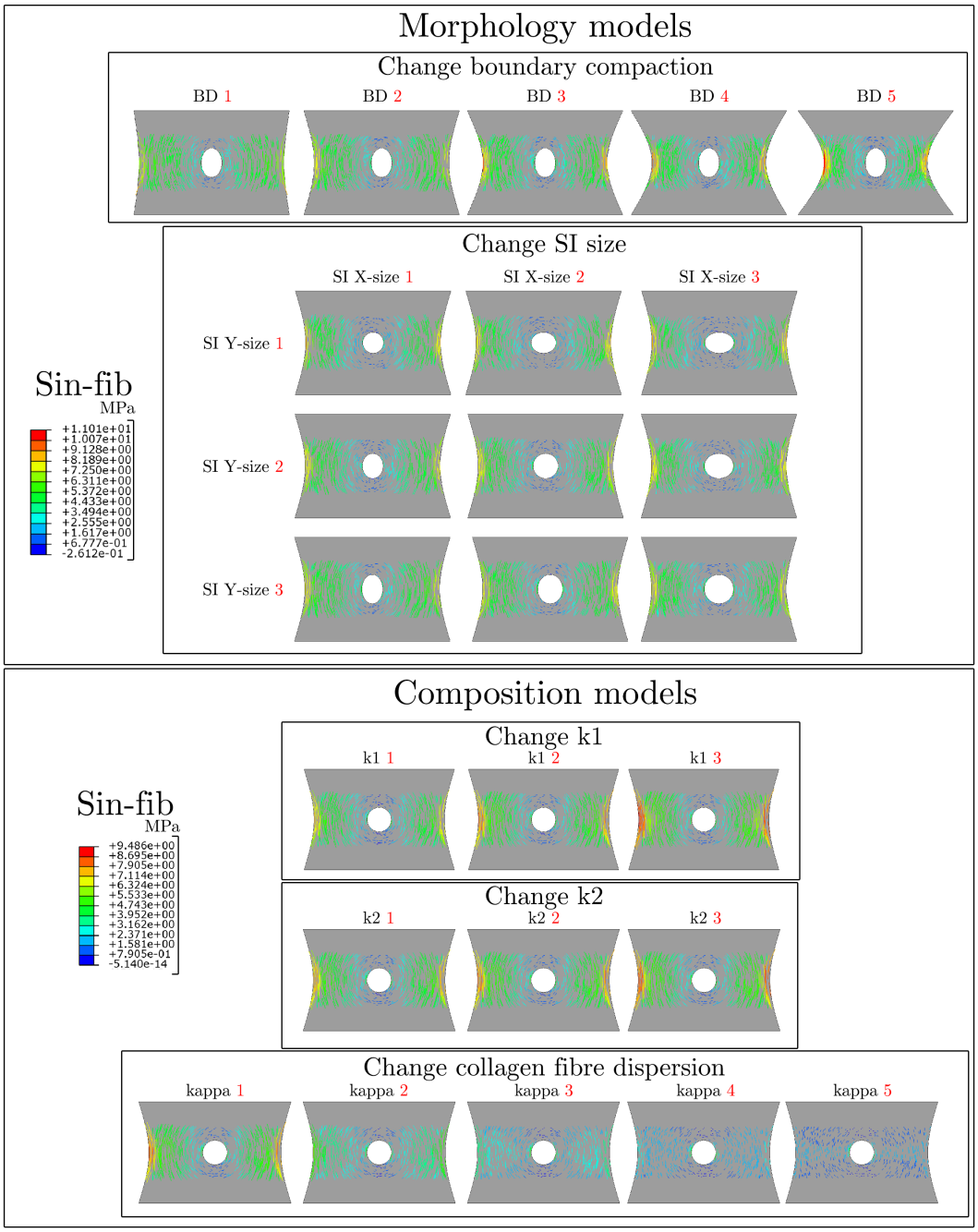

Figure 26: $S_{\text{in-fib}}$ distributions for a selection of idealised morphology and composition models. The model parameter differing between the distributions is displayed above and/or next to its particular distribution (e.g. "k_2 1"). The model parameter values correspond linearly (from lowest to highest values assigned) with the parameter values as presented in Tables 1 and 2. Note that some distributions seem slightly asymmetrical. This is due to the fact that $S_{\text{in-fib}}$ is shown for 70% of all elements of the model.

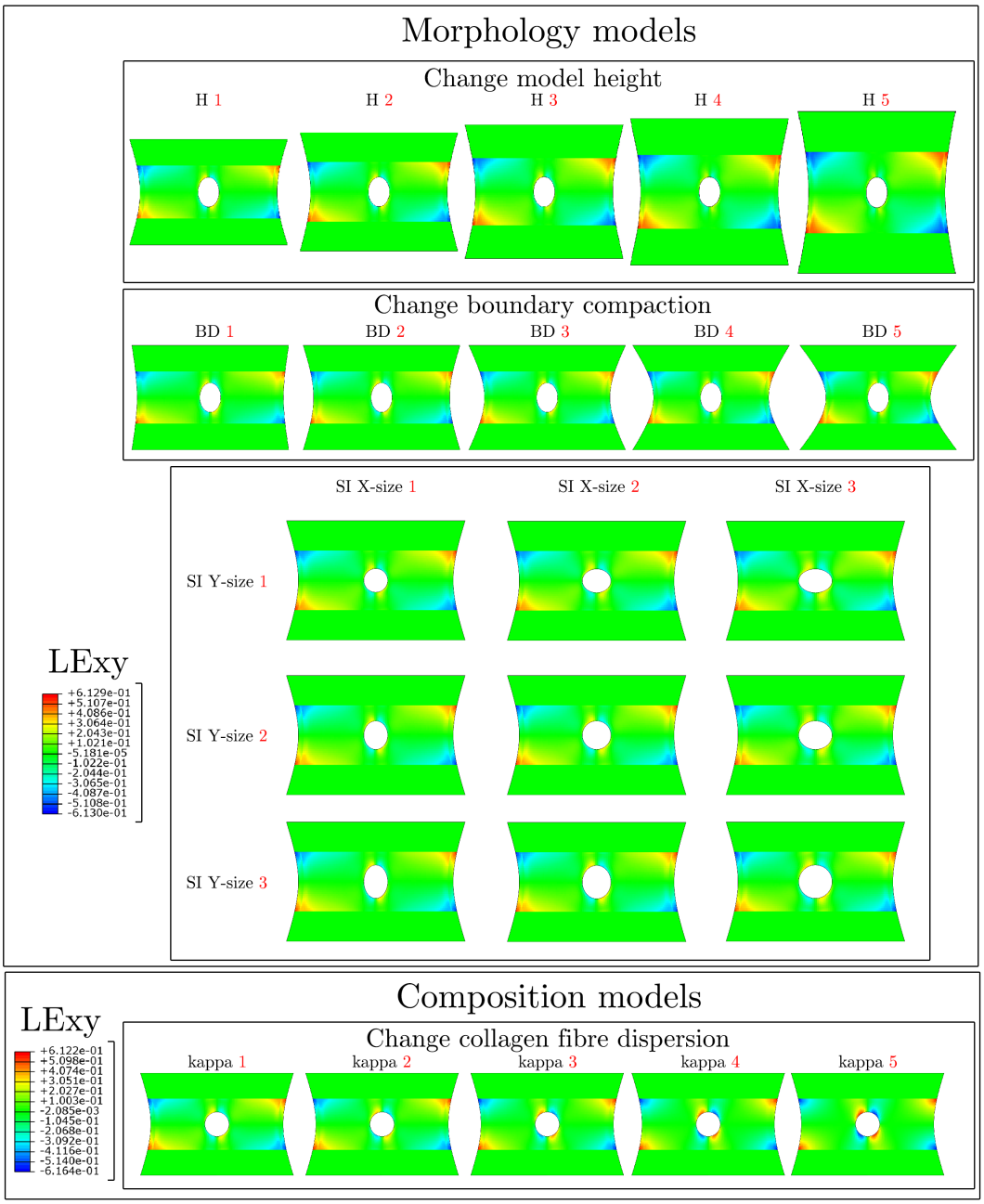

Figure 27: LE_{xy} distributions for a selection of idealised morphology and composition models. The model parameter differing between the distributions is displayed above and/or next to its particular distribution (e.g. "kappa 1"). The model parameter values correspond linearly (from lowest to highest values assigned) with the parameter values as presented in Tables 1 and 2.

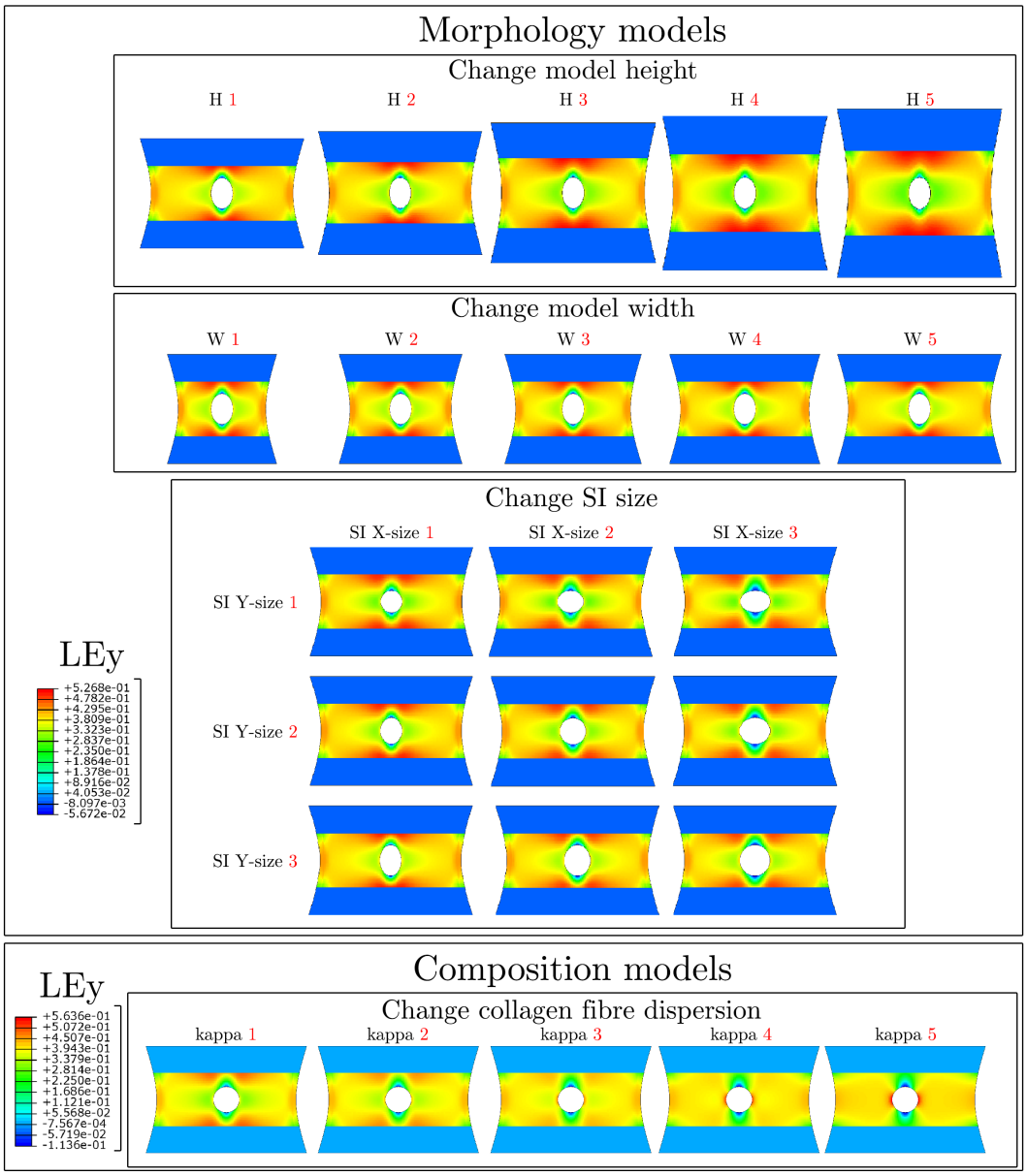

Figure 28: LE_y distributions for a selection of idealised morphology and composition models. The model parameter differing between the distributions is displayed above and/or next to its particular distribution (e.g. "W 1"). The model parameter values correspond linearly (from lowest to highest values assigned) with the parameter values as presented in Tables 1 and 2.

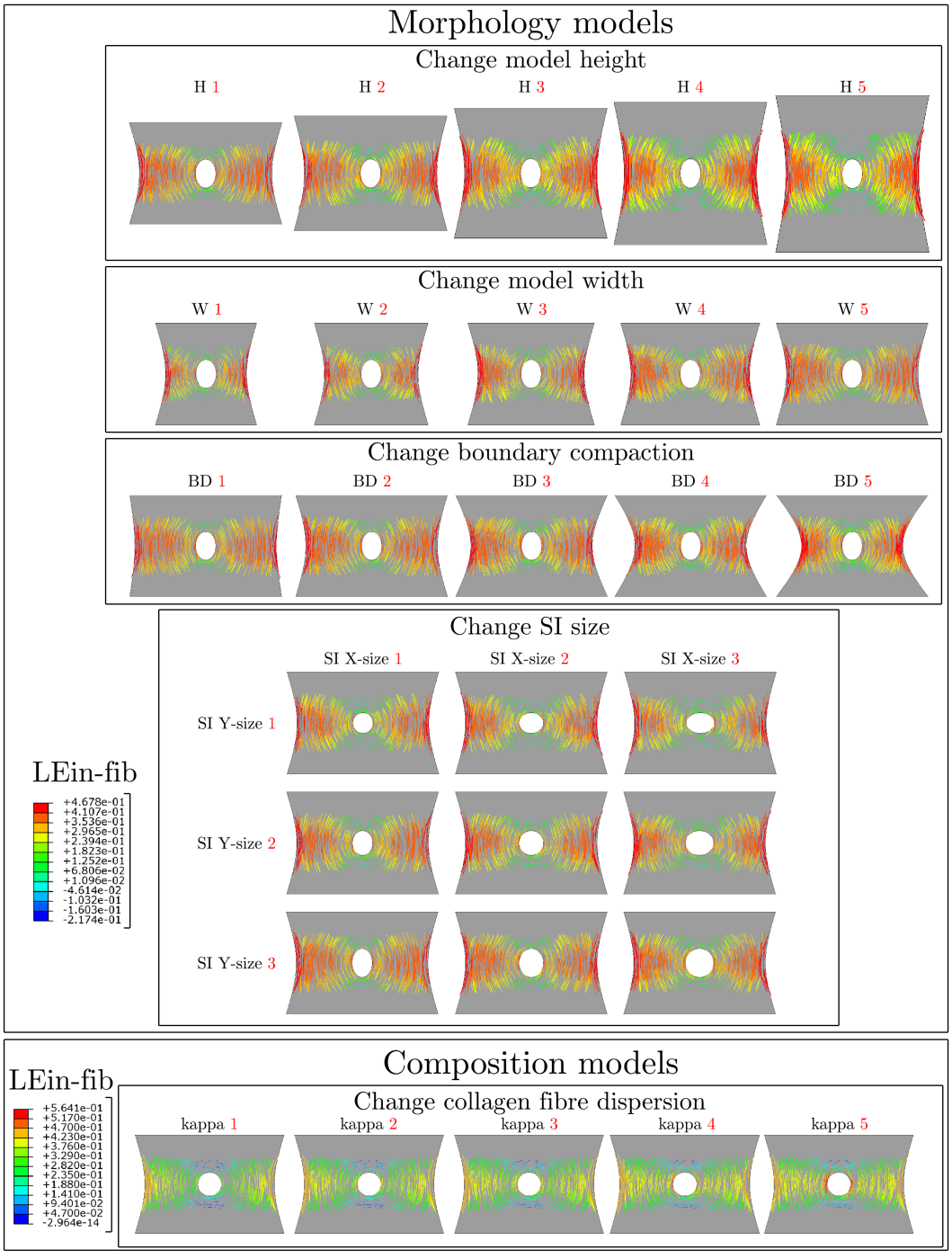

Figure 29: $LE_{\text{in-fib}}$ distributions for a selection of idealised morphology and composition models. The model parameter differing between the distributions is displayed above and/or next to its particular distribution (e.g. "W 1"). The model parameter values correspond linearly (from lowest to highest values assigned) with the parameter values as presented in Tables 1 and 2. Note that some distributions seem slightly asymmetrical. This is due to the fact that $LE_{\text{in-fib}}$ is shown for 70% of all elements of the model.

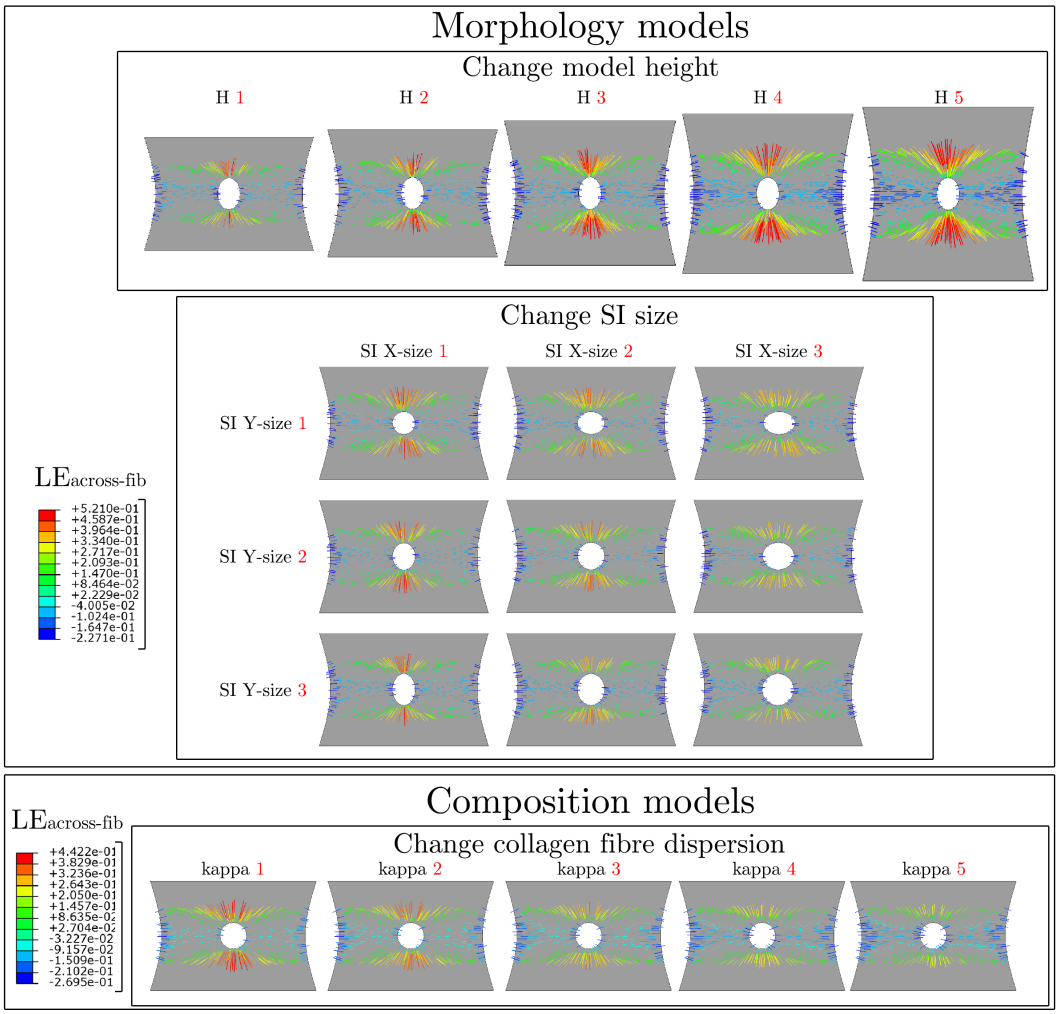

Figure 30: $LE_{\text{across-fib}}$ distributions for a selection of idealised morphology and composition models. The model parameter differing between the distributions is displayed above and/or next to its particular distribution (e.g. "H 1"). The model parameter values correspond linearly (from lowest to highest values assigned) with the parameter values as presented in Tables 1 and 2. Note that some distributions seem slightly asymmetrical. This is due to the fact that $LE_{\text{across-fib}}$ is shown for 70% of all elements of the model.

5 Discussion

The results of this study contribute to the current understanding of BE-FCs. As well as that it therefore aids research aiming to comprehend among other things the biomechanical behaviour of atherosclerotic plaque. All in all the first of such contributions is a modeling pipeline. Following the presented pipeline provides a BE-FC model with local-specific characteristics; a simulation therewith confers an approximation of the BE-FC its stresses and strains. On top of this many idealised BE-FC models were presented. These idealised models - which comprise a great number of possible BE-FC morphologies and compositions - allow for an in-depth interpretation of the aforementioned BE-FC models their stresses and strains.

As the results of the idealised models can be used to interpret the results of the BE-FC models, the upcoming discussion firstly provides a breakdown of the idealised models their simulation results. Further, the discussion on the BE-FC models will be a combination of a discussion on the presented results and a discussion on the developed modeling pipeline.

5.1 Idealised Models

This subsection is divided in three distinct parts. The stress and strain distributions of the idealised morphology models will be addressed first. This will provide a thorough understanding of the stresses and strains in relatively anisotropic models. This is followed by a discussion on the effects of geometrical changes in these models. Lastly, the same will be done for compositional changes in the idealised composition models.

Idealised morphology models - stress and strain distributions
The highest stresses in the idealised morphology models are S_y and $S_{\text{in-fib}}$. Moreover, they are very much alike. These results are within expectations. The models are stretched upwards and their load-bearing component is their collagenous matrix while the fibres therewithin can only bear a load in the fibre direction. In addition to this the assigned fibre mean angles Θ seem to dictate where the two stresses will be high or low. Indeed, areas with fibres predominantly in the loading direction experience high stresses. On the other hand, areas with mostly fibres perpendicular to the loading direction experience low stresses. These relations however do not explain all that is observed for S_y and $S_{\text{in-fib}}$. To start with, high stresses are concentrated to the middle of the compacted boundaries (even for slightly compacted models). This observation can be explained by considering two things: horizontal contraction of a model during stretching and large local differences in a model its stiffness. Model contraction is highest there where the model is most compliant perpendicular to the loading direction. This corresponds to model areas with a lot of fibres in the loading direction, which is around the middle of the compacted boundaries. This localized increase in strain around the middle of the compacted boundaries increases the stresses there. Further, the models have three extremely compliant areas; the SI and the two areas just outside the compacted boundaries between the corners of a model. As a model stretches these three areas expand effortlessly, reducing the strain in the loading direction in the areas above and underneath them. In other words, this reduces the stresses above and under the SI as well as at the corners of a model.

The LE_{xy} distribution of the idealised morphology models can be comprehended by considering the assigned fibre mean angles Θ and local differences in stiffness. Firstly, the four model areas close to the corners that border the clamps mostly have fibres that are oriented largely diagonal to the loading direction. As a consequence these areas strain relatively easily in shear, resulting in a high LE_{xy} there. Further, as was mentioned earlier, each model has three extremely compliant areas that reduce the strain in the loading direction above and under the SI as well as in the corners. This reduction in actual fact is gradual because these three extremely compliant areas are curved. As a result the idealised morphology models experience a high LE_{xy} diagonally around their SI as well as at their corners.

Model areas dominated by fibres more perpendicular to the loading direction strain more easily in the Y-direction. This corresponds with the observation that LE_y is high near the clamps. In consequence these high LE_y areas also allow a lower LE_y in the two areas between the SI and the compacted boundaries - areas dominated by fibres oriented more in the loading direction. Indeed, the higher the LE_y in the areas bordering the clamps, the lower the LE_y in the two areas between the SI and the compacted boundaries. Over and above, the high LE_y near the compacted boundaries could be a result of model contraction. As a final point, the actually observed diagonal straining pattern in the two areas bordering the clamps seems to be a result of the three extremely compliant model areas, which lower LE_y directly above and under the SI and at the corners of a model.

As could be expected the $LE_{\text{in-fib}}$ and $LE_{\text{across-fib}}$ distributions are counterparts of each other - there where $LE_{\text{in-fib}}$ is high, $LE_{\text{across-fib}}$ is low. These strains are highly dependent upon the assigned fibre mean angles Θ. Areas with a lot of fibres in the loading direction experience a high $LE_{\text{in-fib}}$ and a low $LE_{\text{across-fib}}$. Per contra, the opposite is the case in areas dominated by fibres that are oriented more perpendicular to the loading direction. What is more, $LE_{\text{in-fib}}$ is particularly high near the compacted boundaries. Again, this could be a result of model contraction.

Idealised morphology models - geometry changes
The relations between on the one hand model height or width and on the other hand the stresses and strains a model experiences can be explained using a single line of reasoning. A gain in either parameter enlarges particular model areas. In specific, a gain in height enlarges the model areas near the clamps. These areas have fibres predominantly perpendicular or diagonal to the loading direction. In other words, they are relatively compliant in the loading direction or in shear, respectively. In consequence a gain in model height increases LE_{xy}, LE_y, and $LE_{\text{across-fib}}$ in the areas near the clamps, and decreases $LE_{\text{in-fib}}$ there. Further, a gain in width enlarges the model areas between the SI and the compacted boundaries. These additional areas have mostly fibres in the loading direction near the clamps and are dominated by such fibres in the middle. In other words, these areas are relatively stiff in the loading direction throughout. A gain in model width therefore adds areas between the SI and the compacted boundaries with relatively high LE_y and $LE_{\text{in-fib}}$ everywhere.

A gain in model compaction increases the curve and the size of the two extremely compliant model areas outside the compacted boundaries between the corners of a model. As a consequence the corners of a model experience an increased LE_{xy}. The degree of compaction also affects the fibre mean angles Θ along the compacted boundaries. In specific, a gain

thereof clusters fibres that are in the loading direction to around the height of the SI. In contrast, a slightly compacted model has such fibres along its height. Consequently, a more compacted model contracts more around the height of its SI and less so at any other height. This localized increase in model contraction likely explains the increase of S_y, $S_{\text{in-fib}}$, and $LE_{\text{in-fib}}$ at the height of the SI near the compacted boundaries in more compacted models.

To apprehend the relations between on the one hand the shape and size of a model its SI and on the other hand the stresses and strains a model experiences, it is important to recognize that these SI characteristics affect a model its fibre mean angles Θ. In specific and except near a model its compacted boundaries, the assigned fibres follow the shape of the SI. A gain in size of the SI in the X-direction therefore increases the size of the model areas dominated by fibres more perpendicular or diagonal to the loading direction, i.e. these model areas become more compliant in the loading direction and/or in shear. In conjunction this increase in compliance also allows for more expansion of the SI, especially in the loading direction. As a result a gain in SI size in the X-direction decreases S_y and $S_{\text{in-fib}}$ around the SI. Furthermore, an increase in compliance in shear leads to an increase in LE_{xy} in the model areas diagonally around the SI. In like manner an increase in compliance in the loading direction and an increased expansion of the SI increases LE_y diagonally around the SI, and decreases it above and under the SI and between the SI and the compacted boundaries. Lastly, the change in fibre mean angles Θ and the increase in expansion of the SI also decreases $LE_{\text{in-fib}}$ and $LE_{\text{across-fib}}$ above and under the SI. A gain in the SI its size in the Y-direction per contra increases the size of the areas with mostly fibres in the loading direction. Accordingly, the stresses and strains in a model are affected opposite to what happens with a gain in SI size in the X-direction.

Idealised composition models - composition changes
Of all model parameters changed in the idealised models, the fibre dispersion κ is of principal interest. A change therein exceedingly affects all the stresses and strains examined. When a model is relatively anisotropic its biomechanical behaviour seems to be dictated mainly by the characteristics of its collagenous matrix. When a model is very isotropic - when the fibre dispersion κ is high - the collagenous matrix its dominant effect on a model its biomechanical behaviour is diminished. In such models the stress and strain distributions can be recognized as being contingent on model geometry. On account of that the stresses would be high at a geometrical irregularity there where the model its cross-section perpendicular to the loading direction is small. This is exactly what is observed - they are particularly high to the left and right of the SI. In addition to this another observation can be made for S_y and $S_{\text{in-fib}}$ in very isotropic models; the stresses brought forth by a model its geometrical features are much lower in magnitude. This particular observation seems to be brought about by a decrease in a model its stiffness with a gain in isotropy. Still further, this decrease in stiffness also augments the contraction of a model and the expansion of the three extremely compliant model areas (the SI and the two areas outside the compacted boundaries between a model its corners). Moreover, these observations together explain the strain distributions in increasingly isotropic models. Indeed then a more isotropic model should experience that what is observed: (1) an increase in LE_{xy} diagonally around the SI as well as at the corners, (2) an increase in LE_y and $LE_{\text{in-fib}}$ in the area between the SI and the compacted boundaries and especially so directly to the left and right of the SI, and lastly (3) a decrease of $LE_{\text{across-fib}}$ above and under the SI.

The last of all model parameters to be discussed are k_1 and k_2. The results show that a gain in k_1 and k_2 affects S_y and $S_{\text{in-fib}}$ - increasing them near the compacted boundaries. These results are as expected. Firstly, these locations already show high stresses for lower k_1 and k_2 values. Secondly, these parameters affect the stiffness of the model - k_1 is a stress-like material parameter and k_2 is a dimensionless material parameter. In consequence these locations should therefore experience an increase in stress with a gain in the value of these parameters.

5.2 Bio-Engineered Fibrous Cap Models & The Modeling Pipeline

Bio-engineered fibrous cap models - stress & strain distributions
The stress and strain distributions of the idealised models and the BE-FC models are globally very similar. In actual fact, the distributions of the BE-FC models are readily comprehensible having thoroughly considered those of the idealised models. To do so it can be concluded that multiple model behaviours and characteristics must be taken into account. This includes a model its: collagenous matrix characteristics, contraction, localized differences in stiffness, and its geometrical features. An extrapolation here of all these findings to that of a BE-FC model would be an exhaustive repetition of everything that has already been stated for the idealised models. However still - to provide a representative example - a discussion on the stress and strain distributions of BE-FC model number 3 is added to Appendix G.

Bio-engineered fibrous cap models - stress & strain peak values, and rupture
The highest stresses in the BE-FC models are S_y and $S_{\text{in-fib}}$. Moreover, their peak values are comparable within each BE-FC model. Between all BE-FC models S_y has a median of 3.151 [2.407, 3.896] MPa ([interquartile range]) and $S_{\text{in-fib}}$ has a median of 3.2555 [2.352, 4.159] MPa. These stresses are high when compared to the ultimate tensile strength observed in uni-axially tensile tested ex-vivo and unruptured human carotid FCs; Teng et al. [15] and Davis et al. [54] reported a ultimate tensile strength of 0.158 MPa [0.072, 0.259] and 0.366 [0.279, 0.648] MPa (median, [interquartile range]), respectively. Comparably, Holzapfel et al. [55] reported a ultimate tensile strength of 0.255 ± 0.0798 MPa (mean $\pm$ SD) in ex-vivo uni-axially tensile tested FCs of iliac plaques. The peak stresses in FC sections in finite element models of plaques are likewise considerably lower than the peak stresses obtained in this study; Li et al. [56] reported a peak stress of 0.683 MPa and 0.227 MPa in models of ruptured and unruptured carotid plaques, respectively. Still further and in similar conflicting manner the peak stresses in the BE-FC models could not be co-localized to the rupture initiation locations observed in the BE-FCs, while the literature provides proof that FC rupture in actual plaques is preceded by high structural stresses [16, 17, 20, 38, 57, 58].

There are several explanations for the aforementioned dissimilarities. Firstly, the BE-FCs could be less prone to rupture than real human FCs, leading them to rupture at higher stresses. Indeed, one such indication is that human ex-vivo uni-axially tensile tested FCs rupture at lower strains. For instance, Teng et al. [15] reported an ultimate strain of 1.18 [1.10, 1.27] (median, [interquartile range]) for carotid FCs and Holzapfel et al. [55] reported similar values of 1.182 ± 0.1 (mean, SD) for iliac FCs. Per contra, the peak values of the highest strains in the BE-FC models at rupture were much higher. In addition the actually observed BE-FC rupture initiation could transpire through a yet unidentified damage mechanism; BE-FCs can be regarded as fibre-reinforced soft tissues which are known to exhibit distinctive damage mechanisms. More specifically, these mechanisms include a division of

matrix failure and fibre failure [59–61]; a fibre-reinforced soft tissue its matrix and fibres can fail in both tension as well as compression, and damage can also ensue due to shear between the fibres and the matrix, which is termed delamination. These damage mechanisms are not necessarily represented in the peak stresses and strains in the models, or their locations. Matrix failure for instance could occur at lower stresses and/or strains. Presently it is unclear through which mechanism the BE-FCs develop damage that leads to rupture. Along with the aforementioned, assumptions were made in the modeling pipeline which affect the stress and strain peak values and their locations. These assumptions are addressed later on.

Bio-engineered fibrous cap models - global behaviour
The global biomechanical behaviour of the BE-FCs is satisfyingly approximated by the models. However still differences were observed. Firstly, the model relationship overestimates the experimental in the low strain regime. Here the experimental relationship resembles what is termed a "toe region" - a phenomenon transpiring from unloaded collagen fibres realigning and stretching easily without much force [62]. This behaviour is not defined in the models. Different methods to do so in a soft biological tissue have been presented in the literature (e.g., see [63]). For higher amounts of strain there is a consequent underestimation and overestimation of the force. This in all probability arises from the inability to fit the toe-region or from (micro)damage accumulating in the BE-FC, or from a combination thereof. The latter stated behaviour is not incorporated in the models. To do so one could e.g. use a material model formulation such as presented by Gasser [63], which consists of a decomposed material deformation formulation that contains an elastic and a plastic constituent.

Bio-engineered fibrous cap models - modeling pipeline assumptions & choices
Following the presented pipeline provides 2D models. The BE-FCs however exhibit a variable thickness and a changing composition in the in-thickness direction (increasingly isotropic farther within the tissue). These characteristics may significantly affect the BE-FCs their biomechanical behaviour (including their rupture characteristics) and could necessitate the use of 3D models. As per example, a high stress and/or strain gradient may well ensue from a sharp isotropy increase in a BE-FC in the in-thickness direction. In consequence, this high gradient could cause damage within a BE-FC, possibly even in the low strain regime. Having said that, constructing 3D BE-FC models requires new methods or adjustment of the methods in the provided pipeline. To give an instance of the latter, a geometry could be constructed by using a combination of the already adopted planar geometry images in combination with for example in-thickness echo data. On top of that a composition could be established by: employing the HGO material model, utilizing numerous in-thickness stacked collagen images, determining the material parameters with the presented methods, assigning the parameters to a model geometry using the location of the collagen images, and e.g. smoothing the assigned parameters between said locations with a smoothing operation.

BE-FC collagen imaging was limited to two whole-width grid strips. Moreover, the fibre dispersion κ and mean angle Θ were determined therefrom. Consequently two assumptions were necessary to define them over the whole of the BE-FC models. The fibre dispersion κ was spread out over each BE-FC model and the fibre mean angle Θ was assumed to either follow the shape of a model its SI or its compacted boundaries. As the presented results show that the fibre dispersion κ and mean angle Θ considerably affect the biomechanical

behaviour of the BE-FC models, improving these collagen-related parameters their accuracy should be a principal interest of future modeling studies. Availability of collagen images over the whole of the BE-FCs would omit the two assumptions and is therefore recommended for such studies. Supplementary to this the collagen images could be sectioned and a κ and Θ could be determined for each such section, resulting in a higher resolution of the two collagen-related parameters.

On a related note to the aforementioned, the presented method to determine the fibre dispersion κ and mean angle Θ from a collagen image can only extract a single of each parameter per said image. This allows the modeling of only a single fibre family per image, while - in some cases - the data showed multiple families. The source of this limitation is the unimodal transversely isotropic VM distribution that is fitted to the fibre orientation distribution of a collagen image. This specific VM distribution is defined by only a single fibre dispersion κ and mean angle Θ. To obtain multiple such parameters one must change the to-be-fitted statistical distribution to e.g., a bi-variate transversely isotropic VM distribution. Be that as it may, available literature was explored to no avail. Future studies could aim to develop a method for determining multiple κ and Θ per image.

A BE-FC model its composition is further defined by the material parameters C_{10}, k_1, and k_2. These were specified as locally in-variant. Model simulation results however could benefit from these parameters being locally variant. C_{10}, k_1, and k_2 were determined with a method alike to inverse finite element modeling. In particular, they were obtained by optimizing the model its force-length relationship to the experimentally obtained one. To obtain locally variant parameters this framework has to be altered. Firstly, the parameters must be optimized using locally variant experimental data. In this regard e.g. BE-FC strains as determined by digital image correlation could be used. Further, making the parameters locally variant leads to a lot of to-be-optimized parameters. In other words, the parameter space to be explored during the optimization significantly increases. This particular problem can be alleviated by making the parameters semi-locally variant; they could be determined for e.g. clusters of elements rather than for instance per element.

The final point of discussion is on the modeling approach of the BE-FCs their SI. Some of the BE-FCs their actual SI is a hole and accordingly the approach to model it as such is assumed to be appropriate. However, a proportion had their SI filled with fibrin during the culturing process and these SIs exhibit a thin layer of fibres which integrate with the rest of the BE-FC. In consequence, the models of these BE-FCs may perhaps benefit from another modeling approach such as regarding them as a filled region and assigning a HGO material formulation.

6 Conclusion

With this study, a novel modeling pipeline has been developed which when followed through with provides 2D finite element models of BE-FCs. Among other things it includes three especially noteworthy and self-developed scripts. The first provides a model geometry in a data-scaleable manner by utilizing the pixel brightness in geometry images. Further, the second contributes the stress-like HGO material model parameters using a method alike to inverse finite element modeling. Lastly, the remaining HGO material model parameters - the

collagen fibre dispersion κ and mean angle Θ - are obtained from collagen images using an optimization scheme that fits a unimodal π-periodic transversely isotropic VM distribution onto collagen fibre orientation data. Results from simulations with these BE-FC models give insight into the biomechanical behaviour of BE-FCs. Over and above this idealised BE-FC models have been created which allow a more thorough investigation of the relations between on the one hand a BE-FC its morphology and composition, and on the other hand its biomechanical behaviour.

Analysis of the simulation results included an investigation in terms of the global biomechanical behaviour as well as the stress and strain peak values, peak value locations, and distributions. The experimentally obtained global biomechanical behaviour of the BE-FCs is satisfyingly approximated by that of their respective model. The peak stresses and strains in the BE-FC models are considerably higher than those observed in uni-axially tensile tested FCs, as well as in FC sections of finite element models. In like manner, the locations of the peak stresses and strains in the BE-FC models could not be co-localized to the rupture initiation locations of the BE-FCs. Lastly, the stress and strain distributions are thoroughly investigated and each is contingent on different model characteristics and/or behaviours. In general however the most crucial of these are the collagen fibre dispersion κ, the collagen fibre mean angle Θ, the degree of model compaction, and the SI its shape and size.

To conclude, future research could set out to: construct 3D BE-FC models, create models with collagen-related data that is available throughout the BE-FCs, compose programs that determine multiple HGO material model collagen-related parameters per collagen image, or even expand on the presented parametric study by e.g. looking into the relation between a BE-FC its asymmetry and its biomechanical behaviour. Certainly, there are sufficient outstanding research possibilities.

7 References

[1] I. Ferreira-González, "The epidemiology of coronary heart disease," *Revista Española de Cardiología (English Edition)*, vol. 67, no. 2, pp. 139–144, 2014.

[2] H. A. Wafa, C. D. Wolfe, E. Emmett, G. A. Roth, C. O. Johnson, and Y. Wang, "Burden of stroke in europe: Thirty-year projections of incidence, prevalence, deaths, and disability-adjusted life years," *Stroke*, vol. 51, no. 8, pp. 2418–2427, 2020.

[3] D. Mozaffarian *et al.*, "Heart disease and stroke statistics—2015 update: A report from the american heart association," *Circulation*, vol. 131, no. 4, e29–e322, 2015.

[4] K. Sakakura, M. Nakano, F. Otsuka, E. Ladich, F. D. Kolodgie, and R. Virmani, "Pathophysiology of atherosclerosis plaque progression," *Heart, Lung and Circulation*, vol. 22, no. 6, pp. 399–411, 2013.

[5] A. Akyildiz, "Biomechanical modeling of atherosclerotic plaques for risk assessment," 2013.

[6] W. Insull Jr, "The pathology of atherosclerosis: Plaque development and plaque responses to medical treatment," *The American journal of medicine*, vol. 122, no. 1, S3–S14, 2009.

[7] U. Sadat, Z. Teng, and J. H. Gillard, "Biomechanical structural stresses of atherosclerotic plaques," *Expert review of cardiovascular therapy*, vol. 8, no. 10, pp. 1469–1481, 2010.

[8] S. Williamson, Y Lam, H. Younis, H Huang, S Patel, R. Kamm, *et al.*, "On the sensitivity of wall stresses in diseased arteries to variable material properties," *Journal of biomechanical engineering*, vol. 125, no. 1, pp. 147–155, 2003.

[9] G. Finet, J. Ohayon, and G. Rioufol, "Biomechanical interaction between cap thickness, lipid core composition and blood pressure in vulnerable coronary plaque: Impact on stability or instability," *Coronary artery disease*, vol. 15, no. 1, pp. 13–20, 2004.

[10] J. Ohayon, P. Teppaz, G. Finet, and G. Rioufol, "In-vivo prediction of human coronary plaque rupture location using intravascular ultrasound and the finite element method," *Coronary artery disease*, vol. 12, no. 8, pp. 655–663, 2001.

[11] A. Akyildiz *et al.*, "Effects of intima stiffness and plaque morphology on peak cap stress," *Biomedical engineering online*, vol. 10, no. 1, pp. 1–13, 2011.

[12] J. F. Bentzon, F. Otsuka, R. Virmani, and E. Falk, "Mechanisms of plaque formation and rupture," *Circulation research*, vol. 114, no. 12, pp. 1852–1866, 2014.

[13] A. V. Finn, M. Nakano, J. Narula, F. D. Kolodgie, and R. Virmani, "Concept of vulnerable/unstable plaque," *Arteriosclerosis, thrombosis, and vascular biology*, vol. 30, no. 7, pp. 1282–1292, 2010.

[14] D. Tang *et al.*, "Sites of rupture in human atherosclerotic carotid plaques are associated with high structural stresses: An in vivo mri-based 3d fluid-structure interaction study," *Stroke*, vol. 40, no. 10, pp. 3258–3263, 2009.

[15] Z. Teng *et al.*, "A uni-extension study on the ultimate material strength and extreme extensibility of atherosclerotic tissue in human carotid plaques," *Journal of biomechanics*, vol. 48, no. 14, pp. 3859–3867, 2015.

[16] M. Li, J. Beech-Brandt, L. John, P. Hoskins, and W. Easson, "Numerical analysis of pulsatile blood flow and vessel wall mechanics in different degrees of stenoses," *Journal of biomechanics*, vol. 40, no. 16, pp. 3715–3724, 2007.

[17] Z.-Y. Li *et al.*, "Stress analysis of carotid plaque rupture based on in vivo high resolution mri," *Journal of biomechanics*, vol. 39, no. 14, pp. 2611–2622, 2006.

[18] M Cilla, E Peña, and M. Martínez, "3d computational parametric analysis of eccentric atheroma plaque: Influence of axial and circumferential residual stresses," *Biomechanics and modeling in mechanobiology*, vol. 11, no. 7, pp. 1001–1013, 2012.

[19] H. C. Groen *et al.*, "Plaque rupture in the carotid artery is localized at the high shear stress region: A case report," *Stroke*, vol. 38, no. 8, pp. 2379–2381, 2007.

[20] Z. Teng *et al.*, "3d critical plaque wall stress is a better predictor of carotid plaque rupture sites than flow shear stress: An in vivo mri-based 3d fsi study," 2010.

[21] I.-K. Jang *et al.*, "In vivo characterization of coronary atherosclerotic plaque by use of optical coherence tomography," *Circulation*, vol. 111, no. 12, pp. 1551–1555, 2005.

[22] H. M. Loree, R. D. Kamm, R. G. Stringfellow, and R. T. Lee, "Effects of fibrous cap thickness on peak circumferential stress in model atherosclerotic vessels," *Circulation research*, vol. 71, no. 4, pp. 850–858, 1992.

[23] Z. Teng *et al.*, "Lumen irregularity dominates the relationship between mechanical stress condition, fibrous-cap thickness, and lumen curvature in carotid atherosclerotic plaque," 2011.

[24] Z. Teng *et al.*, "Arterial luminal curvature and fibrous-cap thickness affect critical stress conditions within atherosclerotic plaque: An in vivo mri-based 2d finite-element study," *Annals of Biomedical Engineering*, vol. 38, no. 10, pp. 3096–3101, 2010.

[25] P. D. Richardson, M. Davies, and G. Born, "Influence of plaque configuration and stress distribution on fissuring of coronary atherosclerotic plaques," *The Lancet*, vol. 334, no. 8669, pp. 941–944, 1989.

[26] A. P. Burke, A. Farb, G. T. Malcom, Y.-h. Liang, J. E. Smialek, and R. Virmani, "Plaque rupture and sudden death related to exertion in men with coronary artery disease," *Jama*, vol. 281, no. 10, pp. 921–926, 1999.

[27] L. O. Jensen *et al.*, "Intravascular ultrasound assessment of fibrous cap remnants after coronary plaque rupture," *American heart journal*, vol. 152, no. 2, pp. 327–332, 2006.

[28] A. Maehara *et al.*, "Morphologic and angiographic features of coronary plaque rupture detected by intravascular ultrasound," *Journal of the American College of Cardiology*, vol. 40, no. 5, pp. 904–910, 2002.

[29] R. Virmani, F. D. Kolodgie, A. P. Burke, A. Farb, and S. M. Schwartz, "Lessons from sudden coronary death: A comprehensive morphological classification scheme for atherosclerotic lesions," *Arteriosclerosis, thrombosis, and vascular biology*, vol. 20, no. 5, pp. 1262–1275, 2000.

[30] G. R. Douglas, A. J. Brown, J. H. Gillard, M. R. Bennett, M. P. Sutcliffe, and Z. Teng, "Impact of fiber structure on the material stability and rupture mechanisms of coronary atherosclerotic plaques," *Annals of biomedical engineering*, vol. 45, no. 6, pp. 1462–1474, 2017.

[31] H. E. Barrett, K. Van der Heiden, E. Farrell, F. J. Gijsen, and A. C. Akyildiz, "Calcifications in atherosclerotic plaques and impact on plaque biomechanics," *Journal of biomechanics*, vol. 87, pp. 1–12, 2019.

[32] P. Fratzl, "Collagen: Structure and mechanics, an introduction," in *Collagen*, Springer, 2008, pp. 1–13.

[33] G. A. Holzapfel, T. C. Gasser, and M. Stadler, "A structural model for the viscoelastic behavior of arterial walls: Continuum formulation and finite element analysis," *European Journal of Mechanics-A/Solids*, vol. 21, no. 3, pp. 441–463, 2002.

[34] G. A. Holzapfel, "Collagen in arterial walls: Biomechanical aspects," in *Collagen*, Springer, 2008, pp. 285–324.

[35] A. Balguid *et al.*, "The role of collagen cross-links in biomechanical behavior of human aortic heart valve leaflets—relevance for tissue engineering," *Tissue engineering*, vol. 13, no. 7, pp. 1501–1511, 2007.

[36] A. C. Akyildiz *et al.*, "3d fiber orientation in atherosclerotic carotid plaques," *Journal of Structural Biology*, vol. 200, no. 1, pp. 28–35, 2017.

[37] M. D. Rekhter, "Collagen synthesis in atherosclerosis: Too much and not enough," *Cardiovascular research*, vol. 41, no. 2, pp. 376–384, 1999.

[38] G. C. Cheng, H. M. Loree, R. D. Kamm, M. C. Fishbein, and R. T. Lee, "Distribution of circumferential stress in ruptured and stable atherosclerotic lesions. a structural analysis with histopathological correlation," *Circulation*, vol. 87, no. 4, pp. 1179–1187, 1993.

[39] N. Kassis *et al.*, "Fibrous cap thickness predicts stable coronary plaque progression: Early clinical validation of a semiautomated oct technology," *Journal of the Society for Cardiovascular Angiography & Interventions*, vol. 1, no. 5, p. 100 400, 2022.

[40] X. Liu *et al.*, "New insights into fibrous cap thickness of vulnerable plaques assessed by optical coherence tomography," *BMC Cardiovascular Disorders*, vol. 22, no. 1, pp. 1–8, 2022.

[41] P. Wang, Z. Chen, and D. Xing, "Multi-parameter characterization of atherosclerotic plaques based on optical coherence tomography, photoacoustic and viscoelasticity imaging," *Optics Express*, vol. 28, no. 9, pp. 13 761–13 774, 2020.

[42] T. Wissing, K Van der Heiden, S. Serra, A. Smits, C. Bouten, and F. Gijsen, "Tissue-engineered collagenous fibrous cap models to systematically elucidate atherosclerotic plaque rupture," *Scientific reports*, vol. 12, no. 1, pp. 1–13, 2022.

[43] M. Smith, *ABAQUS/Standard User's Manual, Version 17.08.51*, English. United States: Dassault Systèmes Simulia Corp, 2020.

[44] D. Engwirda, "Locally-optimal delaunay-refinement and optimisation-based mesh generation," Ph.D. dissertation, The University of Sydney, 2014.

[45] *Reduced integration*, Available at: https://abaqus-docs.mit.edu/2017/English/SIMACAEGSARefMap/simagsa-c-ctmreduced.htm, Accessed: 02-08-2022.

[46] *What is the difference between the medial axis algorithm and the advancing front algorithm?,* Available at: https://classes.engineering.wustl.edu/2009/spring/mase5513/abaqus/docs/v6.6/books/usi/default.htm?startat=pt03ch17s07s06.html, Accessed: 02-08-2022.

[47] *What is a mesh transition?,* Available at: https://classes.engineering.wustl.edu/2009/spring/mase5513/abaqus/docs/v6.6/books/usi/default.htm?startat=pt03ch17s07s06.html, Accessed: 02-08-2022.

[48] G. A. Holzapfel, T. C. Gasser, and R. W. Ogden, "A new constitutive framework for arterial wall mechanics and a comparative study of material models," *Journal of elasticity and the physical science of solids*, vol. 61, no. 1, pp. 1–48, 2000.

[49] *Anisotropic hyperelastic material behavior*, Available at: http://130.149.89.49:2080/v6.8/books/stm/default.htm?startat=ch04s06ath125.html, Accessed: 02-08-2022.

[50] MATLAB, *version 9.8.0.1451342 (R2020a)*. Natick, Massachusetts: The MathWorks Inc., 2020.

[51] S. Mariën, *Fiblab*, 2006. [Online]. Available: https://gitlab.tue.nl/stem/FibLab.

[52] T. C. Gasser, R. W. Ogden, and G. A. Holzapfel, "Hyperelastic modelling of arterial layers with distributed collagen fibre orientations," *Journal of the royal society interface*, vol. 3, no. 6, pp. 15–35, 2006.

[53] *How pattern search polling works*, Available at: https://nl.mathworks.com/help/gads/how-pattern-search-polling-works.html, Accessed: 02-08-2022.

[54] L. A. Davis, S. E. Stewart, C. G. Carsten III, B. A. Snyder, M. A. Sutton, and S. M. Lessner, "Characterization of fracture behavior of human atherosclerotic fibrous caps using a miniature single edge notched tensile test," *Acta biomaterialia*, vol. 43, pp. 101–111, 2016.

[55] G. A. Holzapfel, G. Sommer, and P. Regitnig, "Anisotropic mechanical properties of tissue components in human atherosclerotic plaques," *J. Biomech. Eng.*, vol. 126, no. 5, pp. 657–665, 2004.

[56] Z.-Y. Li *et al.*, "Stress analysis of carotid plaque rupture based on in vivo high resolution mri," *Journal of biomechanics*, vol. 39, no. 14, pp. 2611–2622, 2006.

[57] Z.-Y. Li *et al.*, "Structural analysis and magnetic resonance imaging predict plaque vulnerability: A study comparing symptomatic and asymptomatic individuals," *Journal of Vascular Surgery*, vol. 45, no. 4, pp. 768–775, 2007.

[58] C. Costopoulos *et al.*, "Plaque rupture in coronary atherosclerosis is associated with increased plaque structural stress," *JACC: Cardiovascular Imaging*, vol. 10, no. 12, pp. 1472–1483, 2017.

[59] Q. Yangyang and B. Yuanli, "A review on failure modeling methods of fiber reinforced polymer matrix composites," *Journal of Automotive Safety and Energy*, vol. 9, no. 01, p. 1, 2018.

[60] A. C. Orifici, I. Herszberg, and R. S. Thomson, "Review of methodologies for composite material modelling incorporating failure," *Composite structures*, vol. 86, no. 1-3, pp. 194–210, 2008.

[61] E. Carrera, "Implementation of classical and advanced failure criteria for composite layered structures in femap and assessment of results," Ph.D. dissertation, POLITECNICO DI TORINO, 2018.

[62] S. C. Cowin and S. B. Doty, *Tissue mechanics*. Springer, 2007.

[63] T. C. Gasser, "An irreversible constitutive model for fibrous soft biological tissue: A 3-d microfiber approach with demonstrative application to abdominal aortic aneurysms," *Acta Biomaterialia*, vol. 7, no. 6, pp. 2457–2466, 2011.

8 Appendix A - Bio-engineered Fibrous Caps - Specifics

Bio-Engineered Fibrous Caps - Straining Protocols
The straining protocols for bringing about compositional and geometrical changes in the myofibroblast-seeded fibrin-based gels are presented in the following list and Fig. 31 (as partially adopted from [42]). In particular, each gel was subjected to one of three straining protocols for a period of seven days by placing them on a post in the Flexcell FC-4000T (Flexcell Int, McKeesport, Pa). This Flexcell creates a vacuum chamber, straining the gel by a specified amount.

- **Static straining** (S-strain): a no-strain protocol. No strain is applied at all to achieve a high degree of isotropy (high collagen fibre dispersion).
- **Intermittent straining** (I-strain): an intermittent straining protocol. A strain of 4% is applied for 1 hour at 0.5 Hz followed by 3 hours of 0% strain. The I-strain protocol is aimed at creating anisotropic BE-FCs (low collagen fibre dispersion) by inducing fibre remodeling and synthesis.
- **Continuous straining** (C-strain): a continuous straining protocol. A strain of 4 % at 0.5 Hz is applied for the whole straining period. The C-strain protocol is intended to create anisotropic BE-FCs with cross-linked collagen fibres through the balancing of fibre remodeling and the maturation of fibres (because of less "late-stage" fibre synthesis and remodeling as compared to the I-strain protocol).

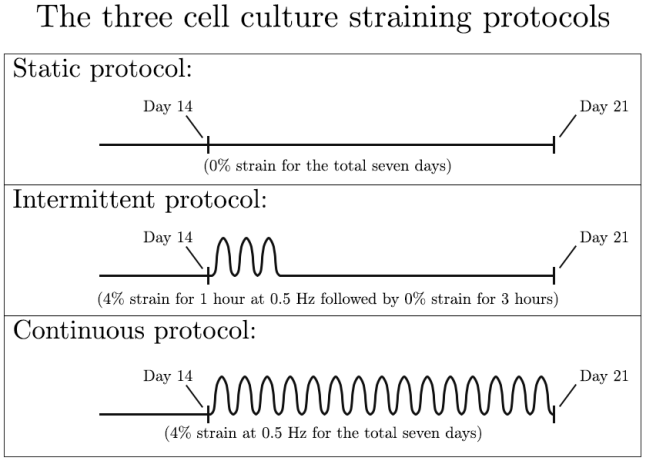

Figure 31: The static, intermittent, and continuous straining protocols applied to the gels.

Bio-engineered Fibrous Caps - The Specifics For Each
The exact experimental procedure followed for each BE-FC is delineated in Table 5. Moreover, the BE-FCs subjected to C-strain were loaded by using a 4.5 N load cell whereas for the others a 10 N stepping motor load cell was used. At the end digital imaging was performed at either 25 fps (sample 1), 30 fps (samples 2-11), or 120 fps (sample 13-17).

Table 5: An overview of the exact experimental procedure followed for each BE-FC. This includes: the BE-FC sample number, the initial planar geometry shape including the dimensions (width x length, [mm]) and the SI type, the straining protocol, the distance between the clamps when the BE-FC is placed in the tensile tester, the pre-stretch characteristics, the details of the pre-conditioning, and the specifics of the tensile test itself.

#	Shape, size (w x h), SI type	Protocol	Unclamped distance	Pre-stretch	Pre-conditioning	Tensile test
1-2	Rectangular, 15 x 10 mm, fibrin SI	C-strain	5.02 mm	1 stretch, 0.02 mm/s	10 cycles, 0.17 mm/s until 0.5 mm	1 stretch, 0.02 mm/s
3-11	Rectangular, 15 x 10 mm, fibrin SI	I-strain	5.02 mm	1 stretch, 0.02 mm/s	10 cycles, 0.17 mm/s until 0.5 mm	1 stretch, 0.02 mm/s
12	Rectangular, 15 x 10 mm, empty SI	S-strain	4.92 mm	1 stretch, 0.02 mm/s	10 cycles, 0.17 mm/s until 0.5 mm	1 stretch, 0.02 mm/s
13	Rectangular, 15 x 10 mm, fibrin SI	S-strain	4.92 mm	1 stretch, 0.02 mm/s	10 cycles, 0.17 mm/s until 0.5 mm	1 stretch, 0.17 mm/s
14	Rectangular, 15 x 10 mm, fibrin SI	S-strain	4.92 mm	1 stretch, 0.02 mm/s	10 cycles, 0.17 mm/s until 0.5 mm	1 stretch, 0.17 mm/s
15	Rectangular, 15 x 10 mm, empty SI	S-strain	4.92 mm	1 stretch, 0.02 mm/s	10 cycles, 0.17 mm/s until 0.5 mm	1 stretch, 0.17 mm/s
16	Dogbone, 10 x 15 mm, fibrin SI	S-strain	7.50 mm	1 stretch, 0.05 mm/s	10 cycles, 0.26 mm/s until 0.75 mm	1 stretch, 0.026 mm/s

9 Appendix B - Bio-engineered Fibrous Cap Models - Characteristics

Bio-engineered Fibrous Caps - Geometry & Composition
Fig. 32 presents the cropped geometry images of the BE-FCs. It is of note that there were large differences in the final geometry between a number of FCs. Firstly, the geometries differ in size in both the X-direction as well as the Y-direction. Secondly, the BE-FC can be asymmetric. This is especially noticeable in samples 1, 2, 5, 7, 8, 10, 11, 12, and 13. Moreover, the compacted boundaries can be seen to have bulges and indentations for samples 1, 4, 7, 8, 9, 11, 12, and 13.

Fig. 32 also shows the grid tiles where collagen is imaged. The color of a tile indicates the degree of collagen fibre dispersion κ. The direction of the vector within a grid tile indicates the collagen fibre mean angle Θ. Several observations can be made regarding κ and Θ. Firstly, Overall lower values for κ are found for BE-FCs 1 and 2. This is followed by slightly higher κ values for κ for BE-FCs 3 through 10. BE-FCs 11-17 show the overall highest values for κ. Secondly, For BE-FCs 1 through 10 the overall lower value for κ is concentrated near the BE-FC its compacted boundaries. In addition κ is higher everywhere else. Lastly, near

the compacted boundaries of the BE-FC, Θ follows said boundaries. Everywhere else on the BE-FC its geometry - for many of the BE-FCs (samples 1, 2, 4, 7, 9, 10, 11, 12, 13, 14, and 15) - Θ seems to roughly follow the shape of the BE-FC its SI. For the BE-FCs where this is not the case (samples 3, 5, 6, 8, and 16) Θ seems to be a combination of following the BE-FC its SI and a vertical alignment.

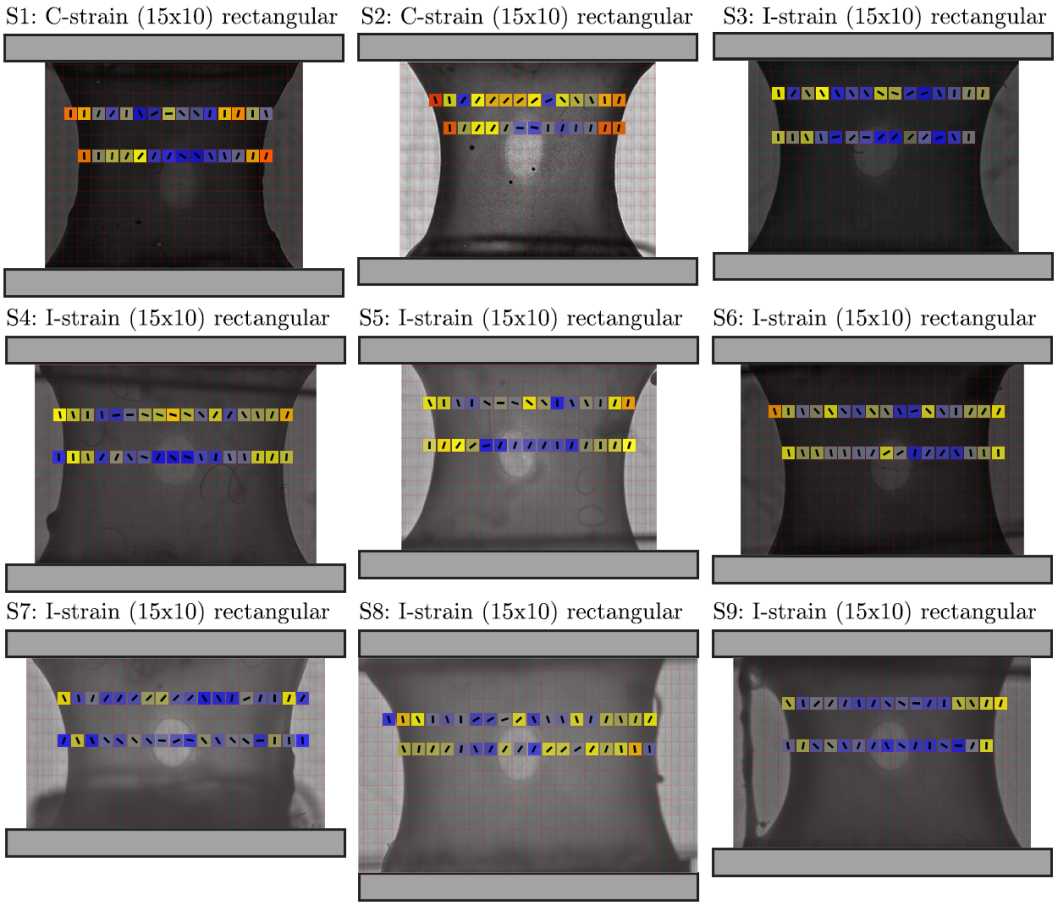

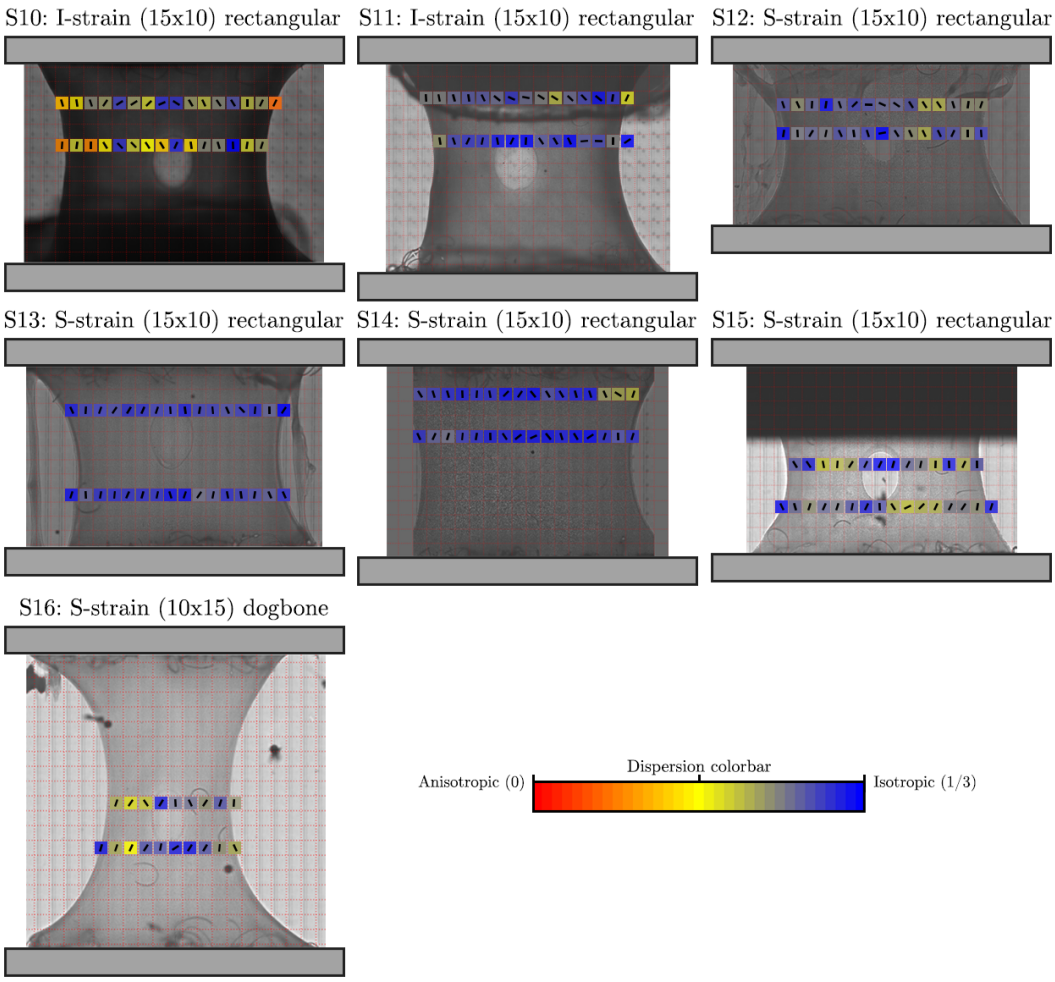

Figure 32: The geometry images of the BE-FCs. The collagen fibre dispersion κ and the collagen fibre mean angle Θ are shown for the tiles where collagen is imaged. The color of a tile represents the degree of collagen fibre dispersion κ. The direction of the vector within the tile indicates the collagen fibre mean angle Θ.

Bio-engineered Fibrous Cap Models - Geometry

Fig. 33 presents the BE-FC models their geometries. Of note to mention here is that some models are flipped or rotated around their midpoint (relative to the depiction in Fig. 32) to replicate the placement of the BE-FCs in the tensile tester. The light grey areas represent the non-fixed areas of the BE-FCs in the tensile tester. The darkgrey areas show where the BE-FCs are fixed in the tensile tester.

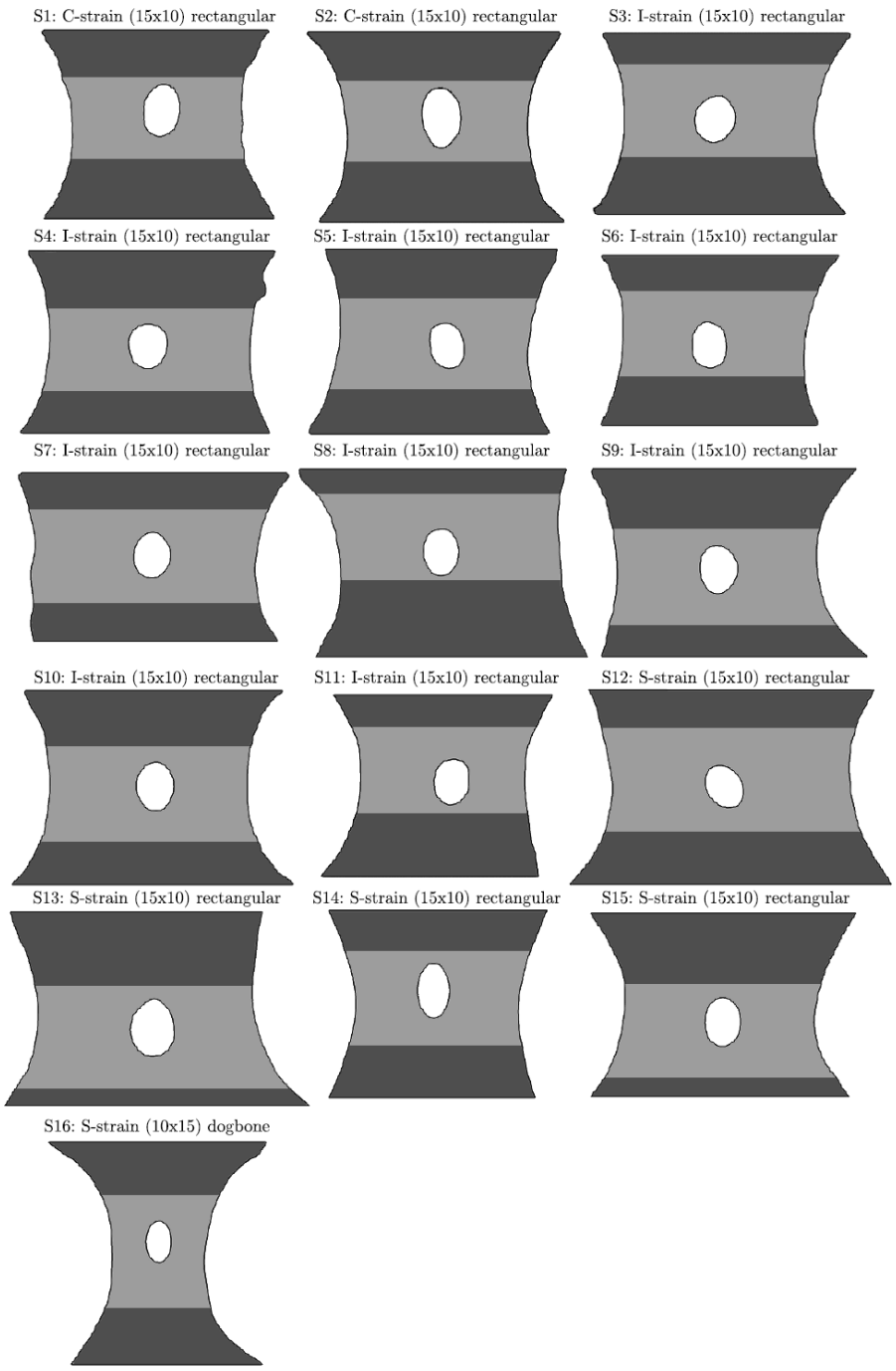

Figure 33: The geometries of the BE-FC models. Dark grey areas: the BE-FC regions fixed between the clamps of the tensile tester. Dark grey areas: the non-fixed BE-FC regions.

Bio-engineered Fibrous Caps - Material Model
The values of the HGO material model parameters D, C_{10}, k_1, and k_2 as assigned to the BE-FC models are shown in Table. 6. Apart from D these parameter values are found with a method alike to inverse finite element modeling (as discussed in section). On account of that the experimental and model force-length relationships are presented in Fig. 34.

The collagen fibre dispersion κ as assigned to the BE-FC models is shown in Fig. 35. As expected from the assumptions made to assign κ, clear vertical κ spread patterns can be noticed. In addition a smooth gradient in κ between elements can be observed as well.

Fig. 36 shows the collagen fibre mean angle Θ as assigned to the BE-FC models (for 70% of all elements). Due to assumptions made to assign Θ over the whole of each BE-FC model two clear orientation patterns can be noticed. Near the compacted model boundaries Θ follows said boundaries and everywhere else on the model Θ follows the shape of the SI. Lastly, a moderate smoothing can be seen between two clear Θ patterns.

Table 6: An overview of the HGO material model parameter values (D, C_{10}, k_1, and k_2) as assigned to each BE-FC model.

#	D	C_{10}	k_1	k_2
1	0.001	0.0673	0.3594	1.9438
2	0.001	0.0422	0.2500	0.8500
3	0.001	0.2023	2.7500	1.8500
4	0.001	0.0969	2.0000	3.1000
5	0.001	0.1691	3.2500	0.1000
6	0.001	0.1672	2.0000	2.1000
7	0.001	0.0813	1.1250	2.3500
8	0.001	0.1750	0.7187	0.1000
9	0.001	0.0969	1.2500	1.3500
10	0.001	0.0998	1.0000	1.6000
11	0.001	0.1360	1.5000	2.1000
12	0.001	0.0656	4.6875	0.0375
13	0.001	0.2922	5.3750	0.1000
14	0.001	0.3527	7.8125	0.1000
15	0.001	0.1164	3.7500	0.1000
16	0.001	0.2805	5.2500	1.7250

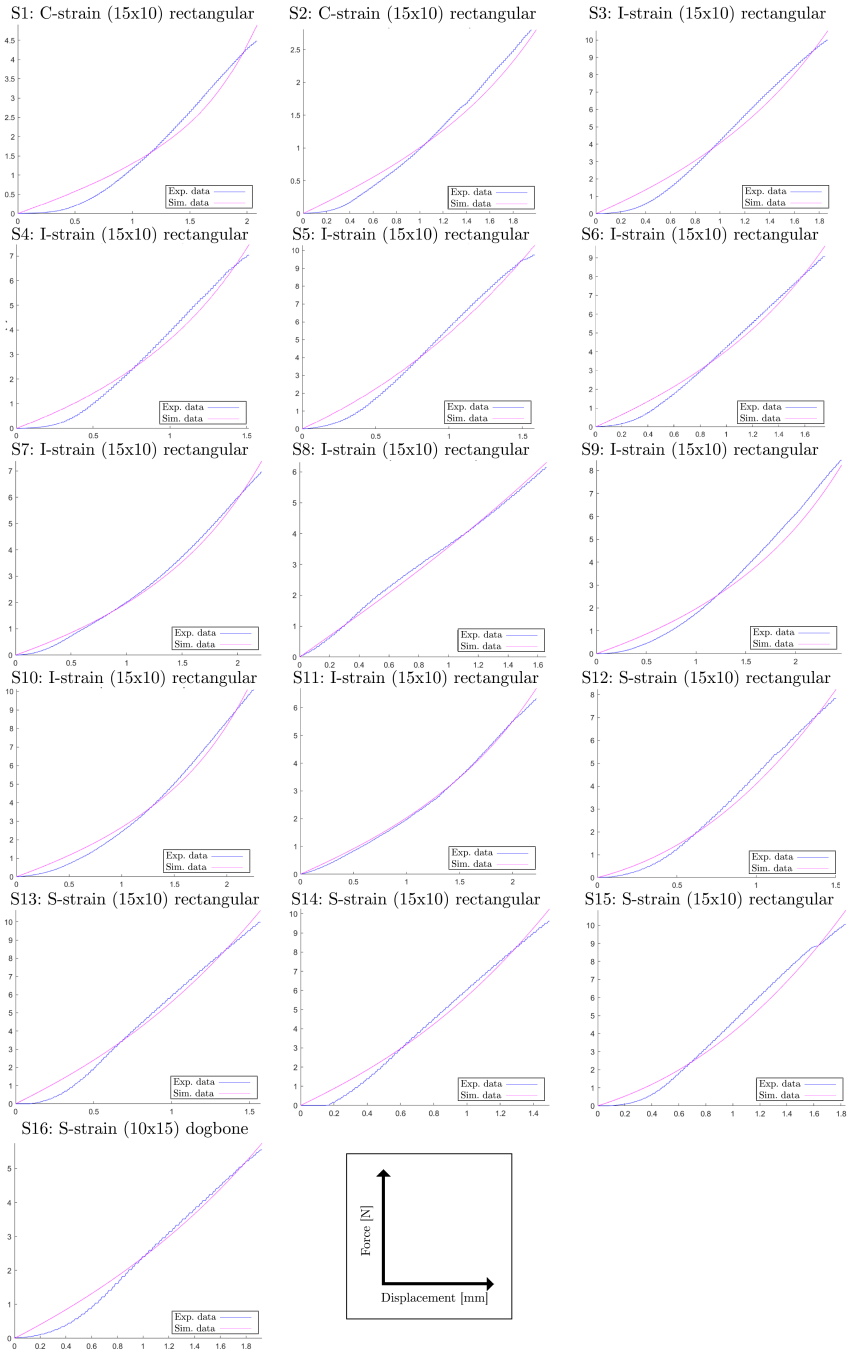

Figure 34: The BE-FC model force-length relationships ("Sim. data") plotted with the experimentally obtained force-length relationships ("Exp. data").

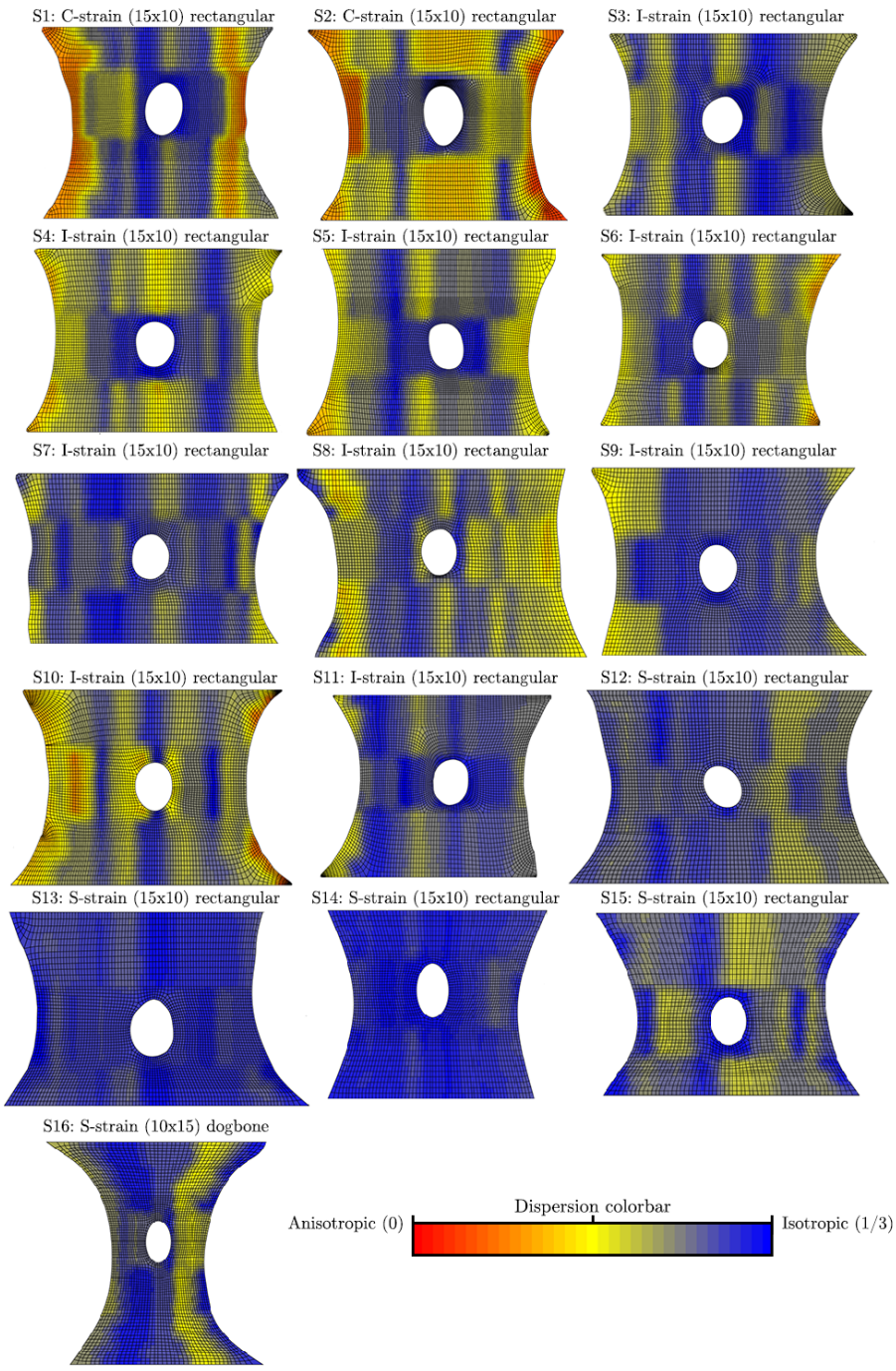

Figure 35: The collagen fibre dispersion κ of each BE-FC model. The color bar shows the color map for κ. The color bar ranges from from fully anisotropic (0) to fully isotropic (1/3).

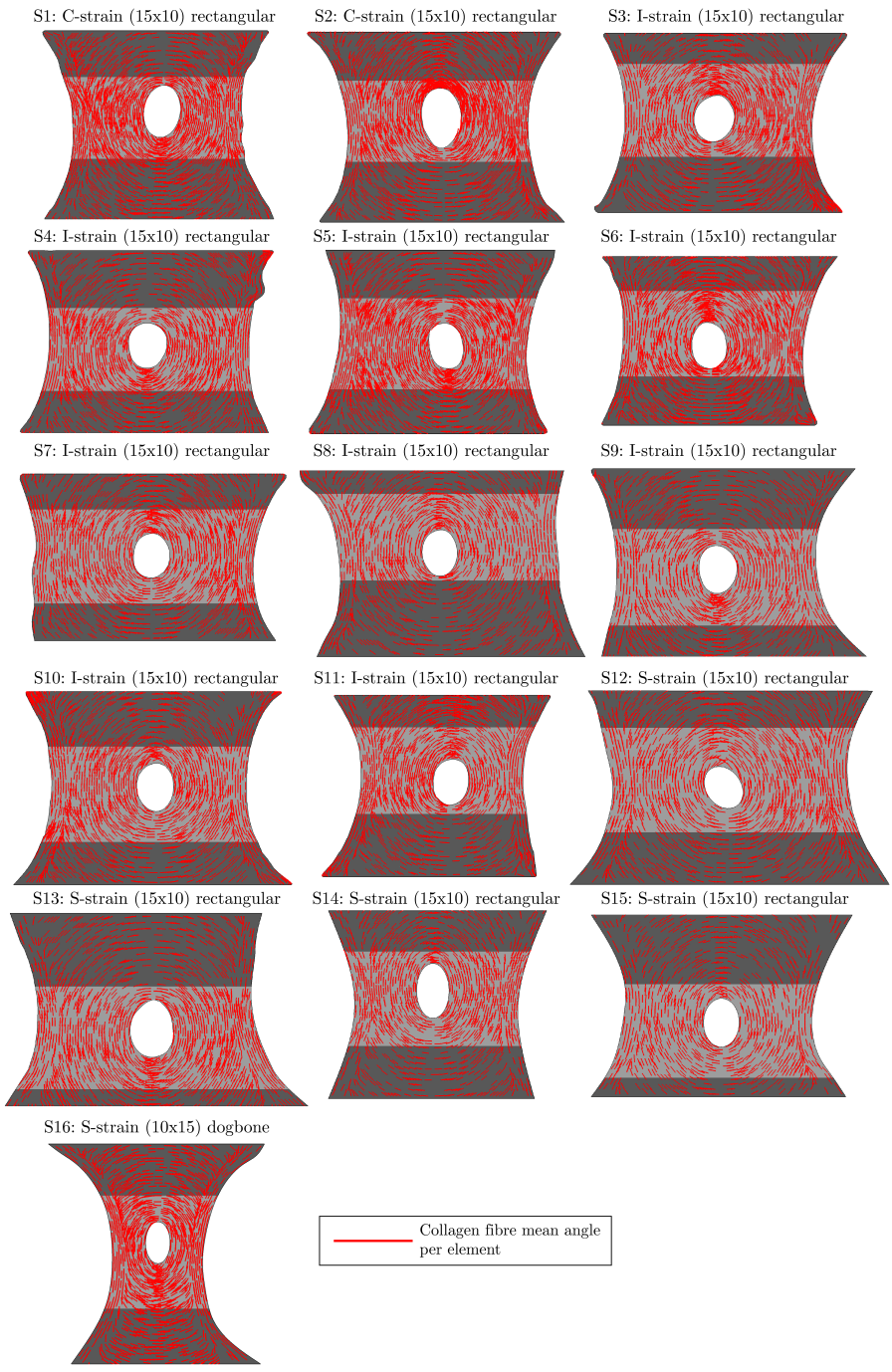

Figure 36: The collagen fibre mean angles Θ of each BE-FC model (for 70% of each model its elements).

10 Appendix C - Bio-engineered Fibrous Cap Models - Peak Values

Table. 7 presents the peak values of the normal stresses and strains in the BE-FC models. In addition, Table. 8 presents the same data for the local stresses and strains.

Table 7: The peak values of the normal stresses and strains in the BE-FC models. Stresses in MPa.

#	S_x	S_y	S_{xy}	LE_x	LE_y	LE_{xy}
1	0.3766	3.4771	0.7882	−0.2367	0.4708	0.5623
2	0.1480	1.3290	0.3142	0.2215	0.4134	0.4666
3	1.0516	3.6263	1.6020	−0.2150	0.4491	0.4343
4	0.4189	2.7691	0.8965	−0.1628	0.3380	0.3677
5	0.7144	4.0601	1.4690	−0.1888	0.3904	0.4083
6	0.6305	3.1496	1.1534	−0.1746	0.3896	0.4120
7	0.5385	2.6997	0.9641	−0.2080	0.4491	0.4522
8	0.3414	1.3210	0.5526	−0.1812	0.3878	0.4231
9	0.5993	3.2896	1.0760	0.2524	0.4653	0.5219
10	1.2000	5.8440	2.0365	0.2481	0.5247	0.4677
11	0.5895	2.6842	0.9379	−0.2222	0.4651	0.4730
12	0.5783	2.4476	0.7939	−0.1543	0.3851	0.4019
13	0.7703	3.1526	1.2255	0.1862	0.3664	0.4543
14	0.8322	2.9464	1.2525	0.1815	0.3581	0.4089
15	0.7472	3.1980	1.0496	−0.1900	0.4244	0.4540
16	0.5917	3.3960	0.8409	−0.1538	0.3140	0.4469

Table 8: The peak values of the local stresses and strains in the BE-FC models. Stresses in MPa.

#	$S_{\text{in-fib}}$	$S_{\text{across-fib}}$	$LE_{\text{in-fib}}$	$LE_{\text{across-fib}}$
1	3.4805	0.3346	0.4698	0.2655
2	1.3573	0.1435	0.4134	0.2013
3	4.0134	1.3120	0.4487	0.2840
4	3.0323	0.4267	0.3311	0.2561
5	4.5793	0.7259	0.3877	0.2943
6	3.5517	0.8175	0.3707	0.3211
7	2.6490	0.5151	0.4970	0.3581
8	1.4646	0.4545	0.3918	0.2547
9	3.2930	0.6747	0.4650	0.3968
10	5.8637	1.0181	0.4202	0.4574
11	2.6930	0.6800	0.4547	0.3419
12	2.4633	0.9607	0.3227	0.3210
13	3.5968	0.8626	0.3761	0.2083
14	3.2180	1.0234	0.3572	0.1938
15	3.2082	1.1588	0.4007	0.3611
16	3.3610	0.9852	0.3279	0.2888

11 Appendix D - Bio-engineered Fibrous Cap Models - Locations

The locations of the normal stresses and strains their peak values in the BE-FC models are given in Table. 9. Table. 10 presents this data for the local stresses and strains. These tables also present the experimentally obtained BE-FC rupture initiation locations. When the experimentally obtained rupture initiation location coincides with the model peak stress or strain value location, said value is highlighted with red in the tables.

Table 9: An overview of each normal stress/strain its peak value location in the BE-FC models. The table its second column presents the experimentally obtained rupture initiation location of each BE-FC (Exp. data). If a stress/strain its peak value location coincides with the experimentally obtained actual rupture initiation location, said value is highlighted in red.

#	Exp. data	S_x	S_y	S_{xy}	LE_x	LE_y	LE_{xy}
1	BD_{UR}	BD_{UL}	BD_{BL}	BD_{UL}	BD_{BR}	SI_{MR}	SI_{BL}
2	–	BD_{UR}	BD_{BL}	BD_{BR}	SI_{BM}	BD_{BL}	SI_{BL}
3	BD_{UL}	BD_{UL}	BD_{UL}	BD_{BL}	SI_{MR}	SI_{MR}	BD_{BL}
4	BD_{ML}	BD_{BL}	BD_{MR}	BD_{UL}	SI_{ML}	SI_{ML}	SI_{UL}
5	SI_{ML}	BD_{UL}	BD_{UL}	BD_{UL}	SI_{MR}	SI_{MR}	SI_{UL}
6	SI_{BL}	BD_{UR}	BD_{BR}	BD_{BR}	BD_{MR}	BD_{UR}	BD_{BR}
7	BD_{BR}	BD_{BR}	BD_{MR}	BD_{BR}	SI_{ML}	BD_{UR}	SI_{UL}
8	SI_{MR}	BD_{UR}	BD_{BL}	BD_{UL}	SI_{MR}	SI_{ML}	BD_{UR}
9	SI_{MR}	BD_{UR}	BD_{ML}	BD_{UL}	SI_{BM}	BD_{ML}	SI_{UL}
10	SI_{UR}	BD_{BL}	BD_{ML}	BD_{BL}	SI_{UM}	BD_{BL}	SI_{BR}
11	BD_{UL}	BD_{BL}	BD_{MR}	BD_{BR}	SI_{MR}	SI_{MR}	SI_{UL}
12	BD_{BL}	BD_{UR}	BD_{MR}	BD_{UR}	BD_{ML}	BD_{UR}	BD_{UL}
13	SI_{UM}	BD_{UR}	BD_{UR}	BD_{UR}	SI_{UM}	SI_{MR}	BD_{UL}
14	BD_{UR}	BD_{BR}	BD_{MR}	BD_{BR}	SI_{BM}	SI_{ML}	BD_{BL}
15	BD_{ML}	BD_{BL}	BD_{UL}	BD_{UL}	BD_{MR}	BD_{BR}	BD_{BL}
16	BD_{UL}	BD_{BR}	BD_{BR}	BD_{BL}	BD_{MR}	BD_{BR}	BD_{BR}

Table 10: An overview of each local stress/strain its peak value location in the BE-FC models. The table its second column presents the experimentally obtained rupture initiation location of each BE-FC (Exp. data). If a stress/strain its peak value location coincides with the experimentally obtained actual rupture initiation location, said value is highlighted in red.

#	Exp. data	$S_{\text{in-fib}}$	$S_{\text{across-fib}}$	$LE_{\text{in-fib}}$	$LE_{\text{across-fib}}$
1	BD_{UR}	BD_{BL}	BD_{BR}	SI_{MR}	BD_{BM}
2	–	BD_{BL}	BD_{BR}	BD_{BL}	BD_{BR}
3	BD_{UL}	BD_{BL}	BD_{UL}	SI_{MR}	BD_{UR}
4	BD_{ML}	BD_{UL}	BD_{BL}	SI_{MR}	BD_{BR}
5	SI_{ML}	BD_{UL}	BD_{BR}	SI_{MR}	BD_{UL}
6	SI_{BL}	BD_{BR}	BD_{UR}	BD_{BR}	BD_{UR}
7	BD_{BR}	BD_{MR}	BD_{BL}	BD_{UR}	BD_{UR}
8	SI_{MR}	BD_{BL}	BD_{UR}	SI_{MR}	BD_{UR}
9	SI_{MR}	BD_{ML}	BD_{BR}	BD_{ML}	BD_{BL}
10	SI_{UR}	BD_{ML}	BD_{BL}	BD_{MR}	BD_{BR}
11	BD_{UL}	BD_{MR}	BD_{UL}	SI_{MR}	BD_{UL}
12	BD_{BL}	BD_{MR}	BD_{UR}	BD_{BR}	BD_{UL}
13	SI_{UM}	BD_{UR}	BD_{BL}	BD_{UR}	BD_{BL}
14	BD_{UR}	BD_{BR}	BD_{BR}	SI_{ML}	BD_{BR}
15	BD_{ML}	BD_{UL}	BD_{BR}	BD_{UL}	BD_{BL}
16	BD_{UL}	BD_{BR}	BD_{BR}	BD_{BR}	BD_{BR}

12 Appendix D - Bio-engineered Fibrous Cap Models - Distributions

The distribution of S_y, $S_{\text{in-fib}}$, LE_{xy}, LE_y, $LE_{\text{in-fib}}$, and $LE_{\text{across-fib}}$ in each BE-FC model is presented in the following 16 figures.

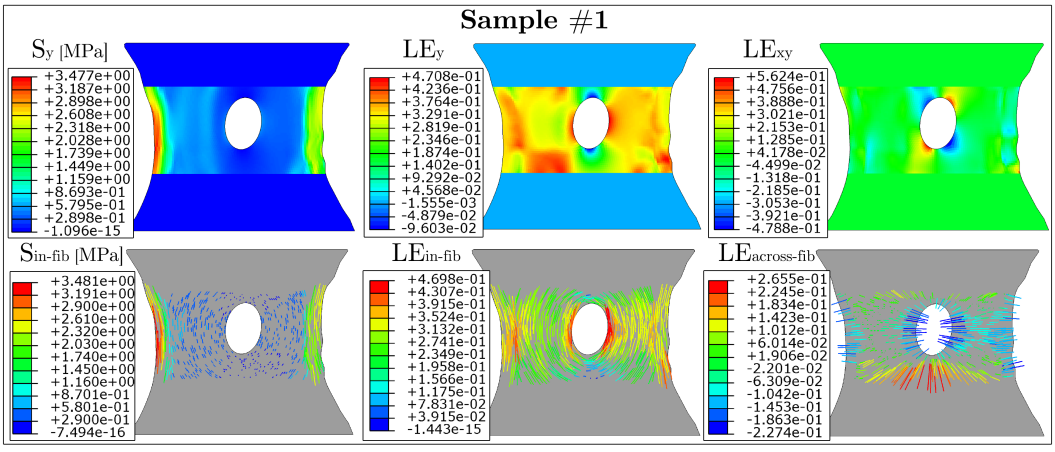

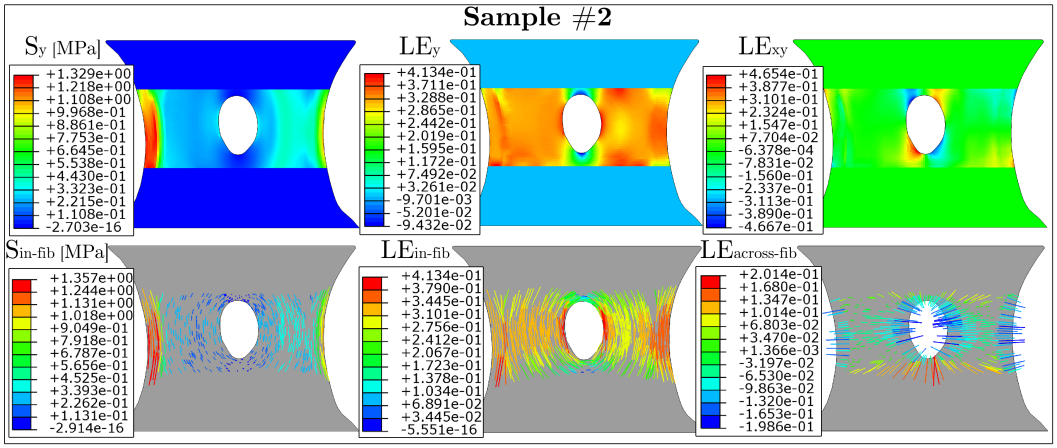
Sample #2
Sy [MPa]
+1.329e+00
+1.218e+00
+1.108e+00
+9.968e-01
+8.861e-01
+7.753e-01
+6.645e-01
+5.538e-01
+4.430e-01
+3.323e-01
+2.215e-01
+1.108e-01
-2.703e-16
LEy
+4.134e-01
+3.711e-01
+3.288e-01
+2.865e-01
+2.442e-01
+2.019e-01
+1.595e-01
+1.172e-01
+7.492e-02
+3.261e-02
-9.701e-03
-5.201e-02
-9.432e-02
LExy
+4.654e-01
+3.877e-01
+3.101e-01
+2.324e-01
+1.547e-01
+7.704e-02
-6.378e-04
-7.831e-02
-1.560e-01
-2.337e-01
-3.113e-01
-3.890e-01
-4.667e-01
Sin-fib [MPa]
+1.357e+00
+1.244e+00
+1.131e+00
+1.018e+00
+9.049e-01
+7.918e-01
+6.787e-01
+5.656e-01
+4.525e-01
+3.393e-01
+2.262e-01
+1.131e-01
-2.914e-16
LEin-fib
+4.134e-01
+3.790e-01
+3.445e-01
+3.101e-01
+2.756e-01
+2.412e-01
+2.067e-01
+1.723e-01
+1.378e-01
+1.034e-01
+6.891e-02
+3.445e-02
-5.551e-16
LEacross-fib
+2.014e-01
+1.680e-01
+1.347e-01
+1.014e-01
+6.803e-02
+3.470e-02
+1.366e-03
-3.197e-02
-6.530e-02
-9.863e-02
-1.320e-01
-1.653e-01
-1.986e-01

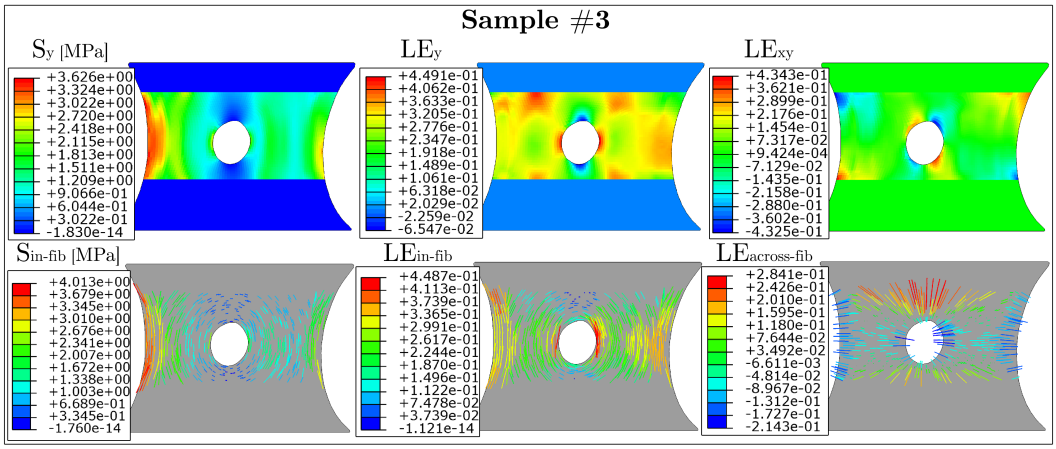
Sample #3
Sy [MPa]
+3.626e+00
+3.324e+00
+3.022e+00
+2.720e+00
+2.418e+00
+2.115e+00
+1.813e+00
+1.511e+00
+1.209e+00
+9.066e-01
+6.044e-01
+3.022e-01
-1.830e-14
LEy
+4.491e-01
+4.062e-01
+3.633e-01
+3.205e-01
+2.776e-01
+2.347e-01
+1.918e-01
+1.489e-01
+1.061e-01
+6.318e-02
+2.029e-02
-2.259e-02
-6.547e-02
LExy
+4.343e-01
+3.621e-01
+2.899e-01
+2.176e-01
+1.454e-01
+7.317e-02
+9.424e-04
-7.129e-02
-1.435e-01
-2.158e-01
-2.880e-01
-3.602e-01
-4.325e-01
Sin-fib [MPa]
+4.013e+00
+3.679e+00
+3.345e+00
+3.010e+00
+2.676e+00
+2.341e+00
+2.007e+00
+1.672e+00
+1.338e+00
+1.003e+00
+6.689e-01
+3.345e-01
-1.760e-14
LEin-fib
+4.487e-01
+4.113e-01
+3.739e-01
+3.365e-01
+2.991e-01
+2.617e-01
+2.244e-01
+1.870e-01
+1.496e-01
+1.122e-01
+7.478e-02
+3.739e-02
-1.121e-14
LEacross-fib
+2.841e-01
+2.426e-01
+2.010e-01
+1.595e-01
+1.180e-01
+7.644e-02
+3.492e-02
-6.611e-03
-4.814e-02
-8.967e-02
-1.312e-01
-1.727e-01
-2.143e-01

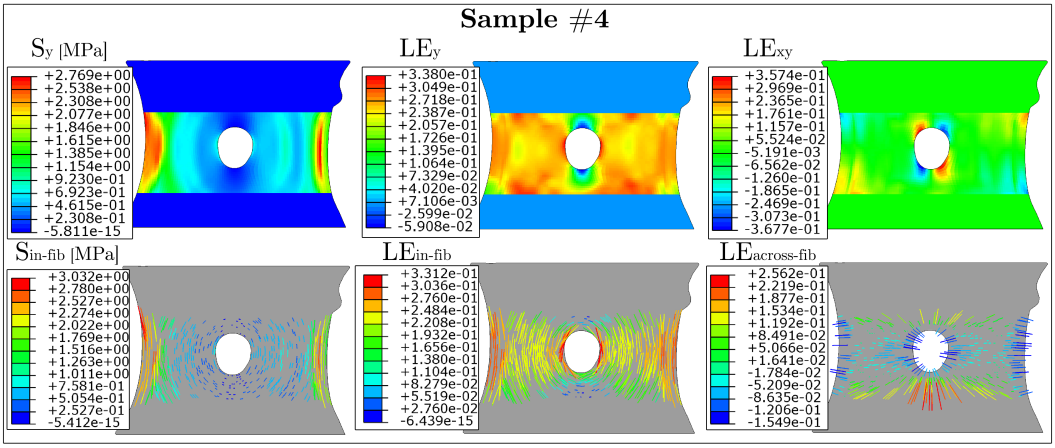
Sample #4
Sy [MPa]
+2.769e+00
+2.538e+00
+2.308e+00
+2.077e+00
+1.846e+00
+1.615e+00
+1.385e+00
+1.154e+00
+9.230e-01
+6.923e-01
+4.615e-01
+2.308e-01
-5.811e-15
LEy
+3.380e-01
+3.049e-01
+2.718e-01
+2.387e-01
+2.057e-01
+1.726e-01
+1.395e-01
+1.064e-01
+7.329e-02
+4.020e-02
+7.106e-03
-2.599e-02
-5.908e-02
LExy
+3.574e-01
+2.969e-01
+2.365e-01
+1.761e-01
+1.157e-01
+5.524e-02
-5.191e-03
-6.562e-02
-1.260e-01
-1.865e-01
-2.469e-01
-3.073e-01
-3.677e-01
Sin-fib [MPa]
+3.032e+00
+2.780e+00
+2.527e+00
+2.274e+00
+2.022e+00
+1.769e+00
+1.516e+00
+1.263e+00
+1.011e+00
+7.581e-01
+5.054e-01
+2.527e-01
-5.412e-15
LEin-fib
+3.312e-01
+3.036e-01
+2.760e-01
+2.484e-01
+2.208e-01
+1.932e-01
+1.656e-01
+1.380e-01
+1.104e-01
+8.279e-02
+5.519e-02
+2.760e-02
-6.439e-15
LEacross-fib
+2.562e-01
+2.219e-01
+1.877e-01
+1.534e-01
+1.192e-01
+8.491e-02
+5.066e-02
+1.641e-02
-1.784e-02
-5.209e-02
-8.635e-02
-1.206e-01
-1.549e-01

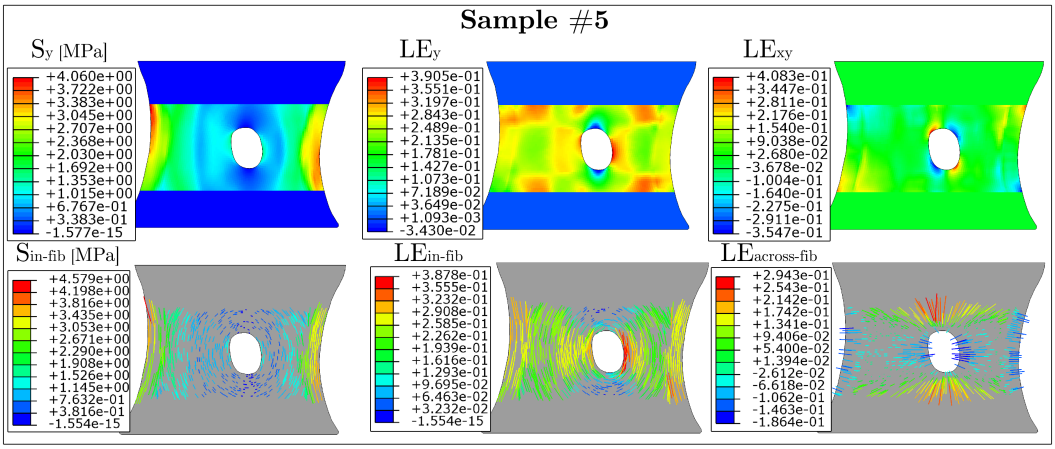
Sample #5
Sy [MPa]
+4.060e+00
+3.722e+00
+3.383e+00
+3.045e+00
+2.707e+00
+2.368e+00
+2.030e+00
+1.692e+00
+1.353e+00
+1.015e+00
+6.767e-01
+3.383e-01
-1.577e-15
LEy
+3.905e-01
+3.551e-01
+3.197e-01
+2.843e-01
+2.489e-01
+2.135e-01
+1.781e-01
+1.427e-01
+1.073e-01
+7.189e-02
+3.649e-02
+1.093e-03
-3.430e-02
LExy
+4.083e-01
+3.447e-01
+2.811e-01
+2.176e-01
+1.540e-01
+9.038e-02
+2.680e-02
-3.678e-02
-1.004e-01
-1.640e-01
-2.275e-01
-2.911e-01
-3.547e-01
Sin-fib [MPa]
+4.579e+00
+4.198e+00
+3.816e+00
+3.435e+00
+3.053e+00
+2.671e+00
+2.290e+00
+1.908e+00
+1.526e+00
+1.145e+00
+7.632e-01
+3.816e-01
-1.554e-15
LEin-fib
+3.878e-01
+3.555e-01
+3.232e-01
+2.908e-01
+2.585e-01
+2.262e-01
+1.939e-01
+1.616e-01
+1.293e-01
+9.695e-02
+6.463e-02
+3.232e-02
-1.554e-15
LEacross-fib
+2.943e-01
+2.543e-01
+2.142e-01
+1.742e-01
+1.341e-01
+9.406e-02
+5.400e-02
+1.394e-02
-2.612e-02
-6.618e-02
-1.062e-01
-1.463e-01
-1.864e-01

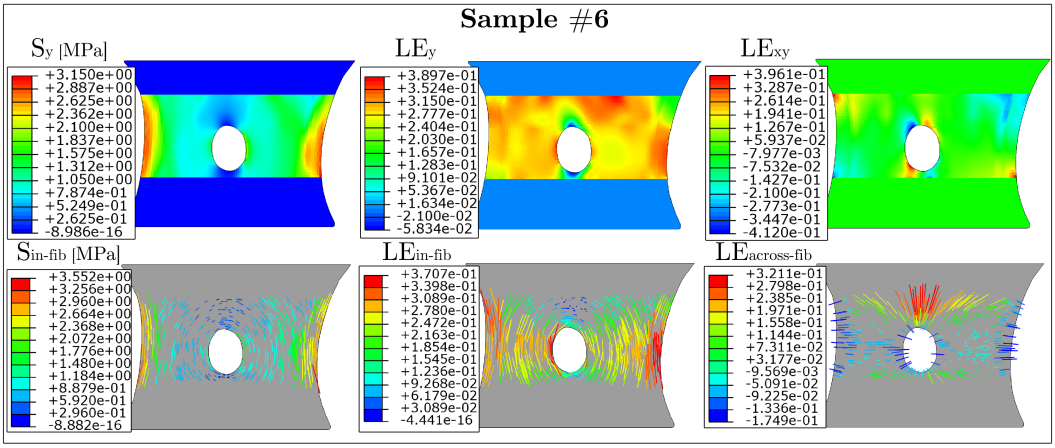
Sample #6
Sy [MPa]
+3.150e+00
+2.887e+00
+2.625e+00
+2.362e+00
+2.100e+00
+1.837e+00
+1.575e+00
+1.312e+00
+1.050e+00
+7.874e-01
+5.249e-01
+2.625e-01
-8.986e-16
LEy
+3.897e-01
+3.524e-01
+3.150e-01
+2.777e-01
+2.404e-01
+2.030e-01
+1.657e-01
+1.283e-01
+9.101e-02
+5.367e-02
+1.634e-02
-2.100e-02
-5.834e-02
LExy
+3.961e-01
+3.287e-01
+2.614e-01
+1.941e-01
+1.267e-01
+5.937e-02
-7.977e-03
-7.532e-02
-1.427e-01
-2.100e-01
-2.773e-01
-3.447e-01
-4.120e-01
Sin-fib [MPa]
+3.552e+00
+3.256e+00
+2.960e+00
+2.664e+00
+2.368e+00
+2.072e+00
+1.776e+00
+1.480e+00
+1.184e+00
+8.879e-01
+5.920e-01
+2.960e-01
-8.882e-16
LEin-fib
+3.707e-01
+3.398e-01
+3.089e-01
+2.780e-01
+2.472e-01
+2.163e-01
+1.854e-01
+1.545e-01
+1.236e-01
+9.268e-02
+6.179e-02
+3.089e-02
-4.441e-16
LEacross-fib
+3.211e-01
+2.798e-01
+2.385e-01
+1.971e-01
+1.558e-01
+1.144e-01
+7.311e-02
+3.177e-02
-9.569e-03
-5.091e-02
-9.225e-02
-1.336e-01
-1.749e-01

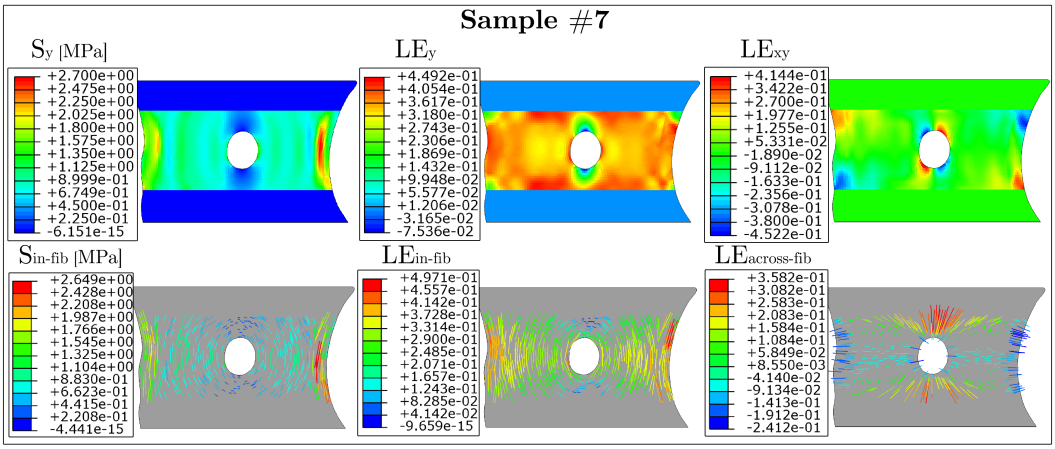
Sample #7
Sy [MPa]
+2.700e+00
+2.475e+00
+2.250e+00
+2.025e+00
+1.800e+00
+1.575e+00
+1.350e+00
+1.125e+00
+8.999e-01
+6.749e-01
+4.500e-01
+2.250e-01
-6.151e-15
LEy
+4.492e-01
+4.054e-01
+3.617e-01
+3.180e-01
+2.743e-01
+2.306e-01
+1.869e-01
+1.432e-01
+9.948e-02
+5.577e-02
+1.206e-02
-3.165e-02
-7.536e-02
LExy
+4.144e-01
+3.422e-01
+2.700e-01
+1.977e-01
+1.255e-01
+5.331e-02
-1.890e-02
-9.112e-02
-1.633e-01
-2.356e-01
-3.078e-01
-3.800e-01
-4.522e-01
Sin-fib [MPa]
+2.649e+00
+2.428e+00
+2.208e+00
+1.987e+00
+1.766e+00
+1.545e+00
+1.325e+00
+1.104e+00
+8.830e-01
+6.623e-01
+4.415e-01
+2.208e-01
-4.441e-15
LEin-fib
+4.971e-01
+4.557e-01
+4.142e-01
+3.728e-01
+3.314e-01
+2.900e-01
+2.485e-01
+2.071e-01
+1.657e-01
+1.243e-01
+8.285e-02
+4.142e-02
-9.659e-15
LEacross-fib
+3.582e-01
+3.082e-01
+2.583e-01
+2.083e-01
+1.584e-01
+1.084e-01
+5.849e-02
+8.550e-03
-4.140e-02
-9.134e-02
-1.413e-01
-1.912e-01
-2.412e-01

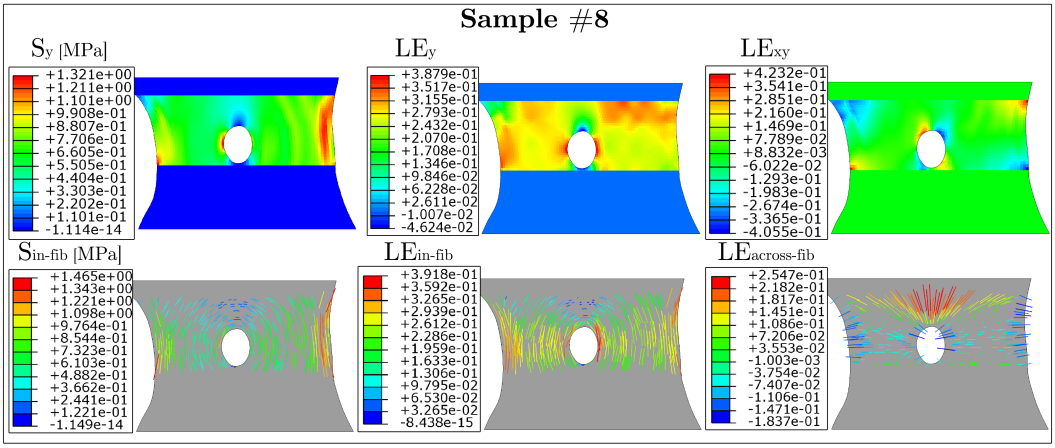
Sample #8
Sy [MPa]
+1.321e+00
+1.211e+00
+1.101e+00
+9.908e-01
+8.807e-01
+7.706e-01
+6.605e-01
+5.505e-01
+4.404e-01
+3.303e-01
+2.202e-01
+1.101e-01
-1.114e-14
LEy
+3.879e-01
+3.517e-01
+3.155e-01
+2.793e-01
+2.432e-01
+2.070e-01
+1.708e-01
+1.346e-01
+9.846e-02
+6.228e-02
+2.611e-02
-1.007e-02
-4.624e-02
LExy
+4.232e-01
+3.541e-01
+2.851e-01
+2.160e-01
+1.469e-01
+7.789e-02
+8.832e-03
-6.022e-02
-1.293e-01
-1.983e-01
-2.674e-01
-3.365e-01
-4.055e-01
Sin-fib [MPa]
+1.465e+00
+1.343e+00
+1.221e+00
+1.098e+00
+9.764e-01
+8.544e-01
+7.323e-01
+6.103e-01
+4.882e-01
+3.662e-01
+2.441e-01
+1.221e-01
-1.149e-14
LEin-fib
+3.918e-01
+3.592e-01
+3.265e-01
+2.939e-01
+2.612e-01
+2.286e-01
+1.959e-01
+1.633e-01
+1.306e-01
+9.795e-02
+6.530e-02
+3.265e-02
-8.438e-15
LEacross-fib
+2.547e-01
+2.182e-01
+1.817e-01
+1.451e-01
+1.086e-01
+7.206e-02
+3.553e-02
-1.003e-03
-3.754e-02
-7.407e-02
-1.106e-01
-1.471e-01
-1.837e-01

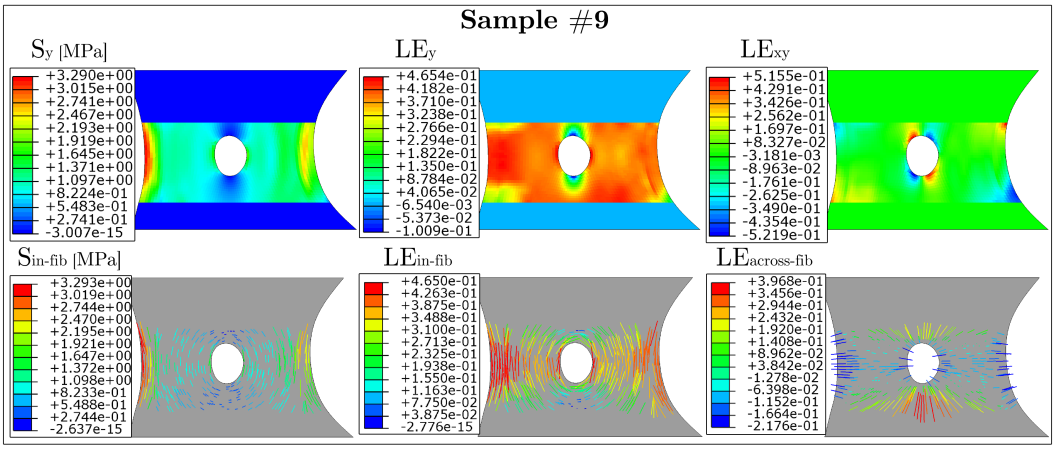
Sample #9
Sy [MPa]
+3.290e+00
+3.015e+00
+2.741e+00
+2.467e+00
+2.193e+00
+1.919e+00
+1.645e+00
+1.371e+00
+1.097e+00
+8.224e-01
+5.483e-01
+2.741e-01
-3.007e-15
LEy
+4.654e-01
+4.182e-01
+3.710e-01
+3.238e-01
+2.766e-01
+2.294e-01
+1.822e-01
+1.350e-01
+8.784e-02
+4.065e-02
-6.540e-03
-5.373e-02
-1.009e-01
LExy
+5.155e-01
+4.291e-01
+3.426e-01
+2.562e-01
+1.697e-01
+8.327e-02
-3.181e-03
-8.963e-02
-1.761e-01
-2.625e-01
-3.490e-01
-4.354e-01
-5.219e-01
Sin-fib [MPa]
+3.293e+00
+3.019e+00
+2.744e+00
+2.470e+00
+2.195e+00
+1.921e+00
+1.647e+00
+1.372e+00
+1.098e+00
+8.233e-01
+5.488e-01
+2.744e-01
-2.637e-15
LEin-fib
+4.650e-01
+4.263e-01
+3.875e-01
+3.488e-01
+3.100e-01
+2.713e-01
+2.325e-01
+1.938e-01
+1.550e-01
+1.163e-01
+7.750e-02
+3.875e-02
-2.776e-15
LEacross-fib
+3.968e-01
+3.456e-01
+2.944e-01
+2.432e-01
+1.920e-01
+1.408e-01
+8.962e-02
+3.842e-02
-1.278e-02
-6.398e-02
-1.152e-01
-1.664e-01
-2.176e-01

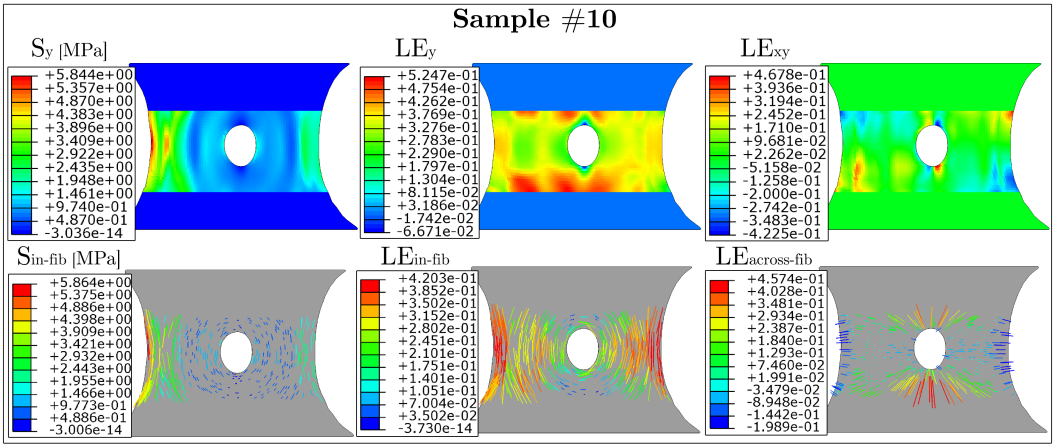
Sample #10
Sy [MPa]
+5.844e+00
+5.357e+00
+4.870e+00
+4.383e+00
+3.896e+00
+3.409e+00
+2.922e+00
+2.435e+00
+1.948e+00
+1.461e+00
+9.740e-01
+4.870e-01
-3.036e-14
LEy
+5.247e-01
+4.754e-01
+4.262e-01
+3.769e-01
+3.276e-01
+2.783e-01
+2.290e-01
+1.797e-01
+1.304e-01
+8.115e-02
+3.186e-02
-1.742e-02
-6.671e-02
LExy
+4.678e-01
+3.936e-01
+3.194e-01
+2.452e-01
+1.710e-01
+9.681e-02
+2.262e-02
-5.158e-02
-1.258e-01
-2.000e-01
-2.742e-01
-3.483e-01
-4.225e-01
Sin-fib [MPa]
+5.864e+00
+5.375e+00
+4.886e+00
+4.398e+00
+3.909e+00
+3.421e+00
+2.932e+00
+2.443e+00
+1.955e+00
+1.466e+00
+9.773e-01
+4.886e-01
-3.006e-14
LEin-fib
+4.203e-01
+3.852e-01
+3.502e-01
+3.152e-01
+2.802e-01
+2.451e-01
+2.101e-01
+1.751e-01
+1.401e-01
+1.051e-01
+7.004e-02
+3.502e-02
-3.730e-14
LEacross-fib
+4.574e-01
+4.028e-01
+3.481e-01
+2.934e-01
+2.387e-01
+1.840e-01
+1.293e-01
+7.460e-02
+1.991e-02
-3.479e-02
-8.948e-02
-1.442e-01
-1.989e-01

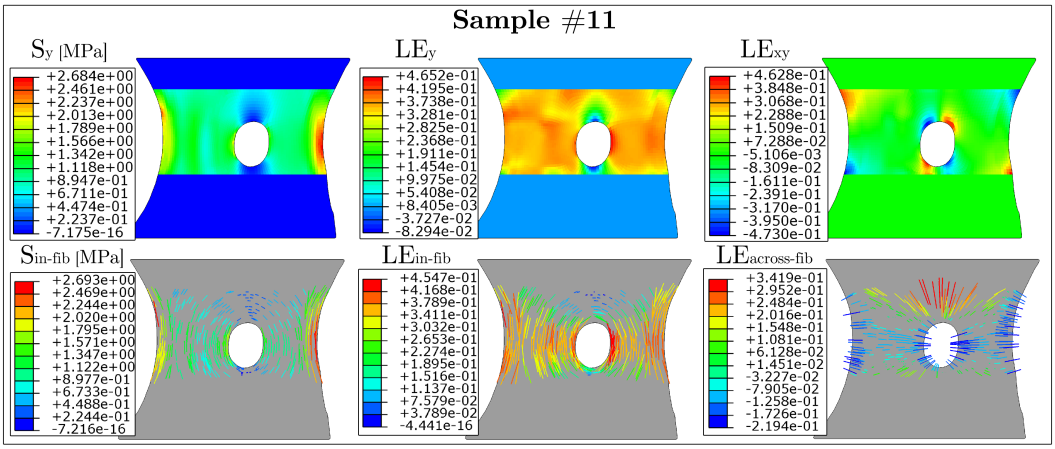
Sample #11
Sy [MPa]
+2.684e+00
+2.461e+00
+2.237e+00
+2.013e+00
+1.789e+00
+1.566e+00
+1.342e+00
+1.118e+00
+8.947e-01
+6.711e-01
+4.474e-01
+2.237e-01
-7.175e-16
LEy
+4.652e-01
+4.195e-01
+3.738e-01
+3.281e-01
+2.825e-01
+2.368e-01
+1.911e-01
+1.454e-01
+9.975e-02
+5.408e-02
+8.405e-03
-3.727e-02
-8.294e-02
LExy
+4.628e-01
+3.848e-01
+3.068e-01
+2.288e-01
+1.509e-01
+7.288e-02
-5.106e-03
-8.309e-02
-1.611e-01
-2.391e-01
-3.170e-01
-3.950e-01
-4.730e-01
Sin-fib [MPa]
+2.693e+00
+2.469e+00
+2.244e+00
+2.020e+00
+1.795e+00
+1.571e+00
+1.347e+00
+1.122e+00
+8.977e-01
+6.733e-01
+4.488e-01
+2.244e-01
-7.216e-16
LEin-fib
+4.547e-01
+4.168e-01
+3.789e-01
+3.411e-01
+3.032e-01
+2.653e-01
+2.274e-01
+1.895e-01
+1.516e-01
+1.137e-01
+7.579e-02
+3.789e-02
-4.441e-16
LEacross-fib
+3.419e-01
+2.952e-01
+2.484e-01
+2.016e-01
+1.548e-01
+1.081e-01
+6.128e-02
+1.451e-02
-3.227e-02
-7.905e-02
-1.258e-01
-1.726e-01
-2.194e-01

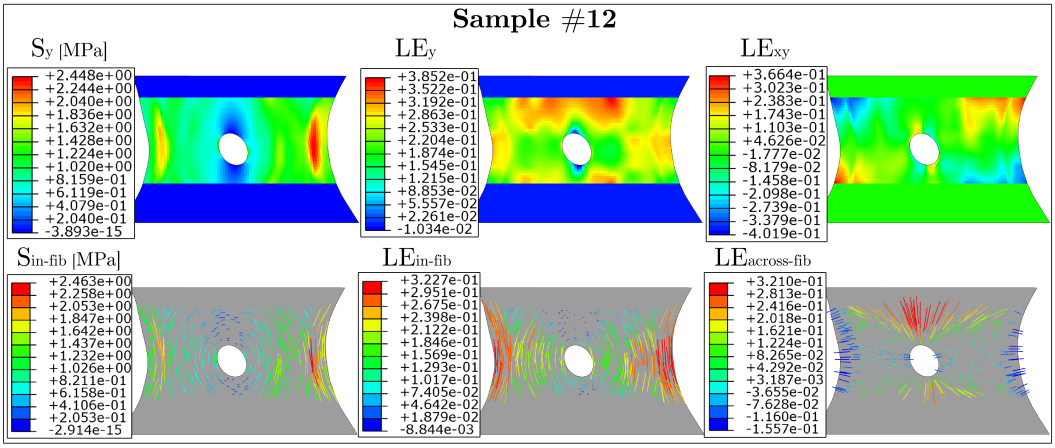
Sample #12
Sy [MPa]
+2.448e+00
+2.244e+00
+2.040e+00
+1.836e+00
+1.632e+00
+1.428e+00
+1.224e+00
+1.020e+00
+8.159e-01
+6.119e-01
+4.079e-01
+2.040e-01
-3.893e-15
LEy
+3.852e-01
+3.522e-01
+3.192e-01
+2.863e-01
+2.533e-01
+2.204e-01
+1.874e-01
+1.545e-01
+1.215e-01
+8.853e-02
+5.557e-02
+2.261e-02
-1.034e-02
LExy
+3.664e-01
+3.023e-01
+2.383e-01
+1.743e-01
+1.103e-01
+4.626e-02
-1.777e-02
-8.179e-02
-1.458e-01
-2.098e-01
-2.739e-01
-3.379e-01
-4.019e-01
Sin-fib [MPa]
+2.463e+00
+2.258e+00
+2.053e+00
+1.847e+00
+1.642e+00
+1.437e+00
+1.232e+00
+1.026e+00
+8.211e-01
+6.158e-01
+4.106e-01
+2.053e-01
-2.914e-15
LEin-fib
+3.227e-01
+2.951e-01
+2.675e-01
+2.398e-01
+2.122e-01
+1.846e-01
+1.569e-01
+1.293e-01
+1.017e-01
+7.405e-02
+4.642e-02
+1.879e-02
-8.844e-03
LEacross-fib
+3.210e-01
+2.813e-01
+2.416e-01
+2.018e-01
+1.621e-01
+1.224e-01
+8.265e-02
+4.292e-02
+3.187e-03
-3.655e-02
-7.628e-02
-1.160e-01
-1.557e-01

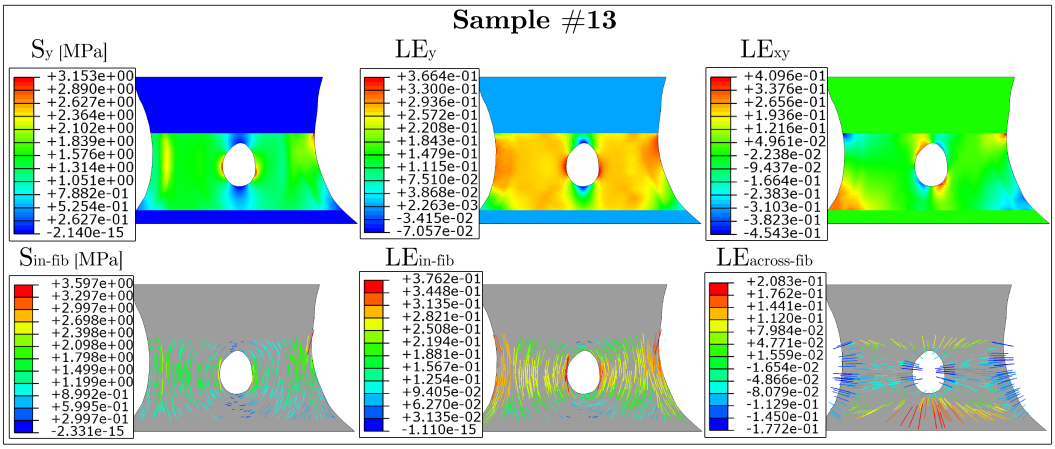
Sample #13
Sy [MPa]
+3.153e+00
+2.890e+00
+2.627e+00
+2.364e+00
+2.102e+00
+1.839e+00
+1.576e+00
+1.314e+00
+1.051e+00
+7.882e-01
+5.254e-01
+2.627e-01
-2.140e-15
LEy
+3.664e-01
+3.300e-01
+2.936e-01
+2.572e-01
+2.208e-01
+1.843e-01
+1.479e-01
+1.115e-01
+7.510e-02
+3.868e-02
+2.263e-03
-3.415e-02
-7.057e-02
LExy
+4.096e-01
+3.376e-01
+2.656e-01
+1.936e-01
+1.216e-01
+4.961e-02
-2.238e-02
-9.437e-02
-1.664e-01
-2.383e-01
-3.103e-01
-3.823e-01
-4.543e-01
Sin-fib [MPa]
+3.597e+00
+3.297e+00
+2.997e+00
+2.698e+00
+2.398e+00
+2.098e+00
+1.798e+00
+1.499e+00
+1.199e+00
+8.992e-01
+5.995e-01
+2.997e-01
-2.331e-15
LEin-fib
+3.762e-01
+3.448e-01
+3.135e-01
+2.821e-01
+2.508e-01
+2.194e-01
+1.881e-01
+1.567e-01
+1.254e-01
+9.405e-02
+6.270e-02
+3.135e-02
-1.110e-15
LEacross-fib
+2.083e-01
+1.762e-01
+1.441e-01
+1.120e-01
+7.984e-02
+4.771e-02
+1.559e-02
-1.654e-02
-4.866e-02
-8.079e-02
-1.129e-01
-1.450e-01
-1.772e-01

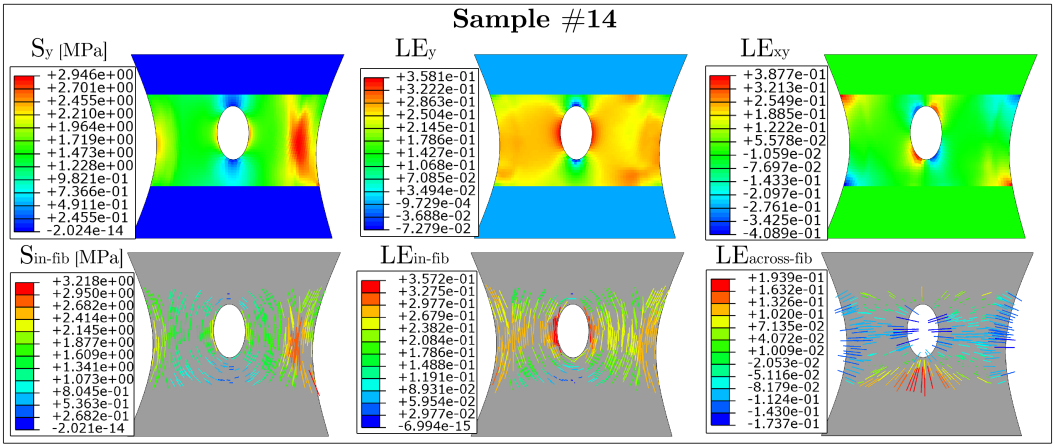
Sample #14
Sy [MPa]
+2.946e+00
+2.701e+00
+2.455e+00
+2.210e+00
+1.964e+00
+1.719e+00
+1.473e+00
+1.228e+00
+9.821e-01
+7.366e-01
+4.911e-01
+2.455e-01
-2.024e-14
LEy
+3.581e-01
+3.222e-01
+2.863e-01
+2.504e-01
+2.145e-01
+1.786e-01
+1.427e-01
+1.068e-01
+7.085e-02
+3.494e-02
-9.729e-04
-3.688e-02
-7.279e-02
LExy
+3.877e-01
+3.213e-01
+2.549e-01
+1.885e-01
+1.222e-01
+5.578e-02
-1.059e-02
-7.697e-02
-1.433e-01
-2.097e-01
-2.761e-01
-3.425e-01
-4.089e-01
Sin-fib [MPa]
+3.218e+00
+2.950e+00
+2.682e+00
+2.414e+00
+2.145e+00
+1.877e+00
+1.609e+00
+1.341e+00
+1.073e+00
+8.045e-01
+5.363e-01
+2.682e-01
-2.021e-14
LEin-fib
+3.572e-01
+3.275e-01
+2.977e-01
+2.679e-01
+2.382e-01
+2.084e-01
+1.786e-01
+1.488e-01
+1.191e-01
+8.931e-02
+5.954e-02
+2.977e-02
-6.994e-15
LEacross-fib
+1.939e-01
+1.632e-01
+1.326e-01
+1.020e-01
+7.135e-02
+4.072e-02
+1.009e-02
-2.053e-02
-5.116e-02
-8.179e-02
-1.124e-01
-1.430e-01
-1.737e-01

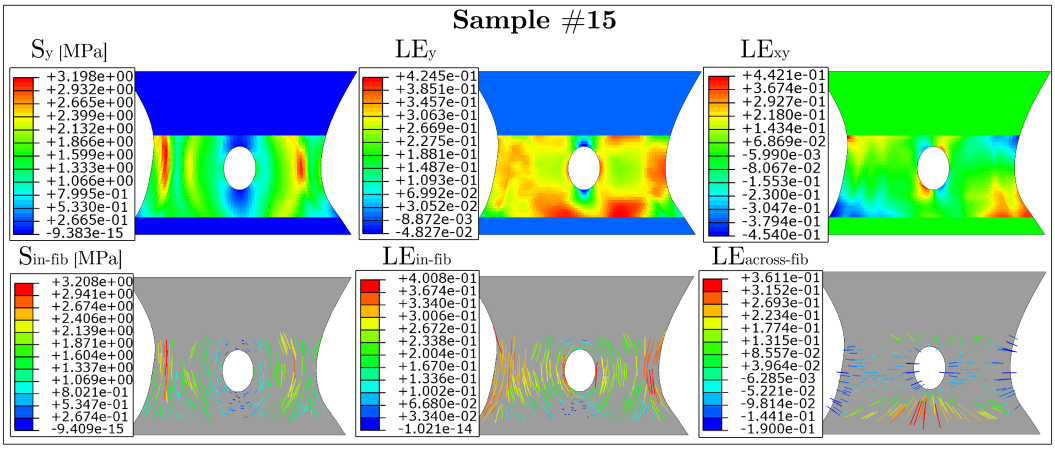
Sample #15
Sy [MPa]
+3.198e+00
+2.932e+00
+2.665e+00
+2.399e+00
+2.132e+00
+1.866e+00
+1.599e+00
+1.333e+00
+1.066e+00
+7.995e-01
+5.330e-01
+2.665e-01
-9.383e-15
LEy
+4.245e-01
+3.851e-01
+3.457e-01
+3.063e-01
+2.669e-01
+2.275e-01
+1.881e-01
+1.487e-01
+1.093e-01
+6.992e-02
+3.052e-02
-8.872e-03
-4.827e-02
LExy
+4.421e-01
+3.674e-01
+2.927e-01
+2.180e-01
+1.434e-01
+6.869e-02
-5.990e-03
-8.067e-02
-1.553e-01
-2.300e-01
-3.047e-01
-3.794e-01
-4.540e-01
Sin-fib [MPa]
+3.208e+00
+2.941e+00
+2.674e+00
+2.406e+00
+2.139e+00
+1.871e+00
+1.604e+00
+1.337e+00
+1.069e+00
+8.021e-01
+5.347e-01
+2.674e-01
-9.409e-15
LEin-fib
+4.008e-01
+3.674e-01
+3.340e-01
+3.006e-01
+2.672e-01
+2.338e-01
+2.004e-01
+1.670e-01
+1.336e-01
+1.002e-01
+6.680e-02
+3.340e-02
-1.021e-14
LEacross-fib
+3.611e-01
+3.152e-01
+2.693e-01
+2.234e-01
+1.774e-01
+1.315e-01
+8.557e-02
+3.964e-02
-6.285e-03
-5.221e-02
-9.814e-02
-1.441e-01
-1.900e-01

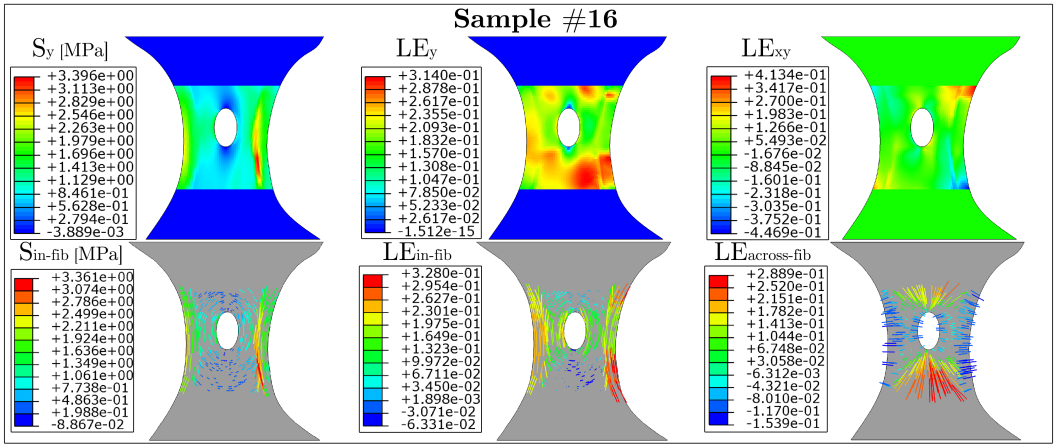

13 Appendix F - Idealised Models - Peak Values Isolated Model Group

Figures 37 and 38 present the peak values of the highest stresses and strains in a single isolated group of models without lumped parameters. The fixed model parameters are as follows. For the idealised morphology models the geometry parameters coincide with the values adapted for the idealised composition models. For the idealised composition models the geometry parameters coincide with the values adapted for the idealised morphology models.

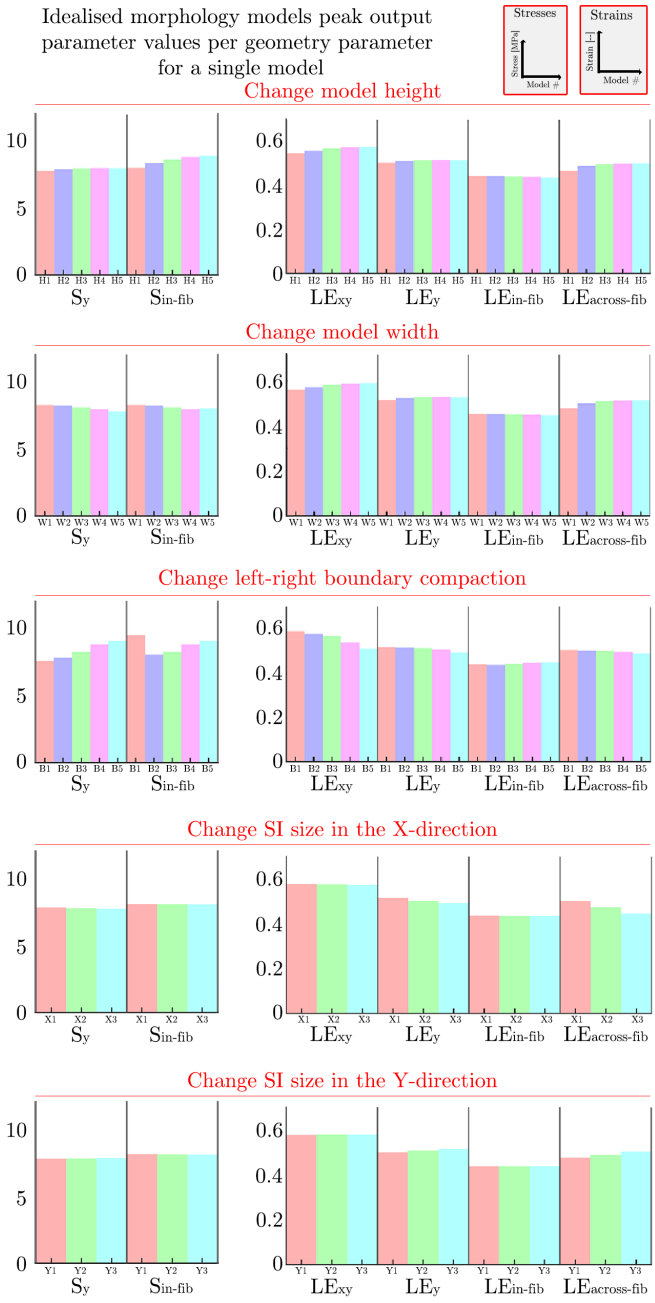

Figure 37: Bar plots of the stresses and strains their peak values for every model subcategory (e.g. changing model height) while fixing all other model parameters. The values on the X-axes of the plots correspond linearly (from lowest to highest values assigned) with the parameter values as presented in Tables 1 and 2.

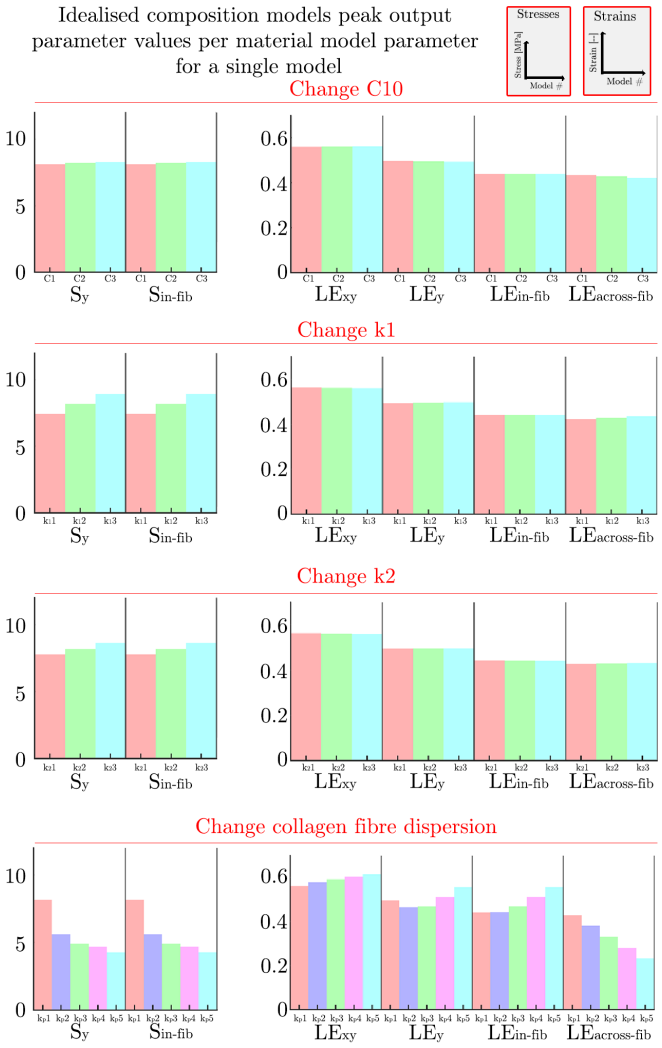

Figure 38: Bar plots of the stresses and strains their peak values for every model subcategory (e.g. changing the to the model assigned C10 value) while fixing all other model parameters. The values on the X-axes of the plots correspond linearly (from lowest to highest values assigned) with the parameter values as presented in Tables 1 and 2.

14 Appendix G - Bio-Engineered Fibrous Cap Model 3 - Distributions

This appendix presents a discussion on the distributions of the stresses and strains in BE-FC model sample number 3. For overview purposes the characteristics of this model as well as its distributions are again presented in figures 39 and 40.

S_y and $S_{\text{in-fib}}$ are similar in both magnitude as well as distribution. More specifically, high stresses are observed in model areas that exhibit both a relatively high degree of anisotropy and wherein the fibres orient predominantly in the loading direction. This is as expected because these model characteristics make the model stiffer in the loading direction. In like manner the model shows comparably lower stresses in areas that are more isotropic and wherein the fibres orient predominantly perpendicular to the loading direction. Further, the stresses near the model its left compacted boundary and the lower half of its right compacted boundary could in part be a result of model contraction, which is highest in model areas with a lot of fibres in the loading direction. Further, the model has three extremely compliant areas; its SI and the two areas outside its compacted boundaries between its corners. During elongation of the model these areas expand effortlessly, decreasing the strain in the loading direction and therefore the stresses in the areas above and under them.

The BE-FC model experiences high LE_{xy} in two different batches of areas. The first hereof comprises the areas near the model its clamps and its corners, diagonally around its SI. These areas are relatively anisotropic and dominated by fibres oriented largely diagonal to the loading direction. In other words, these areas are relatively compliant in shear. Moreover, LE_{xy} is low in the model its bottom right area because it is relatively isotropic there. Further, the three extremely compliant model areas gradually decrease the strain in the loading direction above and under them because they are curved. This strain gradient causes a high LE_{xy} diagonally around the model its SI and in its corners.

LE_y is high in both relatively isotropic as well as anisotropic model areas. Firstly, LE_y should be high there where the model is isotropic, has a geometrical irregularity, and there where the cross-section of the model perpendicular to the loading direction is small. Indeed, LE_y is especially high directly to the left and right of the SI as well as at the model its right compacted boundary. In addition LE_y is high in the areas near the clamps diagonally around the SI. Two observations explain this: these areas are relatively isotropic and they have mostly fibres perpendicular to the loading direction. In other words, these areas are compliant in the loading direction. LE_y is also high near the model its left compacted boundary. This area is relatively anisotropic from clamp to clamp and has largely fibres more in the loading direction; in consequence, the strain is distributed evenly throughout the model its height. Moreover, the LE_y there is increased due to model contraction.

As per deduction $LE_{\text{in-fib}}$ should be high in areas that are compliant whilst having a lot of fibres in the loading direction. Accordingly, such areas should have a high degree of isotropy. This corresponds to the areas directly to the left and right of the SI. Indeed, a high $LE_{\text{in-fib}}$ is observed there. Further, $LE_{\text{in-fib}}$ is also high near the left compacted boundary and the lower part of the right compacted boundary. These areas likewise have fibres predominantly in the direction but are relatively anisotropic. The high $LE_{\text{in-fib}}$ in these areas could be

a result of model contraction. Per contra to this $LE_{\text{across-fib}}$ should be high in areas with mostly fibres perpendicular to the loading direction. Indeed such is observed - $LE_{\text{across-fib}}$ is high above and under the SI. Moreover, it is higher above the SI. This could be a result of the SI being closer to the bottom clamp; the area above the SI is larger and therefore strains more relative to the area under the SI.

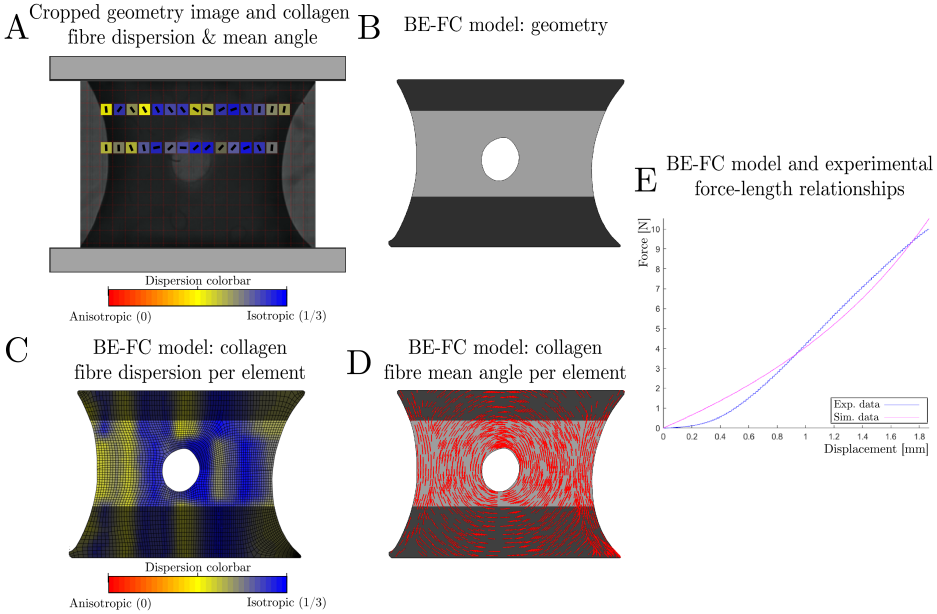

Figure 39: The characteristics of BE-FC model number 3. Subfigure A: the BE-FC its cropped geometry image including the calculated collagen fibre dispersion κ and mean angle Θ for the tiles where collagen is imaged. Tile color = degree of fibre dispersion. Vector within a tile = fibre mean angle. Subfigure B: the model geometry. Dark grey areas: geometry region which is fixed between the tensile tester its clamps. Light grey areas: the non-fixed geometry region. Subfigure C: the model its collagen fibre dispersion κ. Subfigure D: the model its collagen fibre mean angles Θ. Subfigure E: both the model and the experimental force-length relationship ("Sim. data" and "Exp. data", respectively).

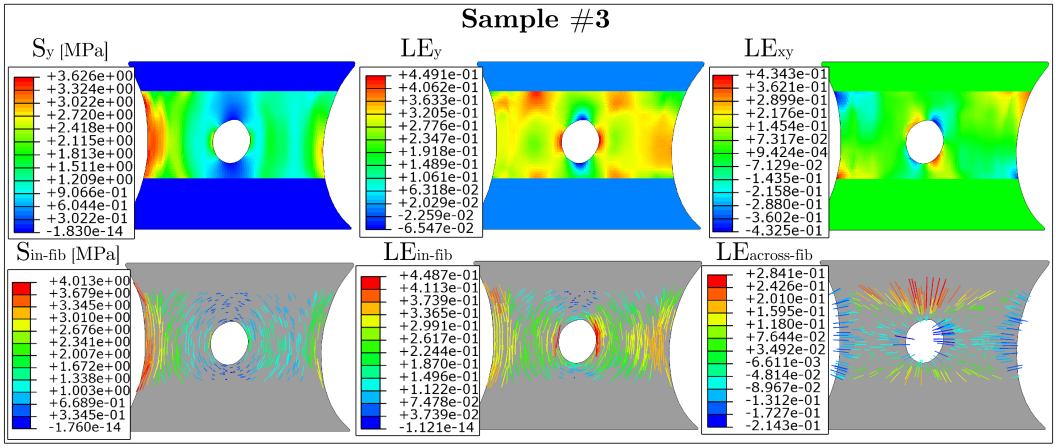

Figure 40: The stress and strain distributions of BE-FC model sample number 3.